Influence of plate tectonic rearrangements on the global ocean circulation

Master's thesis

Faculty of Science

University of Bern

presented by

Patrik Pfister

2013

Supervisor:

Prof. Dr. Thomas Stocker
Physics Institute, Climate and Environmental Physics
and Oeschger Centre for Climate Change Research

Advisor:

Dr. Stefan Ritz
Physics Institute, Climate and Environmental Physics
and Oeschger Centre for Climate Change Research

Abstract

Continental configurations have a large impact on ocean circulation and climate. In this thesis, we use the Bern3D model, a coupled climate model of reduced complexity, to explore this impact by two examples: a modern-world example (Agulhas leakage) and a paleoceanographic example (the opening of Drake Passage).

The leakage of saline waters from the Indian Ocean into the Atlantic, called Agulhas leakage, is parameterized in the coarse-resolution model using freshwater fluxes. In preliminary experiments, it is found that the Atlantic Meridional Overturning Circulation (AMOC) is sensitive to freshwater perturbations in the leakage region. A negative freshwater flux in this region, compensated by an opposite flux in the Indian Ocean, is tested as a simple Agulhas leakage parameterization. In response to this parameterization, an AMOC strengthening is simulated, as well as a very slight modification of the AMOC seasonality.

The opening of Drake Passage is suggested to have caused an increase in the isotopic signature of Neodymium (ϵ_{Nd}) in the Atlantic sector of the Southern Ocean. Such an increase has been measured by Scher and Martin (2006) in marine sediment cores from Ocean Drilling Program (ODP) sites 689 and 1090, and attributed to a Drake Passage opening in the Eocene, at around 41 Ma. Therefore, the ϵ_{Nd} response to a Drake Passage opening in the modern-world bathymetry of the Bern3D model is investigated. Two opening methods are tested, and all simulations are also performed with an open Panama Strait (as in the Eocene). The ϵ_{Nd} response around the ODP sites is in qualitative agreement with the sediment core data in the case of an open Panama Strait, for the more robust opening method. However, the fact that the other opening method does not produce such a clear signal shows that the ϵ_{Nd} response is highly sensitive to the bathymetric shape of the Drake Passage during the opening.

Therefore, we propose that the Neodymium experiments are repeated with a finer model resolution at high latitudes. Ideally, they should be repeated in an Eocene setting. For this purpose, an Eocene bathymetry for the Bern3D model with doubled horizontal resolution is also introduced in this thesis. Effects of the resolution and bathymetry modifications are described, and preliminary Drake Passage opening experiments are performed in this Eocene bathymetry. From these experiments, we infer that more robust opening methods have to be tested also in this bathymetry; and that modifications of the Tasmanian Gateway should be included in future Neodymium experiments, because they have a significant impact on Eocene throughflows.

Contents

1. Introduction **1**

1.1. Agulhas Leakage . . . 2
1.2. Tectonic rearrangements . . . 3
1.2.1. Neodymium isotopes . . . 4
1.3. Goals and Structure of this thesis . . . 4

2. Methods **7**

2.1. Model description summary . . . 7
2.1.1. Resolution and bathymetry . . . 7
2.2. Ocean circulation . . . 8
2.2.1. Boundary drag . . . 9
2.3. Model spinup for modern and Eocene simulations . . . 11
2.4. Agulhas leakage experiments . . . 12
2.5. Tectonic rearrangements . . . 14
2.5.1. Overview . . . 14
2.5.2. Input map modifications . . . 14
2.6. Modern-world tectonic rearrangements . . . 15
2.6.1. Pseudo-transient simulations . . . 15
2.6.2. Detailed description of bathymetry modifications . . . 16
2.7. From standard to double resolution . . . 20
2.8. Eocene bathymetry . . . 21
2.8.1. Creating the input maps from the original bathymetry . . . 22
2.8.2. Eocene bathymetries . . . 22
2.9. Eocene simulations . . . 23
2.9.1. Model adaptations . . . 23
2.9.2. Eocene tectonic rearrangements . . . 25
2.10. Neodymium experiments . . . 26

3. Results and Discussion **29**

3.1. Agulhas leakage experiments . . . 29
3.1.1. Leakage location: dye tracer experiments . . . 29
3.1.2. Single freshwater pulses at cape Agulhas . . . 30
3.1.3. Periodic freshwater forcings and impact on AMOC seasonality . . . 33
3.1.4. Dipole compenstation: an Agulhas leakage parameterization . . . 37
3.1.5. AMOC Hysteresis . . . 41
3.2. Modern world tectonic rearrangements . . . 43
3.2.1. Topographies with closed Drake Passage and open Panama Strait . . . 43
3.2.2. Effects of opening Drake Passage and Panama Strait . . . 51

3.2.3. Influence of Drake Passage on Neodymium isotopes: model-data comparison 58
3.3. From standard to double resolution: modern and Eocene maps 60
3.4. Eocene ocean circulation: comparison with a comprehensive GCM 68
3.5. Tectonic rearrangements in the Eocene bathymetry 71

4. Summary and Outlook **77**

A. The seven input maps **80**

B. Description of the regridding process **81**

List of Abbreviations

not listed here	Model run names: Consult Section 2.5.1, or Table 1 or 2.
$[\mathrm{Nd}]_d$	Total concentration of dissolved Neodymium, $[^{143}\mathrm{Nd}]_d + [^{144}\mathrm{Nd}]_d$
ϵ_{Nd}	Normalized deviation of the isotopic ratio $^{143}\mathrm{Nd}/^{144}\mathrm{Nd}$ from a standard value
AABW	Antarctic Bottom Water
ACC	Antarctic Circumpolar Current
AIW	Antarctic Intermediate Water
AMOC	Atlantic meridional overturning circulation
AOGCM	Atmosphere-Ocean General Circulation Model
APF	Atlantic-to-Pacific freshwater flux
BGC	Biogeochemistry
CESM1.1	Community Earth System Model, version 1.1
EBM	Energy Balance Model
GCM	General Circulation Model
GMOC	Global meridional overturning circulation
HadCM3	Hadley Centre Coupled Model, version 3
L1-L5	Agulhas leakage locations, see Figure 12.
Ma	Million years before present
MOC	Meridional Overturning Circulation
MPI-OM	Max Planck Institute - Ocean Model
NADW	North Atlantic Deep Water
Nd	Neodymium
ODP	Ocean Drilling Program
pCO_2	Atmospheric CO_2 partial pressure
PE	Eocene simulation of the MPI-OM with $pCO_2 = 560\,\mathrm{ppm}$
PE1	Eocene simulation of the MPI-OM with $pCO_2 = 280\,\mathrm{ppm}$
SOMOC	Southern Ocean meridional overturning circulation
SSS	Sea Surface Salinity
SST	Sea Surface Temperature
Sv	Sverdrup, $1\,\mathrm{Sv} = 10^6\,\mathrm{m}^3\,\mathrm{s}^{-1}$
WBC	Western Boundary Current

1. Introduction

Continental configurations have a large impact on climate as physical boundaries for one of its major drivers, the global termohaline ocean circulation. In a world without continents and a flat bathymetry (aquaplanet), wind-driven zonal currents would encircle the whole globe (Smith et al., 2006). In the modern world, however, continental boundaries constrain ocean gyres, western boundary currents (WBC), regions of deep water formation, and more large-scale circulation features governing our climate. A very special, smaller-scale feature is the Agulhas Leakage. This phenomenon is only possible because of the particular position of Africa's southernmost tip, which extends "only" to a latitude of about 35° South, where wind stress forcing is minimal (Beal et al., 2011). Therefore, the WBC along Africa's east coast is not fully deflected back into the Indian Ocean gyre—as it would be if Africa extended further South into the region of strong westerlies—but part of it feeds into the South Atlantic gyre via Agulhas Leakage. One could say "Africa is too short". This phenomenon is further described in Section 1.1.

In the tectonic evolution of the Earth, continental configurations much different from the modern world emerged. About 320 Ma (million years ago), all land masses were connected into a single continent, the supercontinent Pangaea (Veevers et al., 1994). Since Pangaea was split into multiple continents starting from about 230 Ma (Schettino and Turco, 2009), the continents have been drifting towards their modern positions. In the Eocene (56 Ma to ~34 Ma), there were still large bathymetric differences to the modern world, as shown in Section 2.8.2. Also, important tectonic rearrangements occured in this period, such as the separation of Australia and South America from Antarctica. These are further described in Section 1.2, and the latter separation is the main focus of this Master's thesis.

Paleoclimate simulations provide settings that are vastly different from the modern world. Therefore, they are ideal for a Master's thesis, because they also serve as a good introduction to the climate model being used. Modifying the model's very foundations or crucial parameters helps to get a better understanding of its mechanisms and limitations. An earlier Master's thesis by Kosch (2011) showed that the Bern3D model is capable of simulating a "Snowball Earth", where the oceans are entirely covered with sea ice. Now, this Master's thesis focuses on plate tectonic rearrangements, and aims to demonstrate that it is also capable of simulating heavily modified continental configurations. In addition to the modifications in the modern world which are needed for Neodymium experiments (compare Section 1.2.1), an Eocene bathymetry is introduced.

The Eocene is not only relevant for research on plate tectonic rearrangements, but also for future climate change research. Due to antrophogenic CO_2 emissions, the atmospheric CO_2 partial pressure (pCO_2) could rise to up to 2000 ppm until year 2300 under an extreme scenario (Meinshausen et al., 2011). To find comparable atmospheric CO_2 concentrations in Earth's history, one has to go as far back as the Eocene (Pearson and Palmer, 2000). The high

pCO_2 in this period was one of the main reasons that the period following the Paleocene-Eocene transition was the warmest period in the last 65 million years (Zachos et al., 2001), the so-called Paleocene-Eocene Thermal Maximum (PETM) (Sluijs et al., 2011).

1.1. Agulhas Leakage

Warm and saline waters are transported from the Indian Ocean into the Atlantic around Cape Agulhas at the southern tip of Africa. This flow, termed Agulhas leakage, consists predominantly of mesoscale cyclonic or anticyclonic eddies (Agulhas rings). In their review paper, Beal et al., 2011 summarize that 4 -6 Agulhas rings evolve annually, and that Agulhas leakage is estimated to amount to 2 to 15 Sverdrup (Sv, $1\,\mathrm{Sv} = 10^6\,\mathrm{m}^3\,\mathrm{s}^{-1}$). Recent findings highlight the importance of Agulhas leakage for both paleoclimate research and climate change projections, due to its impact on the Atlantic Meridional Overturning Circulation (AMOC). From planktic foraminifera records of the last 550,000 years, Peeters et al., 2004 reconstructed peaks in Agulhas leakage strength shortly before glacial terminations, indicating that the leakage may have played a crucial role in the triggering of these events. While an increase in leakage strength under anthropogenic warming has not been directly measured, it was simulated in a high-resolution General Circulation Model (GCM) that was forced with the poleward shift of Southern Hemisphere westerlies recorded during the last 20 -30 years (Biastoch et al., 2009). An increase in Agulhas leakage strengthens the AMOC, possibly counteracting the projected slowing of the overturning due to Arctic meltwater in a warming climate (Gregory et al., 2005). Two main mechanisms have been found to cause an AMOC strengthening in response to increased leakage: dynamical perturbation by Agulhas Rings (Sebille et al., 2012; Sebille and Leeuwen, 2007) and buoyancy forcing (Weijer et al., 2002), which is briefly described in the following. The heat anomaly of Agulhas leakage water masses is lost to the atmosphere as they propagate through the South Atlantic, but the salt anomaly is transported further into the North Atlantic, where it increases the density at the ocean surface. This enhances deep convection and North Atlantic Deep Water (NADW) formation, in turn strengthening the AMOC.

Beal et al., 2011 suggest that a horizontal resolution of 0.1° is needed to properly simulate Agulhas leakage. However, in contrast to other unresolved phenomena (e.g., enhanced deep water formation in the Ross and Weddell Seas; compare Ritz et al., 2011), Agulhas leakage is not yet parameterized in the Bern3D model. In this work, the simplest possible leakage parameterization will be tested: a salt influx into a single ocean grid box near Cape Agulhas, compensated by a freshwater influx into the Indian Ocean where the leakage originates ("dipole compensation"). Preliminary experiments will be conducted using dye tracers, which are a useful tool to investigate ocean circulation features as they are purely passive tracers for the water mass distribution. This means that the ocean circulation governs the distribution of dye tracers, but not vice versa: The circulation does not act to compensate a gradient in dye tracer concentration, nor is it altered by the tracers in any other way.

The flow direction of the dye tracers will show whether Agulhas leakage can be simulated in the Bern3D model (with this parameterization), and which grid box locations are the most suitable. Furthermore, the response of the AMOC to strong freshwater pulses in the Agulhas leakage region will be studied, leading to hysteresis experiments. Finally, the impact of the temporal shape of the freshwater or salt perturbations will be investigated, including periodic forcings to emulate the occurance of Agulhas rings.

1.2. Tectonic rearrangements

Tectonic rearrangements, i.e. the movement of continental plates during the past millions of years, have had a major impact on climate. Two important such events took place in the Paleogene period, 66 to 23 million years before present (Ma), which is subdivided into the Paleocene (66 Ma to 56 Ma), Eocene (56 Ma to ~34 Ma)and Oligocene epochs (~34 Ma to ~23 Ma) (Cohen et al., 2012). These are the openings of Drake Passage separating South America from Antarctica, and the Tasmanian Gateway separating Australia from Antarctica. They enabled the Antarctic Circumpolar Current (ACC) that presently transports 140 Sv of water through Drake Passage (Ganachaud and Wunsch, 2000). Out of the two, the Drake Passage opening probably had a higher impact on global ocean circulation: Firstly, because South America provides a much larger barrier than Australia (latitudinally), and secondly, because the Drake throughflow is directly linked to the Atlantic Meridional Overturning Circulation (AMOC)(Toggweiler and Samuels, 1995). The AMOC in turn is a major driver of the global termohaline circulation and thus has a great impact on climate.

The timing of the openings of Drake Passage and Tasmanian Gateway is a matter of debate. However, it is important to assess the role of these gateways and the ACC in Cenozonic cooling (the Cenozonic era lasts from the Paleogene to the present), especially in Antarctic glaciation that was triggered during at the Eocene-Oligocene transition (Zachos et al., 2001). Based on magnetic anomalies, Lawver and Gahagan (1998) state that Drake Passage probably opened by 32.5 Ma and was clearly closed at 40 Ma, along with the Tasmanian Gateway that opened almost simultaneously according to their findings. Zachos et al. (2001) present a slightly earlier Tasmanian Gateway opening and a slightly later Drake Passage opening, with a gap of 3 to 5 million years between the two events. Other studies date the Drake Passage opening to between 49 and 17 Ma (Scher and Martin, 2006). From Neodymium (Nd) isotopes (compare Section 1.2.1), Scher and Martin (2006) infer that Drake Passage opened at around 41 Ma, and that the order was reversed (Tasmanian Gateway opening after Drake Passage). One of the main research questions of this Master's thesis is, if the Nd response they associate with the Drake Passage opening can be reproduced in our model. Further details are given in the following section.

1.2.1. Neodymium isotopes

Various elements and isotopic ratios can be used as water mass tracers, i.e. to provide information about ocean circulation. However, many of these are not only influenced by water circulation but also by biological processes and other sources and sinks (e.g., δ^{13}C, δ^{18}O). An advantage of the quasi-conservative water mass tracer ϵ_{Nd} (the normalized deviation of the isotopic ratio ^{143}Nd/^{144}Nd from a standard value) is that it is virtually unaffected by biological processes. Also, ϵ_{Nd} is positively correlated with salinity, which makes it even better suited as a water mass tracer. The sources and sinks of the Nd isotopes are subject of current research. They were also investigated when Nd was incorporated in the Bern3D model by Rempfer et al. (2011). ^{143}Nd and ^{144}Nd are transported independently in the model. Dust fluxes, river discharge and Nd flux from continental margins to the ocean (boundary source) were identified as Nd sources, the only sink being the deposition on the seafloor due to sinking particles.

Pacific water masses have a more radiogenic (i.e., less negative) ϵ_{Nd} signature than Atlantic water masses, because the boundary source is more radiogenic; compare, e.g., Figure 1c in Rempfer et al. (2011). When the Drake Passage is opened, Pacific water is transported into the Atlantic by Drake throughflow. Therefore, it is expected that the opening causes an drift towards less negative ϵ_{Nd} values in the Atlantic sector of the Southern Ocean (hereafter simply called Atlantic Southern Ocean), i.e., east of Drake Passage. A secondary effect could further enhance this drift: increasing Drake throughflow increases the AMOC strength (Toggweiler and Samuels, 1995), which in turn increases ϵ_{Nd} values in the Atlantic Southern Ocean (Rempfer et al., 2012). An ϵ_{Nd} increase was actually found by Scher and Martin (2006) in fossil fish teeth from marine sediment cores in this region, which carry a benthic (seafloor) isotope signature. The analyzed cores come from the Ocean Drilling Program (ODP) sites 689 (Maud Rise) and 1090 (Agulhas Ridge), as shown in Figure 10. Scher and Martin (2006) conclude that the onset of the measured ϵ_{Nd} increase corresponds to the opening of Drake Passage.

1.3. Goals and Structure of this thesis

In this thesis, the following research questions will be addressed:

- Can Agulhas Leakage be parameterized in the Bern3D model by a freshwater forcing in the leakage region? If yes, does this simple parameterization for Agulhas Leakage enhance the AMOC? Can it (partly) replace the Atlantic-to-Pacific freshwater flux that is prescribed in the model? Is there also an influence on the seasonality of the AMOC, and does it depend on the seasonality of the forcing? What is the AMOC response on extremely strong forcings in the leakage region, and can a hysteresis behavior be produced?

- How do the ocean circulation and climate change in a modern-world setting if a) the Drake Passage is closed, b) the Panama Strait is opened and c) both tectonic modifi-

cations are applied simultaneously? What is the response of the Nd isotopes to these modifications? What changes if the Strait of Suez is opened additionally, in analogy to an open Tethys Seaway in the Eocene?

- Starting from the cases a) and c) as described above, what are the effects of a stepwise Drake Passage opening on the Drake throughflow, Panama throughflow (case c) only) and AMOC strength (case a) only)? Is an increase in ϵ_{Nd} values measured around ODP sites 689 and 1090 in response to the Drake Passage openings? If yes, how does it compare to the data from marine sediment cores shown in Scher and Martin (2006)? Two different opening methods and two different bathymetric evolutions of Drake Passage will be tested to tackle these questions.

A more realistic setting for this comparison would be a Drake Passage opening under Eocene conditions. It is beyond the scope of this thesis to adapt the model to realistically simulate Eocene climate, including adaptation of the Nd isotopes; but the most important adaptations will be made to enable simulations with an Eocene bathymetry. This will involve a doubling of the model resolution. These simulations should address the following questions:

- What is the effect of a doubling of the model resolution, if the bathymetry is not modified? What are the changes due to the Eocene bathymetry, and due to the model adaptations made? How does the circulation in the Eocene bathymetry compare to the Eocene circulation in a GCM?

- In analogy to the experiments in the modern-world setting, what are the effects of a stepwise Drake Passage opening in the Eocene bathymetry on the Drake throughflow, Panama throughflow and Tethys Seaway throughflow? How do these change if the Tasmanian Gateway is made shallower or deeper, or even closed? Would these experiments be a sound basis for Nd experiments in an Eocene setting, if Nd was adapted to the different bathymetry?

This thesis is structured as follows. Section 2 describes parts of the Bern3D model that are most important for this thesis. It further describes the experiments that were conducted, and the model adaptations that were made. In Section 3, the results are presented and discussed. In Section 4, the findings and main interpretations are summarized, and the research questions listed above are addressed. Furthermore, an outlook is presented on possible future research.

2. Methods

2.1. Model description summary

The Bern3D model is a coupled ocean-atmosphere model of reduced complexity. In contrast to the most complex climate models available, the comprehensive coupled atmosphere-ocean general circulation models (AOGCMs), the resolution of Bern3D is very coarse, especially in the horizontal direction (see below). Also, many physical processes are parameterized because they cannot not be properly resolved by the model. However, the advantage of such reduced-complexity models is their efficiency. The integration time of AOGCMs is limited to several hundred years, even if the simulations are run on large computer clusters. Ensemble simulations on glacial-interglacial time scales can only be performed using a model of reduced complexity (Menviel et al., 2012; Roth and Joos, 2013). The Bern3D model, which can be run on a single personal computer, is able to perform coupled 800'000-year simulations (Ritz et al., 2011). In its current state, the model is not parallelized, i.e., it can not take advantage of multiple processing units (cores) to speed up the computation. Run on a 2.8 GHz core, a 5000-year simulation with standard resolution takes roughly one hour without the BGC module, and around 4.5 hours including BGC.

The three-dimensional ocean component of the Bern3D model is a seasonally forced frictional geostrophic balance model (Mueller et al., 2006; Ritz, 2012). It can be run under restoring or mixed boundary conditions, or coupled to a two-dimensional atmospheric component which is a single-layer energy and moisture balance model (EBM) (Ritz et al., 2011). All experiments for this thesis were made with the coupled model. The ocean model also has a biogeochemical (BGC) component which is described in Parekh et al. (2008) and Tschumi et al. (2008). It has recently been extended by the addition of Neodymium (Nd) isotopes (compare Section 1.2.1 and 2.10) as a novel water mass tracer (Rempfer et al., 2011). In this thesis, the BGC component was only used for experiments with Nd. The Bern3D model can also be coupled to a land vegetation model (LPX) (Roth and Joos, 2013), but this option was not used here.

2.1.1. Resolution and bathymetry

The Bern3D model has a standard resolution of 36x36 grid cells in the horizontal, and 32 ocean depth layers. The horizontal boxes are equally spaced in longitude and in the sine of latitude. As a result, the horizontal area of all grid boxes is equal, and the resolution is much coarser near the poles than near the equator: the grid box closest to the pole spans almost 20° meridonally. Because the Eocene map requires a higher resolution in the high latitudes, the horizontal resolution is doubled to 72×72 boxes for experiments with this map (compare section 2.7). The standard vertical resolution of 32 layers was not modified. The maximum ocean depth of 5000 m is divided into 32 logarithmically spaced layers, the uppermost layer being 39 m thick and the lowermost 397 m thick (Mueller et al., 2006). As documented in Ritz (2012), the edges (top/bottom) of the vertical layers are given by the formula

$$z_k^w = \eta \left[\left(1 + \frac{1}{\eta}\right)^{\frac{kmax-k+1}{kmax}} - 1 \right] \cdot 5000\,\mathrm{m}; \qquad k \in \{1, ..., kmax + 1\}, \tag{1}$$

where $kmax = 32$ is the number of layers and $\eta = 0.1$ a scaling factor for the exponential cell-height increase. The centers of the cells, which are needed in the interpolation process (section 2.8.1), can be calculated as

$$z_k^c = \eta \left[\left(1 + \frac{1}{\eta}\right)^{\frac{kmax-k+0.5}{kmax}} - 1 \right] \cdot 5000\,\mathrm{m}; \qquad k \in \{1, ..., kmax\}. \tag{2}$$

Figure 1 shows the standard modern-world bathymetry. It includes an open Bering Strait and open Strait of Gibraltar. Details concerning the Drake Passage, Panama and Suez regions are given in section 2.6.2.

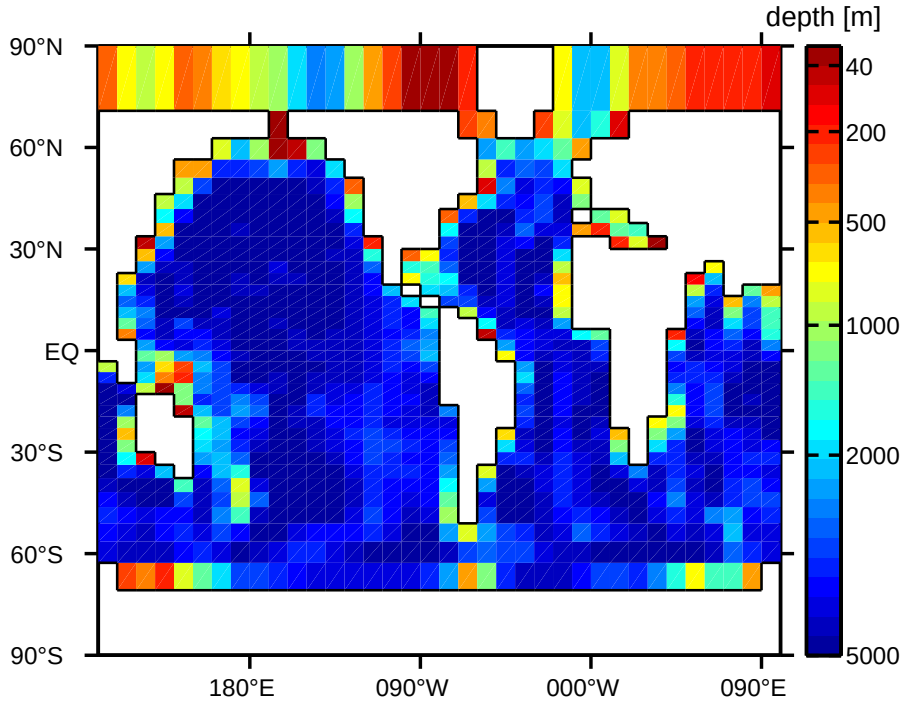

Figure 1: Standard Bern3D modern-world bathymetry. Colors show the seafloor elevation k in layers of exponentially decreasing height, and correspond to the depths calculated in equation 1. Some depths in meters are indicated next to the color bar.

2.2. Ocean circulation

The ocean model has been tuned to realistically represent vertical exchange of tracers and heat. As described in Mueller et al. (2006), physical variables of the model simulations are in good agreement with observations (ocean temperature T, salinity S, meridional heat transport, various tracer concentrations including anthropogenic carbon). However, the model also shows some weaknesses which are of special interest for this thesis. The formation and

propagation of Antarctic Intermediate Water (AIW), as well as the ACC, are too weak in the Bern3D simulations. To compensate for this, the Drake Passage has been widened and deepened (Mueller et al., 2006). Nonetheless, the ACC is still much weaker than in a typical AOGCM, such as the Community Earth System Model (CESM1.1) for example (UCAR, 2013a). The flow through Drake Passage amounts to 38 Sv in the standard setting of the Bern3D model, whereas it is around 160 Sv in the CESM1.1 control run (UCAR, 2013b). The major ocean gyres are also too slow by roughly a factor of two in the Bern3D model. Also, formation of Antarctic Bottom Water (AABW) is too weak, probably because atmospheric temperatures over the Southern Ocean and Antarctica are too warm (Ritz et al., 2011). The maximum AMOC strength is 14.5 Sv in the standard setting. In some simulations for this thesis, a modification was made which increased the modern AMOC strength by 2 Sv. This is described in Section 2.5.2.

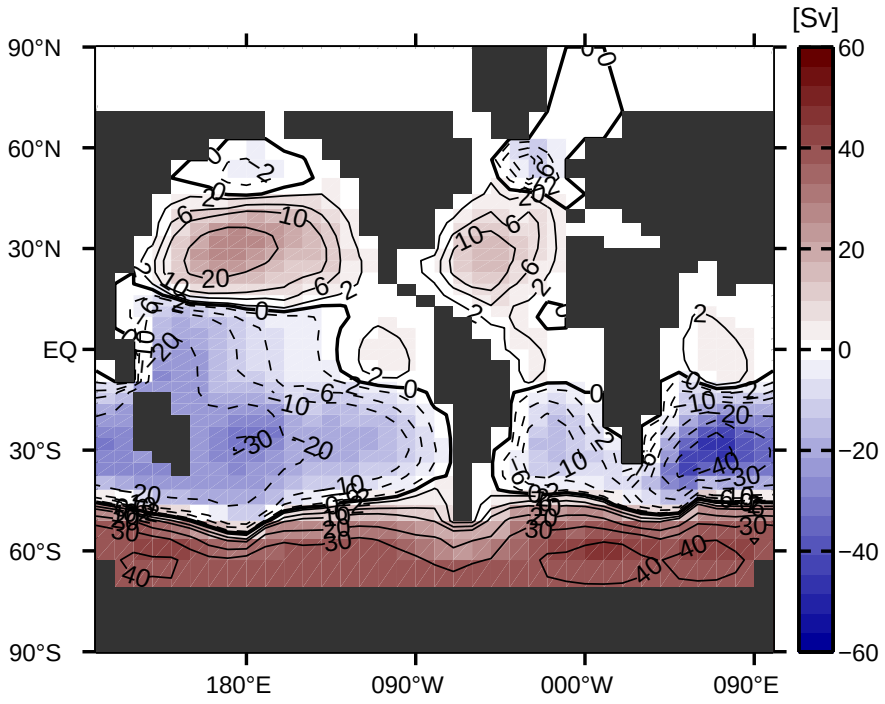

Figure 2: Depth-integrated ocean circulation in a standard Bern3D modern control simulation (CTRL). Contours show the barotropic stream function in Sverdrup (Sv).

However, results of tracer experiments (e.g., Nd distributions) should still be comparable to observations, because the model's tracer distribution was tuned to match observations in the standard model setting, which produced this too weak ocean circulation.

2.2.1. Boundary drag

Various parameters influence the simulated ocean circulation, including ocean diffusivities, scaling of the wind stress input fields, Atlantic-to-Pacific freshwater flux (APF, compare Section 2.4), and more. These parameters were not modified in the experiments with different bathymetries. However, another very important factor is the boundary drag, which is au-

tomatically modified when the ocean boundaries are moved or altered. Three parameters influence the boundary drag: the minimum drag a in the ocean interior, the boundary drag scaling factor λ, and the minimum seafloor elevation level k_λ which classifies an ocean cell as "shallow". a is applied to all grid cells, enabling a stable ocean circulation in the model. λ is only applied to a gridcell if a nearby gridcell is either land or shallow water (i.e. $k > k_\lambda$). The drag multipliers are calculated on the psi-grid, i.e., the edges of the grid that we normally look at (which is the center- or T-grid). The drag in all psi-grid cells that have land or shallow water in one of their nearest neighbouring cells is multiplied by λ^2, the drag in those which have land or shallow water in one of the second nearest neighbours by λ. In order to apply this drag multiplier to the water mass flow, it has to be interpolated onto the u-grid and v-grid, as illustrated and explained in more detail in Figure 3. For more details on the different grids, compare Ritz (2012).

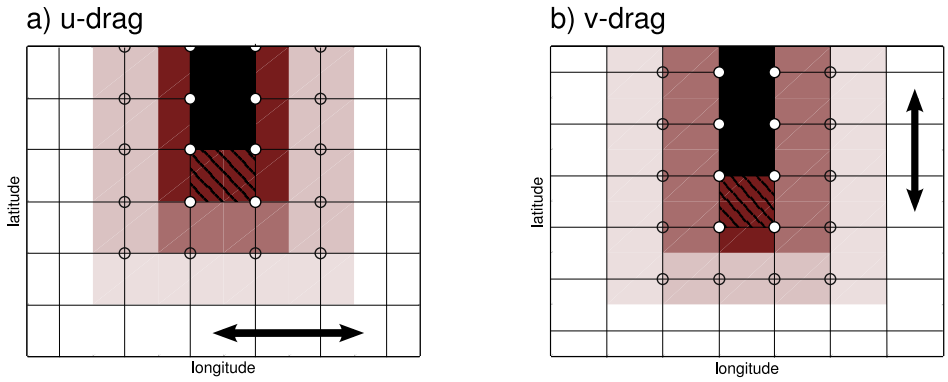

Figure 3: Schematic example for boundary drag multipliers around land cells (black) and shallow water cells (black hatched). The grid shown is the center- or T-grid, its edges are the psi-grid. The standard drag on the psi-grid is multiplied by 1 (no circle) or λ (empty circle) or λ^2 (white filled circle) depending on the distance from the next shallow/land cell. In the standard model setting, $\lambda = 2$. The intensity of the red shaded areas indicates the drag multiplier as interpolated onto the u-grid (a) and v-grid (b). The direction of the flow to which this drag multiplier is applied, is shown by the black arrow in both panels. A realistic flow has velocity components in both directions, therefore u-drag and v-drag are applied simultaneously.

In the Bern3D model, $\lambda = 2$ and $k_\lambda = k_{max}/2 = 16$ are the standard values; the value determining a is given as a unitless inverse quantity, therefore it is not informative to specify here. For the simulations shown in this thesis, the standard values were used, but preliminary tests were made with different values. While combinations of a, λ and k_λ which result in a lower boundary drag can strengthen the circulation by up to 25 % on average, unwanted boundary artifacts may appear (e.g., east of Greenland). Also, the drag threshold below which the model becomes numerically unstable is soon reached when the drag parameters are lowered, resulting in an unstable circulation and eventually causing the model to crash. Gerber and Joos (2013) have tuned a (among other parameters) to best reproduce observed distributions of temperature and salinity in combination with zero to two additional tracers. In all cases, they have found a lower value for a (down to $a_{tuned} = \frac{2}{3}a$). Note that they have used a different notation: their λ is not the λ described above, but $\lambda = C/a$, where C is a constant accounting for the drag units.

When modifying the bathymetry, it is important to note that changing the seafloor elevation from 16 to 17 layers in an ocean cell increases the boundary drag significantly in up to 25 surrounding cells (because $k_\lambda = 16$). To avoid this additional effect, it is legitimate to modify the k1 mask in such critical locations – these small bathymetry modifications will normally have a smaller effect on the circulation than the artificially introduced additional drag. On the other hand, it may sometimes be an interesting option to deepen some shallow ocean cells to 15 layers (just below k_λ) to stimulate the flow (e.g., through a shallow gateway). This was done for some bathymetries in this thesis, as described in Section 2.9.2.

2.3. Model spinup for modern and Eocene simulations

Before new experiments can be made, the model has to run through a "spinup" procedure in order to achieve steady state conditions. It consists of the following steps:

Spinup 1 The ocean model is run under restoring boundary conditions. Temperature and salinity are restored at the ocean surface (compare Section 2.4) to SST and SSS fields taken from Levitus and Boyer (1994) and Levitus et al. (1994). Consequently, a steady state is reached with SST and SSS very similar to these restoring fields, corresponding to modern-world conditions. However, the same restoring fields were also used for spinup 1 of Eocene maps (missing values were interpolated to get restoring values for all Eocene ocean boxes). The spinup 1 output of the Eocene simulations should hence not be interpreted because it is heavily biased by the modern-world input fields, but it still serves as a stable starting point from which the coupled model can be run. A duration of 10,000 simulation years is recommended for spinup 1, but normally 5000 years are enough to obtain a steady state.

Spinup 2 Still under restoring boundary conditions, this step serves only to diagnose a spatial climatology of the Dalton constant, a property influencing evaporation in the coupled model, see Ritz et al. (2011) for details. 50 model years are sufficient for this diagnosis.

Spinup 3 The ocean model is coupled to the energy balance model, which is run with a constant orbital forcing. Also, the water vapor feedback is not yet included because an EBM steady state is needed to calculate that. However, if one is only interested in a steady state of the coupled model, the output of spinup 3 is normally sufficient. Therefore, all Eocene steady state simulations were run up to this point and then analyzed. Spinup 3 takes 5000 simulation years.

Spinup 3b From the steady state output of spinup 3, an EBM control temperature is diagnosed during 1000 simulation years. After spinup 3b, the water vapor feedback can be included in the simulation. This feedback has been tuned such that the climate sensitivity (global average temperature rise due to a doubling of atmospheric CO_2 concentration) for a modern-world control run is 3 K (Ritz et al., 2011). Without it, the climate sensitivity is 3.5 °C, which is higher than the current best estimations. Therefore, the water vapor feedback

is needed if the steady state is perturbed. It was included in all simulations made for Section 3.1, and in all simulations including Nd.

Spinup 4 This step is only required if the BGC component of the model is used, i.e. in this thesis only as a prerequisite for Nd simulations. In this case, spinup 3b can be skipped as the EBM control temperature can also diagnosed during spinup 4. But mainly, all BGC tracers are initialized in this spinup and distributed until a steady state is reached, which normally takes 5000 model years.

Spinup 5 In this step, the Nd isotopes are introduced. It may take up to 20,000 years until the Nd distributions reach equilibrium. The water vapor feedback for the EBM could already be enabled at the start of this spinup, but in the simulations for this thesis, it was only included afterwards in an additional model run.

The option for time-dependent insolation in the EBM is only needed if the exact period which the run should reproduce is known, i.e. in transient simulations with specified start and end dates. For all experiments made for this thesis, the insolation was kept constant at modern values.

2.4. Agulhas leakage experiments

Restoring fluxes

In ocean models, restoring fluxes are commonly used to control the sea surface concentration of a physical quantity (e.g., temperature, salinity, etc.). Restoring means that the flux out of each ocean cell (i, j) ($i \hat{=}$ longitude, $j \hat{=}$ latitude) is proportional to the difference of the concentration $C(i, j)$ and its control value $C_{restoring}(i, j)$:

$$F_{restoring}(i, j) = -\frac{1}{\tau}(C_{restoring}(i, j) - C(i, j)), \tag{3}$$

where τ is the restoring time scale. The smaller τ, the faster deviations from the control value are compensated by the restoring flux. A typical value used in the Bern3D model for temperature, salinity and also dye tracer restoring is $\tau = 20\,\text{days}$. The sign convention in equation 3 is such that $F_{restoring} > 0$ corresponds to a flux out of the ocean.

Dye tracers

In the Bern3D model, an atmosphere-to-ocean flux of a dye tracer can be prescribed in one or more horizontal grid boxes to simulate a dye tracer injection into the ocean. This is done by restoring the dye tracer concentration to 100 % at the ocean surface (i.e., in the top most grid box) at the chosen tracer inlet locations. From there, the tracer is transported as described, e.g., in Ritz (2012), without any further sources or sinks in the tracer transport equation.
Normally, dye tracer concentrations are restored to zero in all ocean surface cells except the inlet locations, because one is mainly interested in the depth propagation of the water

masses. In the Agulhas leakage experiments however, the dye tracers were mainly used to track horizontal circulation directions. Therefore, these restoring fluxes were removed to allow the dye tracers to propagate freely also along the surface. The various dye tracer experiments made for Agulhas leakage simulations are described in detail in Section 3.1.1.

Freshwater fluxes

A salt or freshwater inflow can be simulated by prescribing an atmosphere-to-ocean flux of freshwater in specific sea surface cells (a negative freshwater flux corresponds to a salt influx). In contrast to the dye tracer restoring fluxes, the amount of freshwater introduced per timestep is fixed - the fluxes are kept constant, independent of sea surface salinity. This means that freshwater perturbations will behave differently from dye tracers, because they are not restoring fluxes. For example, if a dye tracer is injected into a box where the ocean circulation is slow, it is only removed slowly from this location (and mainly by diffusion), because the advection is proportional to the speed of the water masses. Therefore, the dye tracer concentration always stays close to its restoring value in this box, such that only a small amount of dye is injected during each time step. Consequently, the increase in the global inventory of this dye tracer is also smaller than if the tracer was injected into a more rapidly ventilated location. On the other hand, if freshwater is injected into a box with slow circulation, the salinity will rapidly decrease in this region because the flux is fixed. The global salinity will decrease linearly with time, independently of ocean circulation.

This means that, unless the freshwater flux is compensated elsewhere, the salt budget of the whole ocean is not constant during the perturbation, and sea level changes would occur if this possibility was included in the model. Therefore, the impact of such a flux (e.g., on ocean circulation) may only partly be caused by the investigated perturbation itself, and partly by these additional effects. Two compensation methods were tested in the Agulhas leakage simulations: compensation in all unperturbed surface boxes (always compared to the uncompensated simulations in Section 3.1.2) and dipole compensation (Section 3.1.4).
Different kinds of freshwater experiments were made for Agulhas leakage simulations. They are described separately in Sections 3.1.2 to 3.1.5.

Atlantic-to-Pacific freshwater flux

An Atlantic-to-Pacific freshwater flux (APF) is often prescribed in ocean models to compensate for the missing effect of a dynamical atmosphere (Zaucker et al., 1994). It is also used in coupled models of reduced complexity, in particular those with a simplified atmosphere. The APF in the Bern3D model is a tunable quantity and chosen as 0.34 Sv in two parts: 0.17 Sv of freshwater is transferred from the South Atlantic into the South Pacific, and the same amount from the North Atlantic into the North Pacific (Ritz et al., 2011). This increases the SSS of the Atlantic Basin, creating surface water that is dense enough to enable an AMOC in the coupled model. A weaker APF causes a weaker AMOC, and if the APF is removed entirely the AMOC collapses. Section 3.1.4 addresses the question if part of the Bern3D APF can be substitued by an Agulhas leakage parameterization.

2.5. Tectonic rearrangements

2.5.1. Overview

The seven maps (or masks) that determine the topographic boundary conditions of the Bern3D model are named `*.k1`, `*.lmask`, `*.bmask`, `*.dyemask`, `*.alti`, `*.psiles` and `*.paths`, where `*` is a name consisting of eleven characters. The information stored in each map is briefly described in Appendix A. The standard Bern3D modern-world map is named `wor36_misls` (for "multiple islands"), which will hereafter be abbreviated by MOD36. For this master thesis, four new world maps were generated. They are listed here with abbreviated names:

MOD2X A duplicate of the MOD36 bathymetry, but with doubled horizontal resolution (72×72 grid boxes). The purpose of this map is to run the model with 72×72 resolution, but with the standard 36×36 bathymetry. Thus, MOD2X contains four identical grid cells for each grid cell in MOD36. This is done to investigate changes in the model's behaviour purely due to a doubling of the resolution, without bathymetry modifications. Compare Section 2.7.

EO36 An Eocene bathymetry regridded from a finer Eocene bathymetry to the standard Bern3D resolution, as described in Section 2.8.

EO2X Like MOD2X, but for EO36 instead of MOD36.

EO72 An Eocene bathymetry regridded from the same GCM bathymetry as EO36, but with doubled horizontal resolution. In contrast to MOD2X and EO2X, not only the resolution of the model was doubled, but also the resolution of the bathymetry. Compare Section 2.8.2.

With MOD36 and EO72, experiments of plate tectonic rearrangements were performed. For this purpose, dozens of slightly modified versions of both maps were generated. These modifications are described in Sections 2.6 and 2.9.2, respectively.

2.5.2. Input map modifications

The first step in realising an alternative topography in the Bern3D model is to modify the input maps (described in Appendix A) accordingly. If nothing but the bathymetry is changed, only the depth levels in the k1 map has to be modified. On the other hand, if some land boxes are converted into ocean boxes or vice versa, all seven maps must be adapted. The adaptation of the `.k1`, `.bmask`, `.dyemask`, and `.alti` maps is straightforward and only involves the boxes that are being modified. But the adaptation of the `.lmask` and `.psiles` maps includes relabeling of the islands if the number of islands is changed; i.e. if islands are connected by land cells or split up into multiple islands. Finally, the `.paths` file must be modified only if an island is enlarged (which may result in a dry path), or again if the number of islands is changed. In the latter case, a new path must be defined for each modified island.

The `.paths` files are very much prone to error if generated by hand, as was common practice at the time when this master thesis was written. According to the island rule (Godfrey, 1989; Ritz, 2012), the paths must be closed. Depending on the location, a non-closed path may have a small effect on the model, as described in the paragraph below, or it may completely distort the global ocean circulation. The latter has happened during the process of modelling an Eocene steady state in double resolution. Similarly, the exact path that is chosen around an island may also have a strong effect on ocean circulation, as in the example described in Section 3.5.

In the original MOD36 `.paths` file, a meridional section of the path around North and South America was missing. Interestingly, closing this section in the `.paths` file had only a negligibly small effect on the barotropic ocean circulation. It is still mentioned here because the effect on the meridional circulation was non-negligible, namely the maximum AMOC increased from 14.5 Sv to 16.5 Sv. The experiments on Agulhas leakage were carried out with the uncorrected version of the `.paths` file before this error was discovered, the experiments on plate tectonic rearrangements were carried out with the corrected version. As the shape of the AMOC remained largely unchanged, the inferences made from the earlier experiments are still valid, though some numbers would slightly change if the corrected `.paths` file was used.

2.6. Modern-world tectonic rearrangements

In a first series of experiments, various ocean gateways were modified in the standard Bern3D modern world. The Drake Passage was made shallower and finally closed; the Panama Strait was opened, its depth incrementally increased; and the Mediterranean was connected to the Indian Ocean via an open Strait of Suez. These three modifications were then also applied simultaneously, and combinations of two modifications were simulated as well.
The bathymetry modifications are described in more detail in section 2.6.2 and listed in Table 1. Unless stated otherwise in this section, all simulations were carried out using two different methods: Firstly, a pseudo-transient opening series was simulated, as described in the subsection below. Secondly, each bathymetry was run through a separate spinup procedure as described earlier in Section 2.3.

2.6.1. Pseudo-transient simulations

In the pseudo-transient simulations, the first model run with a modified modern topography was restarted from the Nd spinup (spinup 5, see section 2.3) of the standard map (CTRL). Subsequent runs were restarted from the last timestep of the previous run in the pseudo-transient series. Each simulation was run long enough to reach equilibrium. We call this method pseudo-transient because it simulates a chronological series of opening steps, but restarts and interpolations are required for each bathymetry as we have not implemented a

real transient bathymetry modification in the model. When a gateway was opened in the first pseudo-transient step, new ocean grid boxes ("wet boxes") appeared. As the restart fields contained missing values in these locations, the values for the new boxes were set in the model code as follows.

- The EBM sea ice variables were set to atmicea=0 m^2 (area), atmiceh=0 m (height) and atmicet=273 K (temperature). This choice is unproblematic because these are just restart values, the ice is allowed to develop according to the EBM from there on.
- For the two-dimensional climatology of the Dalton number[1], the missing values were replaced by interpolating values of neighbouring boxes.
- The same was done for all three-dimensional tracer fields, including Nd, temperature, salinity and therefore also density. This last step was not only necessary if a land box was opened, but also if an ocean box was deepened.

However, this is a cumbersome method, because the interpolation has to be hardcoded: In many cases, not all four neighbouring boxes are wet, hence specific interpolation formulae have to be applied for every location. The interpolations applied for each gateway are described in Section 2.6.2. For similar future experiments, it is therefore suggested that only separate spinup are made for each different topography, as was done here in parallel. Although the large number of additional spinups greatly increases computation time, this method is less prone to error and more adequate. Furthermore, it allows for more complex topography modifications, because an interpolation need not be possible.

2.6.2. Detailed description of bathymetry modifications

Panama Strait

The Panama Strait is normally closed by two land boxes (Figure 4a). It was opened by converting these into ocean boxes and incrementally increasing their depth. The depth of the two boxes was chosen to be equal at all stages. The maximum depth was 21 layers (2100 m), because this was also the maximum depth of the neighbouring box pairs used for interpolation (see below).

Pseudo-transient Interpolation: Temperature, salinity and density were again interpolated from the two zonally neighbouring grid boxes ($(i-1, j)$ and $(i+1, j)$); if all four neighbouring boxes had been taken into account, the maximum depth of the Panama Strait would have been 12 layers (824 m). The two-dimensional climatology of the Dalton number, which contains only surface values, was interpolated from all four neighbouring ocean grid boxes.

Drake Passage

In the standard setup, the Drake Passage consists of two shallow ocean boxes and a deep ocean box lying inbetween. As shown in Figure 4b, the shallow boxes have 9 (southernmost

[1] The Dalton number is a scaling factor in the EBM evaporation which is dependent on time, longitude and latitude, i.e., monthly values are defined for each surface grid cell.

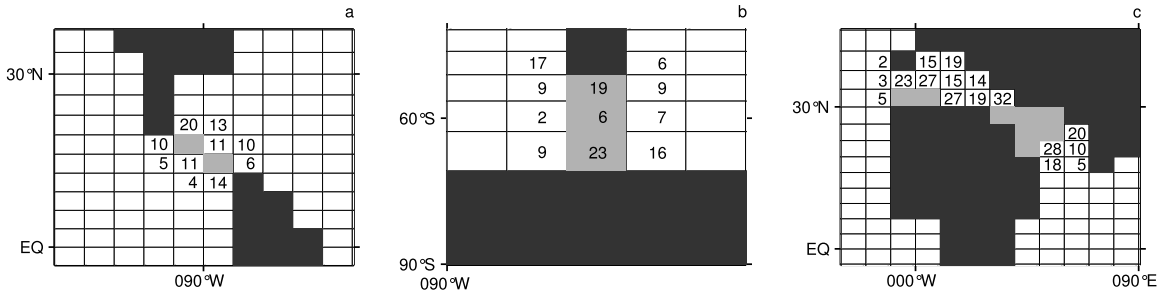

Figure 4: Sections of the standard modern map: a) Panama Strait, b) Drake Passage, c) Strait of Suez. Numbers denote seafloor elevations in the unmodified map. Light grey cells indicate land cells that were opened (a,c) or ocean cells that were closed (b). Dark grey cells are permanent land cells.

box) and 13 depth layers (corresponding to depths of roughly 590 m and 970 m), the deep box 26 layers (3280 m). Instead of gradually closing the passage, it was decided to simulate a world with fully closed Drake Passage to start with. This simulation was done starting from spinup 1, not using interpolation. A low value was chosen arbitrarily for the height of the emerging land cells (80 m), which is not so important because this information is only used for diagnostics. To gradually open the passage, the depth layers were then increased in steps of 2, 5 and 3 layers (south to north) to avoid a narrow deep passage, compare DRA1-5 in Table 1. For simplicity, the boxes adjacent to the three described boxes were not modified. Because the Drake Passage is the main focus of the tectonic rearrangements study, intermediate opening bathymetries (DRI1-11) were created for the shallowest states (DRA3-5). These were used in a separate pseudo-transient experiment series and in separate spinups. Finally, a uniform Drake Passage opening was simulated (only as separate spinups) with bathymetries TRIO31-1, in which all three boxes are lowered uniformly. The results of these opening experiments are shown in Section 3.2.2.

Pseudo-transient Interpolation: Temperature, salinity and density were interpolated from the two zonally neighbouring grid boxes ($(i-1,j)$ and $(i+1,j)$) if these do not contain missing values. If one of the two values was missing, the value of the other neighbour is simply copied into the new cell. The case that both values were missing did not occur. Because the new ocean cells have land cells as meridional neighbours, the Dalton number (which is only defined for ocean cells) was also interpolated from the two zonal neighbours.
TRIO31-1 simulations were only carried out as separate spinups, partly because the lowermost cells could not have been interpolated and partly because of the limitations of the pseudo-transient method (compare Section 3.2.2).

Strait of Suez

Figure 4c shows the Mediterranean bathymetry in the standard modern map. The Mediterranean can be connected to the Indian Ocean by opening 4 land cells, creating a narrow Strait of Suez. However, the innermost Mediterranean ocean box is just 1 layer deep, therefore its depth was adjusted to the depth chosen for the 4 new ocean boxes. This depth was varied from 2 to 19 layers (81 to 1576 m), where the maximum depth was again limited by the neighbouring ocean boxes. In subsequent experiments, the Strait was widened by 3 additional ocean boxes. In one experiment, the Gibraltar Strait was also widened by opening 2

land cells and deepening 3 ocean cells, with the objective of stimulating the Suez throughflow.

Pseudo-transient Interpolation: Because values in most new ocean boxes cannot be interpolated from neighbouring boxes, two reference boxes adjacent to the newly opened strait were chosen for the interpolation: one in the Mediterranean, one in the Indian Ocean. The new boxes were then filled by weigthed averages of the two reference boxes as follows: $V_i = \frac{1}{n}(iV_I + (n-i)V_M)$, where $i = 1, ..., n$ is the index of the box, counting from the Mediterranean to the Indian Ocean, and V_M and V_I are the values in the reference boxes. This was done for the 2D-fields and each layer of the 3D-fields. For the widening of Gibraltar Strait, a similar interpolation was performed.

Drake Passage opening with open Panama Strait

The Drake Passage bathymetry modifications were also applied to a map with opened Panama Strait. A Panama Strait depth which showed an average Panama throughflow was chosen for these combined simulations (PAN2, compare Table 1 and Section 3.2.2). The Drake Passage modifications were identical to DRA1-DRA5, DRD1-11 and TRIO31-1. For the same reasons as TRIO31-1, TRIC31-1 simulations were only carried out as separate spinups.

Combinations with open Strait of Suez

Only one of the tested Strait of Suez bathymetries resulted in a throughflow (SUE6, compare Table 1 and section 3.2.1). This bathymetry was combined with an open Panama Strait (SP1) to see wether the Panama throughflow strengthens the Suez throughflow. Combinations with the most interesting configurations with open Panama Strait and shallow/closed Drake Passage were also investigated (SPD1-2). These were not simulated using interpolations, but only with separate spinups.

Table 1: Bathymetry of three mayor ocean gateways (Drake Passage, Panama Strait and Strait of Suez) for all experiments on modern world tectonic rearrangements. CTRL is a standard modern world simulation. The other simulations were made with bathymetries that are modified only in the regions specified in the table. Numbers correspond to seafloor elevation k in model layers, as in the `.k1` map (compare Section 2.1.1). Drake cell elevations are listed from north to south; for Panama Cell elevations, only one number is given, which was applied to both Panama boxes. For the Strait of Suez, the number with an 'I' prefix denotes how many model boxes next to the Indian Ocean were either opened or deepened; the number with an 'A', how many boxes next to the Atlantic were so altered; and the last number denotes the elevation which is equal for all these modified boxes. Where run names are given instead of numbers, the elevations are equal to the ones in that run. Blank space means that the elevations are equal to the above specified elevations.

Experiment	**Drake Cells**			**Panama Cells**	**Suez Cells**	
	53.7°S	59.4°S	66.4°S	both cells	cf. caption	
CTRL	19	6	23	closed	closed	
DRA1	22	11	25			
DRA2	25	16	27			
DRA3	28	21	29			
DRA4	31	26	31			
DRA5			closed			
DRD1-5	31	31-27	31			
DRD6	31	26	31			
DRD7-10	30	25-22	30			
DRD11	28	21	29			
TRIO31-1	31-1	31-1	31-1			
PAN1	19	6	23	11		
PAN2				16		
PAN3				21		
PAN4				27		
PAN5				31		
PD1	22	11	25	16		
PD2	25	16	27			
PD3	28	21	29			
PD4	31	26	31			
PD5			closed			
PDD1-11			DRD1-11			
TRIC31-1	31-1	31-1	31-1			
SUE1	22	11	25	closed	I5	18
SUE2					I5	25
SUE3					I5	31
SUE4					I5	14
SUE5					I8, A5	14
SUE6					I8	14
SP1				16		
SPD1	31	26	31			
SPD2			closed			

2.7. From standard to double resolution

In principle, the resolution of the Bern3D model may easily be varied by modifying the number of grid cells in the model's variable definition routine (var.cmn.F). However, several additional adaptations had to be made:

- In order not to violate the CFL criterion for numerical stability (compare, e.g., Stocker (2011)), a finer spatial resolution also requires a shorter time step. Double resolution simulations were therefore run with 192 instead of 48 timesteps per year.
- Memory problems occured due to the higher spatial and temporal resolution which increased the size of some EBM matrices by a factor of 16. The structure and allocation of the problematic matrices was modified by Stefan Ritz, solving the memory problems.
- All input fields for the Bern3D model had to be newly regridded to the doubled resolution. This includes temperature and salinity restoring fields; zonal and meridional wind stress; two-meter atmospheric temperature and evaporation fields for the Dalton Number diagnosis; surface wind speed, moisture advection, and cloud cover for the EBM. Additional fields would be required if the BGC module was to be used in the double resolution simulations.
- For modern-world experiments, a double resolution land albedo climatology is also needed. However, because the impact of the albedo on the model climate is so large, it was decided not to regrid the original albedo climatology to the new resolution, but to read in the 36×36 albedo climatology and double it in the code. In that way, the land albedo is exactly the same in the CTRL and MOD2X simulations. A spatially invariant land albedo was chosen for Eocene simulations (compare section 2.9.1).
- The freshwater flux in the Ross and Weddell Sea regions, which are hardcoded in the model, was turned off for all double resolution experiments (including MOD2X).

2.8. Eocene bathymetry

To simulate the impact of the opening of Drake Passage in a more realistic setting, an Eocene paleobathymetry is needed. Figure 5 shows the bathymetry on the HadCM3 model grid, which has been kindly provided by P. J. Valdes (pers. comm.). The interesting differences to the modern-world map are not described here, but in Section 2.8.2. The same bathymetry has been used for Eocene simulations with the HadCM3 model and represents the boundary conditions of ca. 55 Myear before present (Lunt et al., 2010; Tindall et al., 2010). Its horizontal resolution is 3.75° in longitude and 2.5° in latitude (equally spaced for all latitudes, unlike in the Bern3D model). Therefore, it must be regridded to the coarser Bern3D standard resolution. The 20 depth levels of the original bathymetry also correspond to the HadCM3 ocean layers. Compared to the Bern3D resolution (see Section 2.1.1), the HadCM3 resolution is finer near the ocean surface (10 m in the uppermost layers) and coarser in the deep ocean (616 m in the lowermost layers; Collins et al. (2001); Johns et al. (1997)). The shallowest cell of the Eocene bathymetry is 67 m deep, corresponding to 6 HadCM3 ocean layers. The original bathymetry hence only consists of 15 different depth levels. However, as these are averaged to the coarser Bern3D horizontal grid cells, intermediate depths arise, such that the final Bern3D Eocene bathymetry still uses the full vertical resolution of 32 layers. In addition to the bathymetry, P. J. Valdes has also provided a land/sea (1/0) mask, which was also used in the regridding process, as described below.

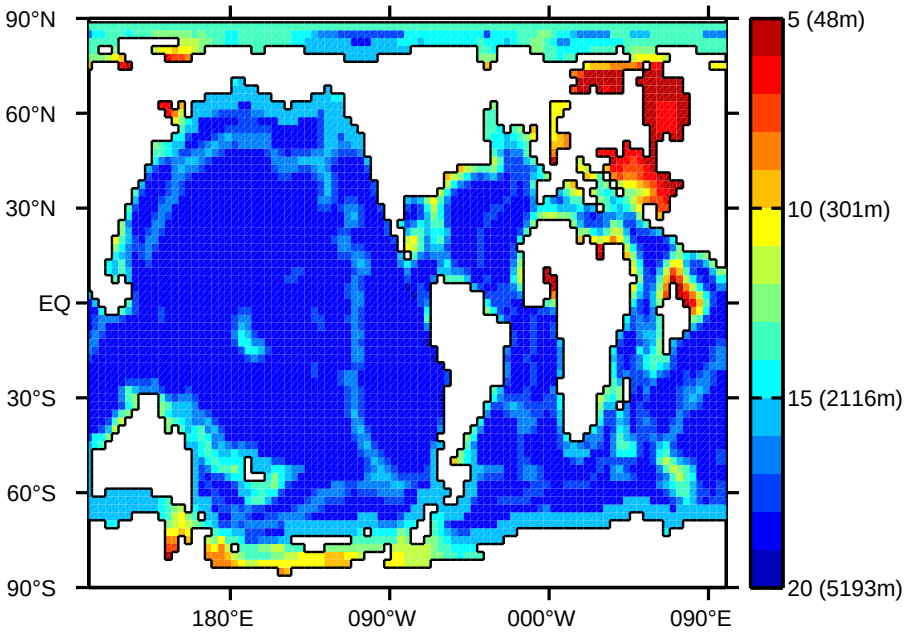

Figure 5: HadCM3 Eocene bathymetry as provided by P. J. Valdes (pers. comm.). Colors indicate HadCM3 depth levels as described in Section 2.8. The depth in meters is indicated next to the depth levels.

2.8.1. Creating the input maps from the original bathymetry

In a first step, the HadCM3 bathymetry was regridded to the Bern3D model grid. An overview of this regridding process is given here, a more detailed description can be found in Appendix B. The land cells were set to zero in the original HadCM3 bathymetry, such that all Bern3D cells that overlapped one or more HadCM3 ocean cells recieved a non-zero ocean depth value after the interpolation. This resulted in much too small land masses, but a complete coverage of ocean depths. The size of the land masses was later corrected using the HadCM3 land/sea mask. This binary mask was regridded, resulting in a Bern3D grid mask with values between zero and one. All boxes that contained significantly more land than ocean in this mask (as specified below) were then converted into land boxes in the Bern3D bathymetry. Inconsistencies in the bathymetry were then removed by hand. Finally, the seven Bern3D input maps were generated from the bathymetry.

In a second step, the seven input maps (compare Appendix A) were created from the regridded bathymetry. The templates for the input maps were generated from the bathymetry in matlab, and finalized by hand. For the `.k1` map, all missing values were replaced by the number $91 - 94$ depending on the runoff direction, as described below. The `.bmask`, `.lmask` and `.dyemask` files were generated as differently labeled land-sea masks; the differentiation into regions was done by hand. As the land temperatures were not diagnosed in Eocene simulations, the `.alti` mask simply was generated as a land-sea mask with a value of 100 for each land cell. For the `.psiles` file, the conversion of the land-sea mask onto the edge grid was done by a MATLAB script, the numbering of the islands was done by hand. Finally, the `.paths` file was completely done by hand, which is a possible source of errors, as discussed in Section 2.5.2. For simplicity, as in the original MOD36 file, the paths were chosen to be as close to rectangular as possible. Near the end of this master thesis, Stefan Ritz wrote a MATLAB script that automatically generates paths directly following the coastlines. While this script has been tested and works well for various coarser resolutions, it could not be used to generate the `.paths` file for EO72 and similar 72×72 maps, because the complicated coast shapes provided ambiguous information to the script.

The runoff map was qualitatively adapted from the HadCM3 Eocene river routing map, as seen in Figure 1(e) of the supplementary material to Lunt et al. (2010). As an exception, no runoff was allowed into the Arctic Ocean, to reduce the freshening of this nearly isolated water mass. The Bern3D runoff map for EO36 is shown in Figure 6, for EO72 in Figure 9.

2.8.2. Eocene bathymetries

Figure 7 shows the preliminary regridded Eocene bathymetry EO36 in the standard resolution. The Arctic Ocean is not resolved because it spans only roughly half of the northernmost grid box. Also near the South Pole, important features are missing and the bathymetry of the Drake Passage region does not resemble the original bathymetry (Figure 5). Apart from these significant issues, the main features of the bathymetry are captured reasonably well. But the coarse resolution also causes additional problems, such as a high drag (compare Sec-

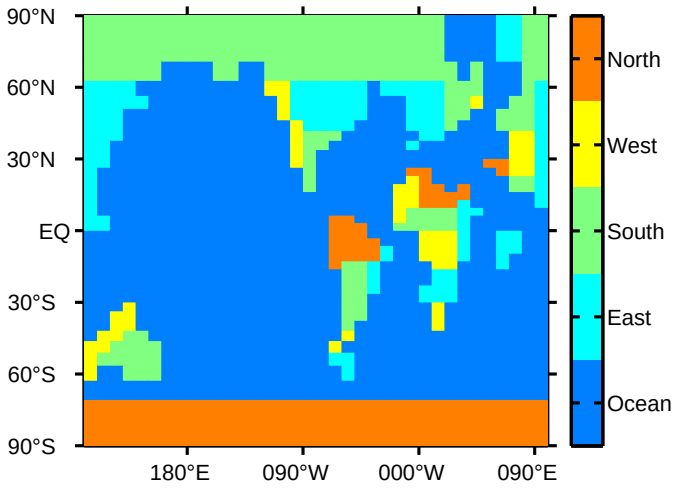

Figure 6: Runoff map for Eocene simulations with standard Bern3D resolution (EO36).

tion 2.2.1) in most cells of the very narrow central Atlantic.

Figure 8 shows the Bern3D Eocene bathymetry EO72 with double resolution, which was also used as a base for Eocene tectonic rearrangements. While the resolution near the poles is still much coarser than in the HadCM3 bathymetry (Figure 5), it is sufficient to resolve the most important features, such as the Arctic Ocean and the island obstructing Drake Passage. This island is a special topographic feature of the early Eocene which will eventually become part of the Antarctic Peninsula. The gap between this island and Antarctica is a shallow seaway that is suggested to have opened before the opening of Drake Passage (Lawver and Gahagan, 1998), but its impact on ocean circulation was probably much smaller.

Further interesting features of the map are listed in the following. The Tasmanian Gateway, which separates Australia from Antarctica, is very narrow and shallow. Europe is connected to North America due to a broadly closed Bering Strait, but separated from Asia by very shallow ocean regions. These are remnants from the Tethys Sea, which also forms a broad Tethys Seaway in today's Suez region. The Panama Strait is wide open and very deep. South America is much closer to Africa than in the modern world, resulting in a narrow Atlantic and a vast Pacific. India is an island east of Africa and not yet connected to Asia.

2.9. Eocene simulations

2.9.1. Model adaptations

The following EBM modifications were made for Eocene simulations:

- Following Lunt et al. (2010), the land albedo α was set to be equal in all land cells, corresponding to land covered with shrub. An average albedo for deciduous shrub from AVHRR satellite data was used, $\alpha = 0.186$ (Wei et al., 2001).

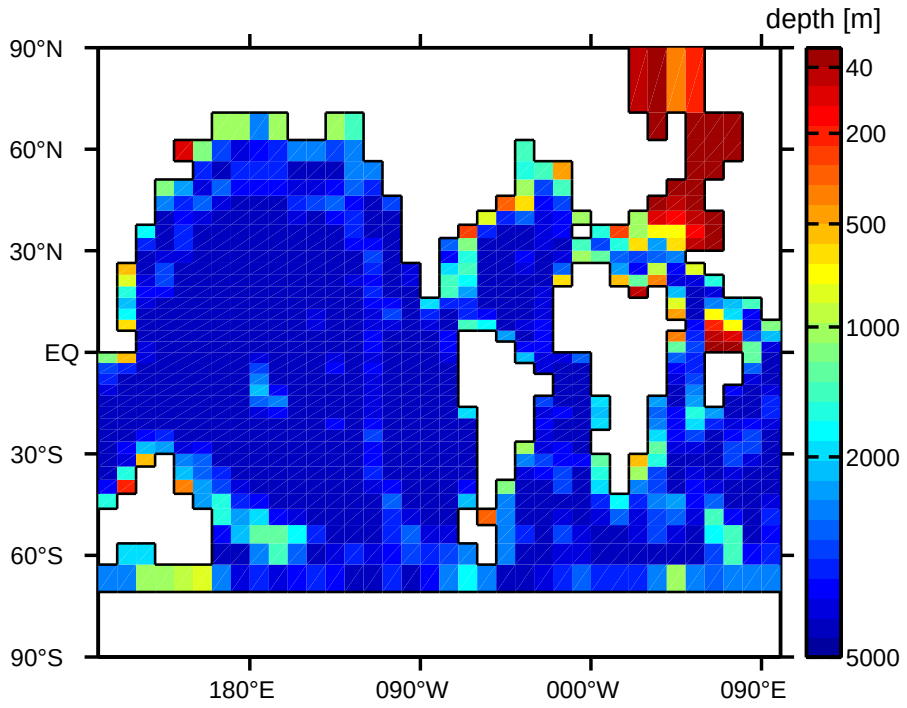

Figure 7: Regridded Eocene bathymetry with standard Bern3D horizontal resolution (36×36 grid cells). Colors show the seafloor elevation k in layers of exponentially decreasing height, and correspond to the depths calculated in equation 1. Some depths in meters are indicated next to the color bar.

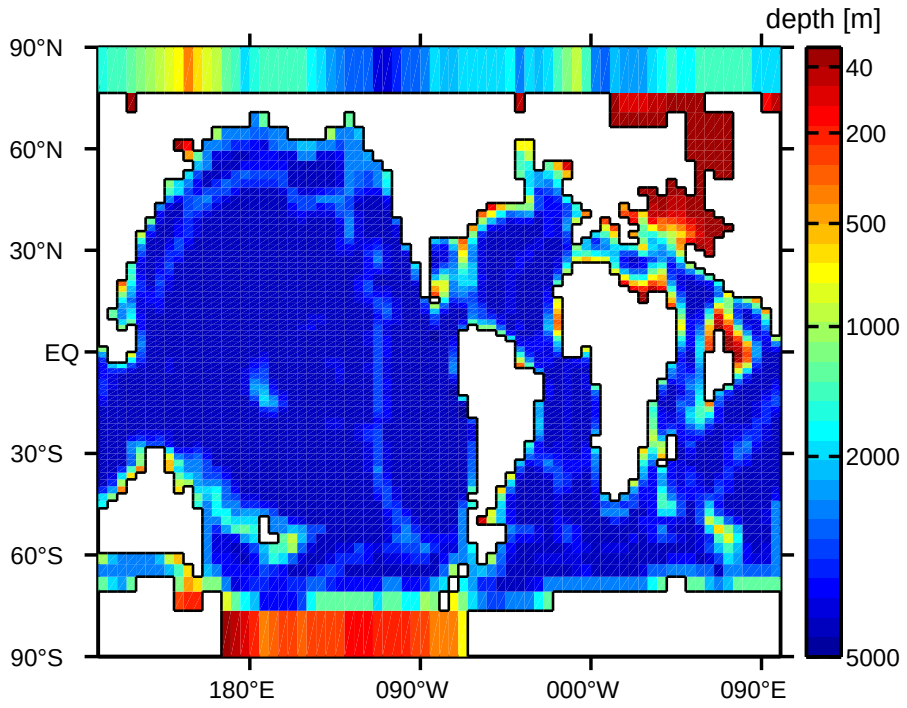

Figure 8: Regridded Eocene bathymetry with double Bern3D horizontal resolution (72×72 grid cells). Colors show the seafloor elevation k in layers of exponentially decreasing height, and correspond to the depths calculated in equation 1. Some depths in meters are indicated next to the color bar.

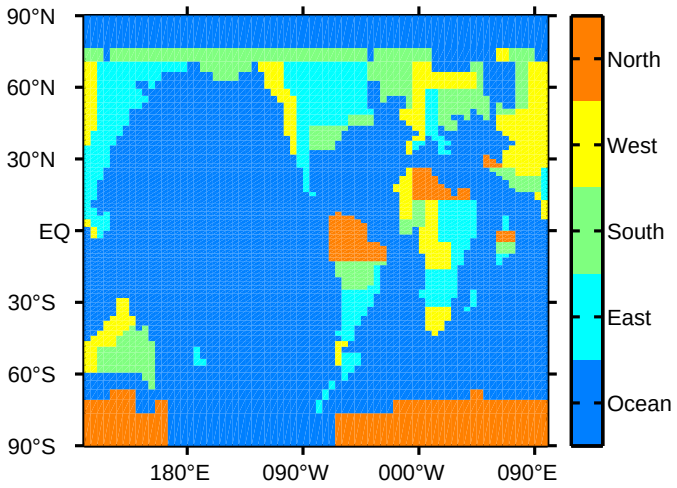

Figure 9: Runoff map for Eocene simulations with doubled Bern3D resolution (EO72).

- In the standard modern setup of the EBM, the fraction of precipitation which is transported back into the ocean via runoff is different for each continent, according to data (Ritz et al., 2011). An average fraction of 0.4 was chosen for all continents in Eocene simulations.

- Two-dimensional EBM input fields for two-meter atmospheric temperature, evaporation, and surface wind speed are read in for modern simulations. These fields are heavily influenced by the locations of the continents and, if unaltered, transport a modern signature to the Eocene simulations (visible, e.g., in the SST). Therefore, the fields were zonally averaged. This also results in a zonally averaged Dalton Number, but the evaporation output of the Eocene simulations is still zonally resolved due to the temperature dependence of the evaporation (compare Equation 12 in Ritz et al. (2011)).

2.9.2. Eocene tectonic rearrangements

In EO72, the wide open Panama Strait and Strait of Suez were not modified. The Drake Passage was closed from both sides (North and South) of the Antarctic island. From the North, only one grid cell with a normal depth of 22 layers (2300 m) needed to be closed to connect the island to South America. From the South, four Antarctic cells of depths between 6 and 12 layers (345 m to 825 m) were closed. For each cell, three stages were simulated: normal (unmodified depth), shallow (depth reduced to 4 layers), and closed (ocean cell replaced by land). The Drake Passage was also widened by shrinking and removing the Antarctic island, and deepening three cells in the Drake region that were below 16 layers deep. This was done to reduce the drag and stimulate throughflow (compare Section 2.2.1).

Furthermore, the Tasman Gateway was also modified: normal, shallower, deeper and closed stages were tested. For the shallower and closed stage, it was sufficient to modify one cell. For the deeper stage, all 10 cells between Antarctica and Australia with a depth smaller than 16 layers were deepened. Combinations of modified Drake Passage and Tasman Gateway

were also systematically simulated as listed in Table 2.

Table 2: Bathymetry of two mayor ocean gateways (Drake Passage and Tasman Gateway) for all experiments on Eocene tectonic rearrangements. EO72 is a standard Eocene simulation (Spinup 3). The other simulations were made with bathymetries that are modified only in the regions specified in the table. Section 2.9.2 specifies how many boxes correspond to the regions Drake N (North), Drake S (South) and Tasman. Each adjective in the table corresponds to a specific seafloor elevation level (compare Section 2.1.1) of these boxes: normal=unmodified; shallow=29; deeper=15 (lower drag, Section 2.2.1); open=15, land cell replaced by ocean; closed=ocean cell replaced by land. Where a run name is given instead of an adjective, the elevations are equal to the ones in that run. Blank space means that the elevations are equal to the previous specified elevations. In bathymetries marked with an asterisk, the Antarctic island is fully open (middle box also); with two asterisks, three shallow cells in the Drake region are deepened in addition to that.

Experiment	**Drake N**	**Drake S**	**Tasman**
EO72	normal	normal	normal
TOP1	shallow		
TOP2	closed		
TOP3		shallow	
TOP4		closed	
BOT1	normal	shallow	
BOT2		closed	
BOT3	shallow		
BOT4	closed		
TAS1	normal	normal	shallow
TAS2			closed
TAS3			deeper
STOP1-4	TOP1-4	TOP1-4	TAS1
CTOP1-4			TAS2
OTOP1-4			TAS3
SBOT1-4	BOT1-4	BOT1-4	TAS1
CBOT1-4			TAS2
OTOP1-4			TAS3
WIDE1	normal	open	normal
WIDE2	open	normal	
WIDE3		open	
WIDE4*			
WIDE5**			
WIDE6**			deeper

2.10. Neodymium experiments

The Nd implementation in the Bern3D model is described in Rempfer et al. (2011). Three sources of Nd are included: rivers, dust and continental boundaries. None of these were modified for the experiments made for this thesis. A control run was made and compared to the results of Rempfer et al. (2011). Thereafter, all experiments in Table 1 were repeated with Nd, except those with an open Strait of Suez because the influence on the ocean circulation was too small. These experiments were performed as separate spinups as well as pseudo-transient simulations, as described in Section 2.6.1. In all cases, Nd simulations were

run for 20,000 years to ensure equilibrium.

In this thesis, we are especially interested in seafloor values of ϵ_{Nd}, because those can be compared with data from marine sediment cores (Section 3.2.3). To test the hypothesis that Drake Passage opening increases ϵ_{Nd} east of Drake Passage, we compare the model results with data from sediment cores at two sites, ODP site 689 and 1090. These are shown in Figure 10. We cannot simply compare the data with the simulated ϵ_{Nd} value of the gridbox containing the site, because no model provides reliable results on a one-gridbox level. Therefore, we take the mean of this cell's lowermost and second to lowermost layer, and the two lowest layers of its nearest horizontal neighbours, which are also shown in Figure 10. Thus, we average over a total of 18 grid cells around site 1090, and over 12 cells around site 689. While the seafloor elevations of the nearest horizontal neighbours differ from the cells containing the ODP sites, all averaged sites are deep ocean cells (elevation smaller or equal to six layers), such that they have no boundary source. One of the sites around site 689 has an elevation of six layers, such that the layer above it already has a boundary source; but this had only a very small effect on the 12-box average, therefore the averaging method was not modified.

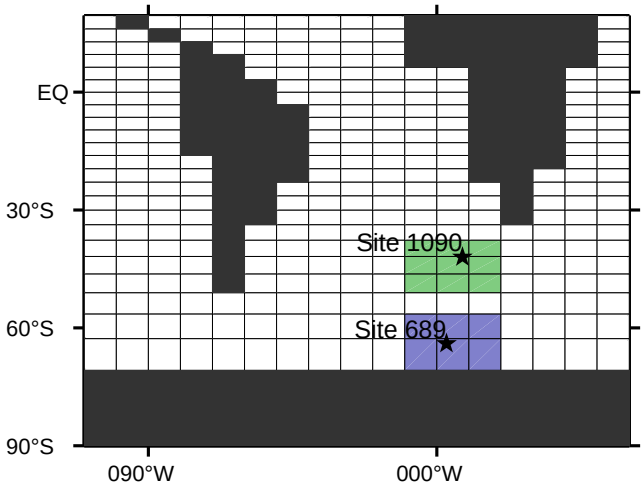

Figure 10: Locations of ODP sites 689 and 1090, and seafloor grid cells that were averaged to compare with site 689 (blue) and 1090 (green).

For Nd simulations with the Eocene map, the boundary source would have to be completely redefined. It could not simply be regridded because it is only defined at the continental margins. This was not done here because it is beyond the scope of this thesis.

3. Results and Discussion

3.1. Agulhas leakage experiments

3.1.1. Leakage location: dye tracer experiments

A dye tracer flux as described in Section 2.4 was prescribed in various single grid boxes around Cape Agulhas. Even for inlet boxes located east of South Africa, a discernible tracer flux into the Atlantic was recorded, i.e. a water mass flow around the Cape. An example is given in Figure 11 (Location 1), where the tracer source was located at the ocean box just east of Africa's southernmost land box. The surface distribution of the dye tracer after 400 years of constant influx is shown. The model simulates a similar pathway of water masses from Cape Agulhas into the Atlantic as the observed track of Agulhas rings (compare, e.g., Figure 1 in Beal et al., 2011). It can be seen that part of the tracer concentration is also advected eastwards by the Antarctic Circumpolar Current (ACC) and distributed into the Pacific and Atlantic thereafter. After 1000 years, the surface distribution is nearly homogeneous in all ocean basins.

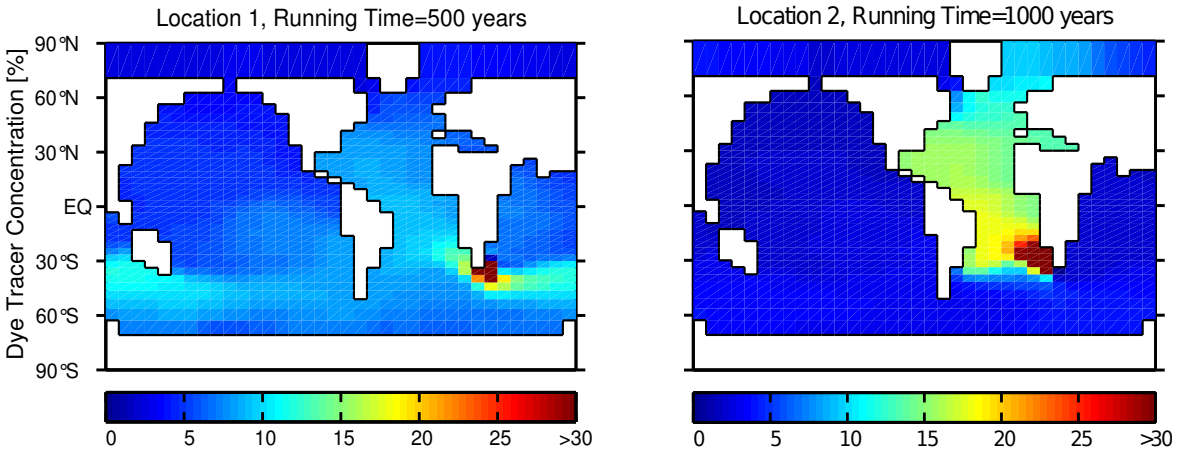

Figure 11: Dye tracer distribution from two different inlet positions L1 and L2 (compare Figure 12). On each map, the inlet position is the only grid box with a 100 % dye tracer concentration. The distribution starting from Location 1 is plotted after 500 years, because the pathway of Agulhas leakage is less visible after 1000 years.

Therefore, a more suitable inlet position has to be found in order to investigate the impact of Agulhas leakage on Atlantic Salinity and AMOC. The box southwest of the southern tip of Africa is ideal, as water masses starting from there are distributed into the entire Atlantic, but barely affect any other basin (Figure 11, Location 2). Therefore, this location was chosen for the salt or freshwater influx in most of the follow-up freshwater perturbation experiments. Figure 12 shows this location (L2) and all other grid boxes that were used.

Although a water mass transport similar to the Agulhas leakage is found in the Bern3D model, it has to be noted that the model resolution is much too coarse to resolve the real,

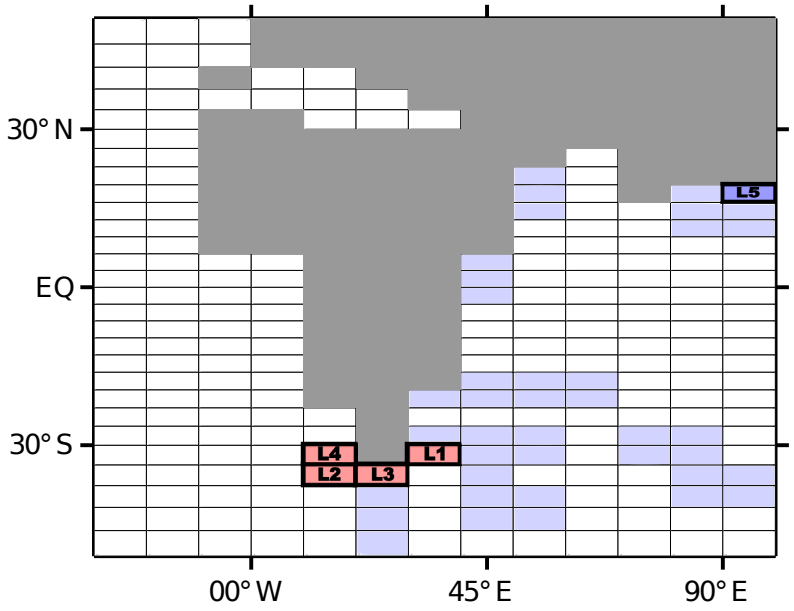

Figure 12: Section of the Bern3D grid, including Africa and parts of the Atlantic and Indian Ocean. Red grid boxes L1-L4 were used as freshwater or salt influx locations, the blue box L5 was used for dipole compensation (section 3.1.4). Light blue boxes were tested in dye tracer experiments, but not chosen for freshwater experiments.

eddy-driven phenomenon. The dye tracer transport in the model is mainly due to advection by the near-surface currents shown in Figure 13. Therein, Agulhas retroflection is visible: Part of the Agulhas current along the east coast is reflected back into the Indian Ocean gyre. Another part leaks into the South Atlantic around cape Agulhas, not in the form of Agulhas rings but as a 'normal' surface current. Part of this leakage current feeds into the Atlantic gyres; but part of it also flows northward all the way, until reaches the regions of NADW formation. This explains the impact of Agulhas freshwater perturbations on the AMOC that we will investigate in the following sections.

3.1.2. Single freshwater pulses at cape Agulhas

First freshwater experiments were carried out with single perturbation fluxes of rectangular (flux on/off) and triangular shape in time (flux increasing, then decreasing linearly). The duration of the perturbation was varied from 100 to 2000 years, the maximum amplitude from 0.02 to 25 Sverdrups. Although pure freshwater perturbations of more than 1 Sv are unrealistic, it is interesting to investigate the model response to extreme pulses as well. The flux inlet location was only slightly varied in these experiments, it was chosen to be either the single grid box in location two of Figure 11 (denoted L2 in the following) or the single grid box just east of it (L3, compare Figure 12). The difference in AMOC patterns resulting from perturbations at L2 or L3 is only very small. The impact of the freshwater perturbation on AMOC strength was examined by plotting the time evolution of the AMOC maximum. The AMOC maximum of the unperturbed Bern3D model is approximately 14.5 Sv.

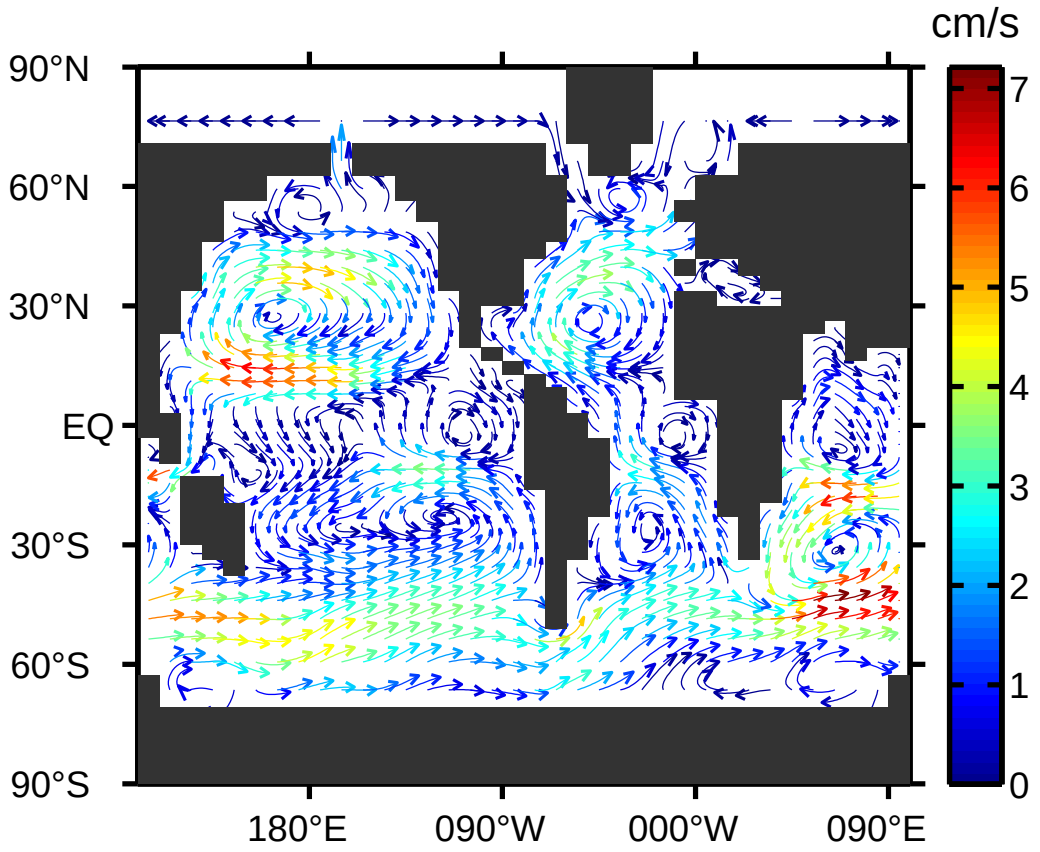

Figure 13: Near-surface currents in the Bern3D control run (CTRL). Water mass velocities averaged over the six topmost ocean layers are shown, corresponding roughly to the top 300 metres. Colors indicate water mass speed in $\mathrm{cm\,s^{-1}}$.

One would expect a decrease in AMOC strength if freshwater is injected into the Atlantic via Agulhas leakage, because the freshwater is transported along the ocean surface to the region of North Atlantic Deep Water formation. The salty surface water in this region is therefore freshened, decreasing its density and in turn slowing down the sinking of water masses and weakening the AMOC. This effect is indeed recorded in the Bern3D model, as shown in Figure 14. When the maximum amplitude of a 200-year-long, triangular freshwater perturbation at L2 is increased step by step from 0.1 to 7 Sv in a series of simulations, the AMOC decreases accordingly. Up to a perturbation strength of 5 Sv, the AMOC partly recovers some 2000 years after the perturbation. Forced by a 6 Sv perturbation, it reaches a minimum at around 2 Sv: the AMOC is almost completely shut down. After this disturbance, the AMOC recovers much more slowly than after smaller perturbations, reaching 12Sv after around 7000 years. In the case of a 7 Sv perturbation, the AMOC does not recover even after 20,000 years.

It is hypothesized that this "AMOC-off-state" is a second equilibrium of the Bern3D model. Figure 14 shows that for perturbations above 6 Sv, the AMOC is forced into the 2 Sv minimum even if this value is not reached during the perturbation. Stronger perturbations of up to 10 Sv lead to the same final state as the 7 Sv disturbance. The hypothesis is supported

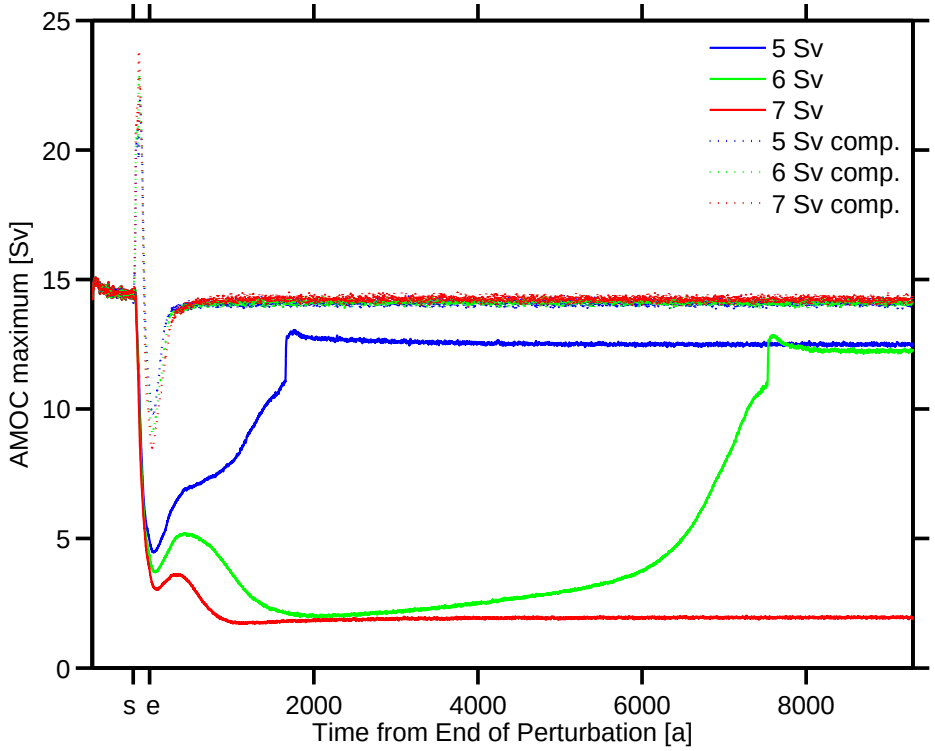

Figure 14: Temporal evolution of the maximum AMOC strength in response to a freshwater perturbation at Cape Agulhas (L2) of 5 Sv (blue line), 6 Sv (green) and 7 Sv (red). 's' and 'e' denote the start and end of the 200 year long, triangular perturbation. Solid lines show uncompensated freshwater perturbations, dotted lines show the corresponding (all-box) compensated perturbations.

by the fact that the off-state may also be reached by a weaker perturbation at L3 (0.5 Sv) of longer duration; such perturbations of length 1500 or 2000 years result in virtually the same state (AMOC maximum difference around 0.1 Sv). It is notable that for even stronger perturbations, the AMOC maximum does not become as low as 2 Sv, but increases from around 4 Sv at a 15 Sv perturbation to almost 9 Sv at a 25 Sv perturbation. This indicates that these perturbations are too strong to reach the off-state equilibrium. It has to be mentioned that the off-state—in all experiments that produce it—is reached not only due to the local freshwater perturbation, but also due to the reduction of the global salinity caused by the lack of freshwater flux compensation.

In a second experiment, the Agulhas freshwater perturbations were compensated by adding a small salt influx to all unperturbed boxes. This is also shown in Figure 14 by the dotted lines. The initial AMOC strengthening following the onset of the compensated freshwater perturbations is caused by the all-box compensation: The compensating freshwater flux out of the ocean in all grid cells (including the North Atlantic region) has a faster impact on the AMOC than the Agulhas freshwater perturbation. Roughly 50 years later, enough freshwater has been advected into the North Atlantic region to overrule the compensating effect. Thereafter, the AMOC is weakened, but only by a factor of roughly 2 less than in the uncompensated case. After the perturbation vanishes, the AMOC recovers almost to its original strength (-0.3 Sv at the most), even for much stronger perturbations than 7 Sv. We infer that an "AMOC-off-state" equilibrium only exists in the uncompensated case.

While freshwater influxes are interesting to investigate the model response, the observed phenomenon of Agulhas leakage is a salt influx into the South Atlantic. Similar experiments were made as with the freshwater influx: Varying amounts of freshwater were taken out at the grid boxes L2 or L3 (compare Figure 12) to simulate the salt influx. This should eventually strengthen the AMOC because the salt is transported along the surface towards the Arctic, where it increases the surface water density and thus accelerates the sinking of the water masses. Figure 15 shows the AMOC response to negative freshwater perturbations of 5 Sv to 7 Sv, in analogy to Figure 14. If the perturbations are not compensated, an AMOC strengthening was indeed recorded in the simulations, as long as the perturbations are not unrealistically strong (>15 Sv). For example, for a triangular 5 Sv perturbation over 200 years, the AMOC reaches a new equilibrium with a maximum of around 18 Sv. The lag of the AMOC response is around 15 -25 years for triangular perturbations (depending on perturbation strength), down to 5 years for rectangular forcings. For strong perturbations, the new AMOC equilibrium is preceded by major oscillations in AMOC strength.

If the Agulhas leakage is compensated in all other grid boxes (as shown by the dotted lines in Figure 15), the model recovers its initial equilibrium state after the perturbation vanishes. Also, the observed impact on the AMOC during the perturbation is not a strengthening, but a weakening, because the compensating freshwater input in all grid boxes (including the North Atlantic region) is more direct than the Agulhas influence and large enough to overrule it completely. Applying only the compensation flux (without the perturbation at Cape Agulhas) has a similar impact on the AMOC, implying that the impact of the compensation is much stronger than that of the perturbation which should be investigated. Therefore, the freshwater compensation in all boxes was not used for the following experiments.

3.1.3. Periodic freshwater forcings and impact on AMOC seasonality

Without any freshwater compensation, the impact of the temporal shape of the freshwater forcing on the AMOC response was investigated. The previously used rectangular and triangular forcing were compared to periodic forcings consisting of one to four triangular pulses per year. The periodic triangular pulses were chosen to occur at regular intervals, the periods between pulses being as long as the pulses themselves (see Figure 16). For a fixed net salt flux, this causes more frequent perturbations to be shorter, but their amplitude is independent of the pulse frequency. Beal et al., 2011 state that 4-6 Agulhas rings occur per year, but because a low temporal resolution of 48 timesteps per year was chosen for our experiments, no more than 4 rings were simulated. It was found that the shaping of the perturbation has a discernible influence on the amplitude of the AMOC disturbance during the perturbation, as shown in Figure 17. The rectangular perturbation causes the largest AMOC increase, followed by the triangular perturbation. The initial overshoot of the AMOC maximum is even smaller for periodic forces, and decreases further if the pulses occur less frequently. This may possibly be explained by the fact that there are short unperturbed time periods between

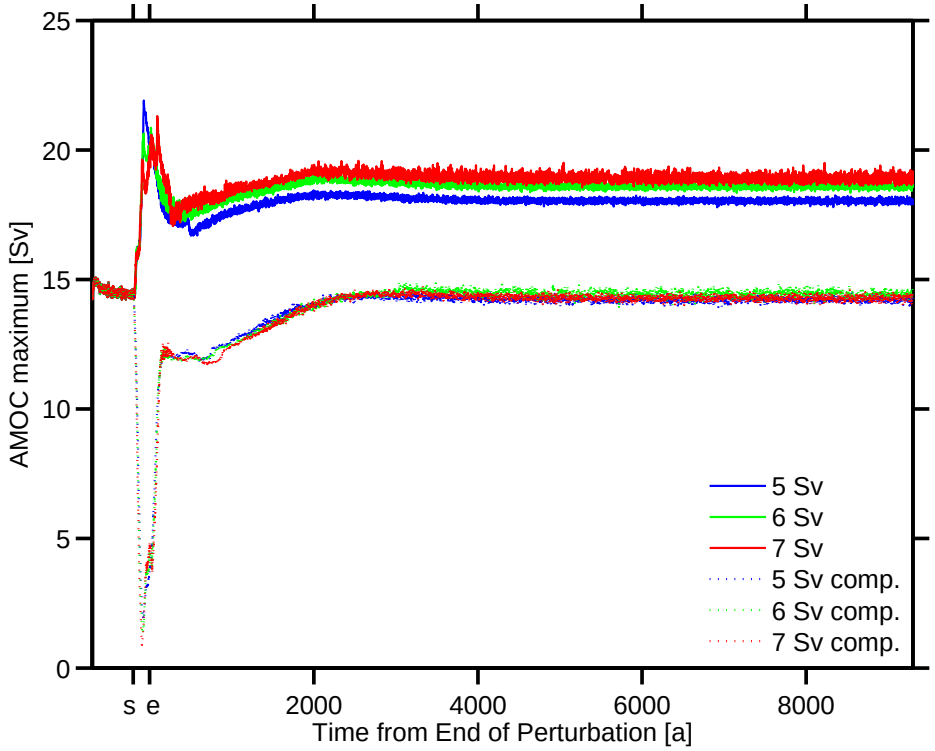

Figure 15: Temporal evolution of the maximum AMOC strength in response to a negative freshwater perturbation at Cape Agulhas (L2) of 5 Sv (blue line), 6 Sv (green) and 7 Sv (red). 's' and 'e' denote the start and end of the 200 year long, triangular perturbation. Solid lines show uncompensated freshwater perturbations, dotted lines show the corresponding compensated perturbations.

the periodic pulses, which allows the AMOC to adjust to the new salinity distribution and remain closer to equilibrium. These periods are longest in the case of only one pulse per year (compare Figure 16), which is why the overshoot is smallest for this case. However, the temporal shape of the freshwater perturbation has no impact on the AMOC maximum in the new equilibrium after the perturbation ceases. This is expected, because the amplitudes of the forcings were chosen such that the total loss of freshwater is the same in all cases. The AMOC amplification after the perturbation is caused by the increased global salinity due to the lack of freshwater compensation.

The unperturbed AMOC seasonality of the Bern3D model is shown in Figure 18a. In agreement with the measured AMOC seasonality (Kanzow et al., 2010), a spring minimum is found; for the rest of the year, Kanzow et al. (2010) find an Autumn maximum, but not a regular bi-annual oscillation as recorded in our model. This oscillation is probably mainly caused by the seasonal shift of shuffling convection regions, which is shown in Figure 19a-d. The seasonal changes in the mixing convection are much smaller than in the shuffling convection, because the latter is applied before the mixing convection.

To determine the effect of an Agulhas salt perturbation on this seasonality, five time series of the AMOC maximum were recorded over a period of 10,000 years, one for each different perturbation shape (compare Figure 17). The starting year was denoted 2000, and an Agulhas leakage salt flux of 1 Sv was introduced from 2100 to 2300. For the analysis, the time series

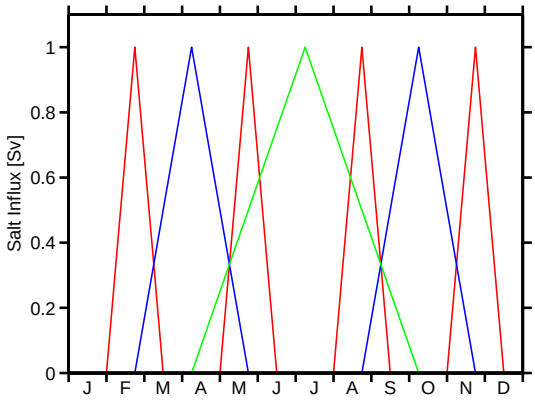

Figure 16: Seasonalities of the periodic salt perturbations, realized as negative freshwater perturbations, simulating 1-4 Agulhas rings per year. The colors used correspond to the ones in Figure 17, where the response of the AMOC on these perturbations is shown.

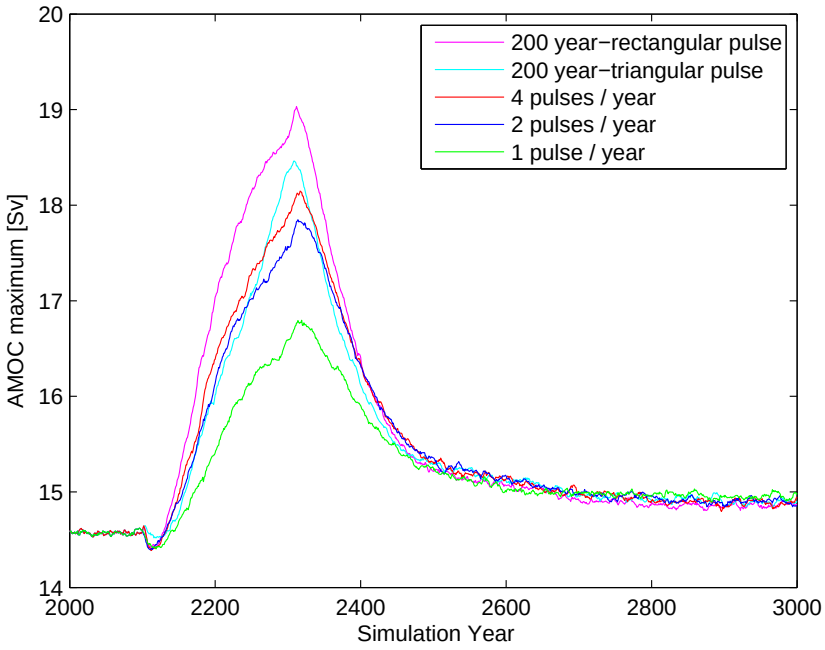

Figure 17: Temporal evolution of the maximal AMOC strength in response to salt influxes at Cape Agulhas (L2), realized as negative freshwater perturbations of various shapes. The seasonalities of the periodic forcings (1-4 pulses per year) are shown in Figure 16. The integrated freshwater loss is the same for all perturbation shapes and corresponds to a triangular freshwater forcing of -0.5 Sv over 200 years (2100-2300).

was split into 200 parts of 50 years. The first two (unperturbed) parts p_k ($k = 1, 2$) were then subtracted from the other parts p_i ($i = 3...200$), to determine if the AMOC seasonality of these parts (during and after the perturbation) is different from the unperturbed seasonality. The differences were normalized by Each of the so gained differences $p_i - p_k$ was detrended by subtracting its trend component determined by the STL method (see Box).

One such example with a rectangular freshwater forcing (the first five years of $p_{20} - p_1$, corresponding to the years 2950-2955 versus 2000-2005) is shown in Figure 18, but all paired differences look very similar. The subtraction revealed that the seasonality is altered by the perturbation: Shortly after reaching its annual minimum in spring, the AMOC is slightly enhanced by the Agulhas perturbation. The enhancement amounts to 0.1 Sv to 0.4 Sv. Interestingly, this effect is not just recorded while the perturbation is active, but carries over to the new equilibrium (which has been reached by year 2950, as seen in Figure 17). While the mean value of the AMOC strength is rapidly restored after the perturbation ceases, the seasonality modification is still clearly visible after 10,000 years.

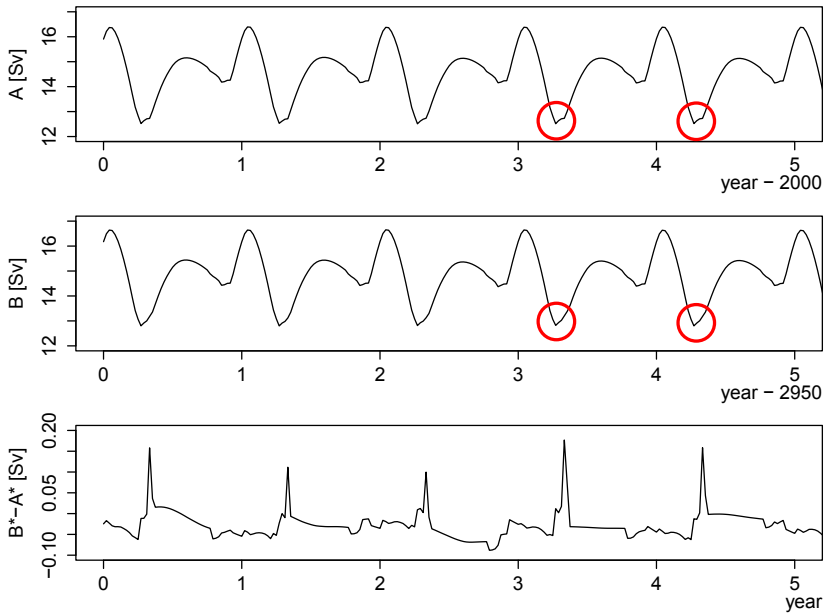

Figure 18: AMOC seasonality before (A) and after (B) a periodic negative freshwater forcing of one pulse of 1 Sv per year, which was applied at Cape Agulhas (L3) over 200 years; and their normalized difference B*-A*, where A*$= A - \bar{A}$ and B*$= B - \bar{B}$. The red circles highlight the main difference between A and B.

The non-rectangular forcings (the triangular forcing as well as 1, 2 or 4 periodic negative freshwater pulses per year) produce a very similar AMOC seasonality modification. As can be seen from the seasonality plots before and after the perturbation in Figure 18, the modification is not a temporal enhancement of an already strong AMOC phase, but causes a slightly faster recovery from the annual minimum state. This faster recovery corresponds to the sharp peaks seen in the difference plot and occurs for any of the five tested perturbation shapes. This leads to the conclusion that the AMOC seasonality modification is not caused by the Agulhas leakage seasonality, but by the overall salinity increase; which is consitent with the fact that the modified seasonality remains unchanged for thousands of years after the perturbation.

Figures 19e-f show the seasonal differences in shuffling convection depth between the new equilibrium after a negative rectangular freshwater perturbation and the unperturbed state. Figure 19f reveals that the shuffling convection is enhanced in a grid cell south of Greenland in spring (MAM), which enhances NADW formation.

It has to be remembered that the simple Agulhas leakage parameterization employed in these experiments only influences the AMOC via buoyancy forcing. If the dynamical interaction of leakage and AMOC was taken into account, it may well be that the leakage seasonality has an impact on AMOC seasonality. Therefore, the Bern3D model is not ideal to simulate the temporal response of the AMOC to Agulhas leakage. Unless a leakage parameterization could be found that also accounts for the impact of dynamics, a model that resolves the dynamical processes should be employed for such experiments.

3.1.4. Dipole compenstation: an Agulhas leakage parameterization

Thus far, only temporally limited freshwater perturbations were introduced at Cape Agulhas. However, the real Agulhas leakage phenomenon is a ceaseless flow of saline water. For multi-millennium simulations with the model, the salt influx has to be compensated such that the total salt content of the ocean remains constant and an equilibrium can be reached. As mentioned in the previous section, distributing the compensating freshwater flux on the remaining unperturbed boxes is not a good solution, because this causes unwanted effects. Therefore, a new compensation approach was tested: The freshwater that was taken from a single box at Cape Agulhas was added to a single box elsewhere. This is called “dipole compensation”.

The location of the Agulhas dipole grid boxes was chosen in such a way that the impact on the Atlantic Ocean salinity was maximized. Water masses starting from the salt inlet location should be entirely distributed into the Atlantic, while waters from the compensation location should stay away from this basin as long as possible. For the salt inlet location, the first grid box west of South Africa’s southernmost tip was chosen (hereafter denoted L4; see Figure 12). The flux into the Atlantic from this position is even more direct than from the previously used locations L2 and L3. Many different boxes were tested for the compensa-

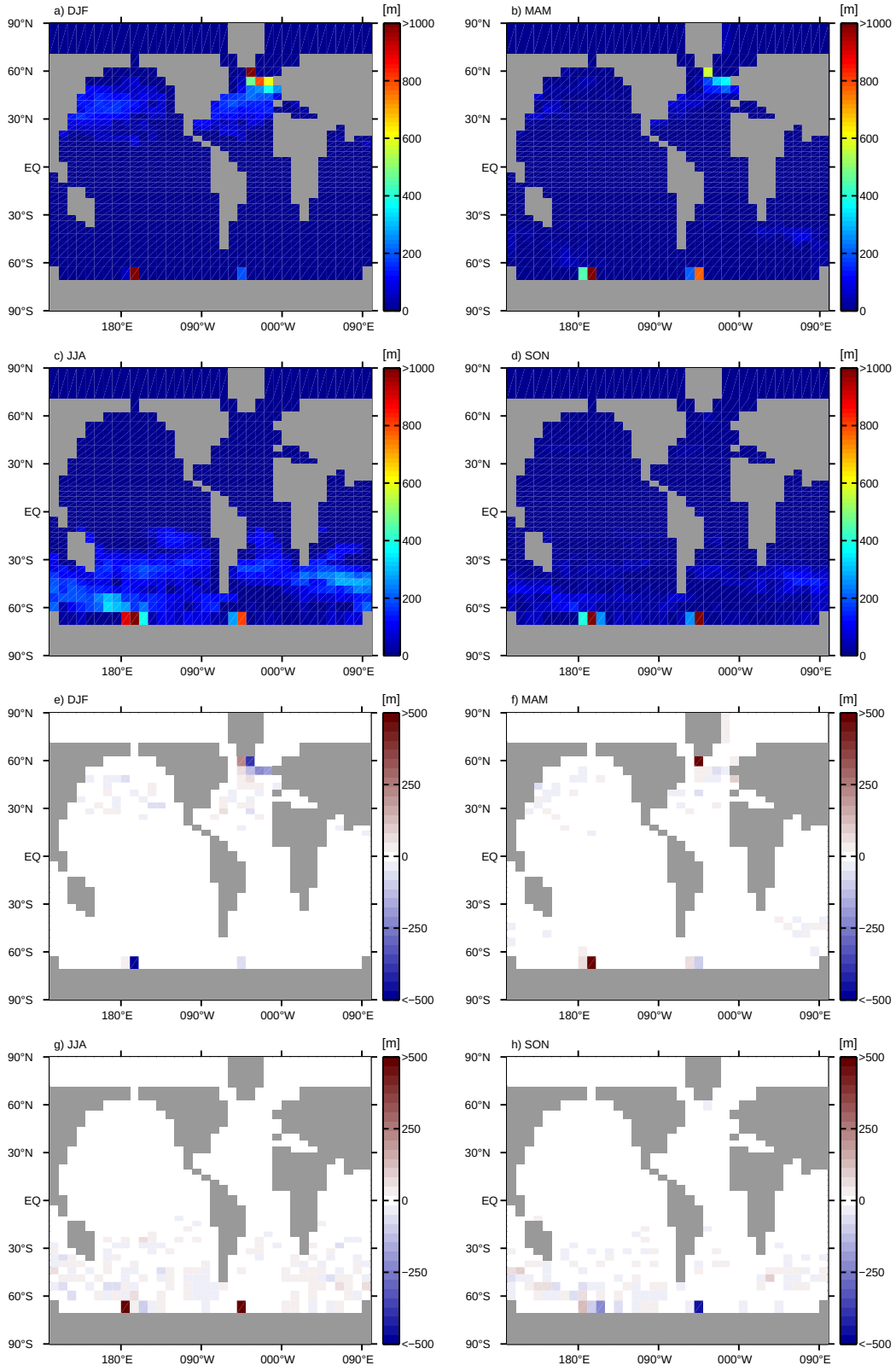

Figure 19: Seasonally averaged convective depths of the shuffling convection in an unperturbed state (a-d); and differences to this unperturbed state after a negative freshwater perturbation of 0.25 Sv during 200 years (e-h). The freshwater perturbation flux out of the ocean is prescribed near the southernmost tip of Africa (location 2, compare Figure 12).

tion location, most of them situated in the Indian Ocean, where the saline waters forming Agulhas leakage come from. All tested locations are shaded in light blue in Figure 12. For each of them, a dye tracer experiment was performed. One dye tracer ($Dye1$) was inserted at the test location, and a second one ($Dye2$) was injected at L4 at the same time. After 1000 simulation years, the concentration of $Dye1$ was subtracted from the concentration of $Dye2$. The location with the largest result $Dye2 - Dye1$ in the Atlantic Ocean surface was chosen to be the freshwater compensation location for the following dipole experiments. It is situated in the North Indian Ocean at the coast and hereafter denoted L5, see also Figure 12. Although freshwater and salinity behave differently from the passive dye tracers, this location choice ensures a minimal interference of the compensating freshwater influx with the Agulhas salt influx.

Test compensation locations also included boxes in the Southern Ocean below Africa. Part of the dye tracers injected into these boxes were distributed in the Indian Ocean due to Agulhas Retroflection, but a large fraction was also transported eastward swiftly around the ACC and thereafter into the Atlantic. Therefore, these locations are not suitable for the dipole experiments. Other test locations in the South or East of the Indian Ocean (in the Agulhas Gyre) caused a similar dye tracer distribution as L5. They were rejected in favor of L5 after some preliminary freshwater experiments, because they caused an even stronger freshening of the Indian Ocean surface waters (compare Figure 20).

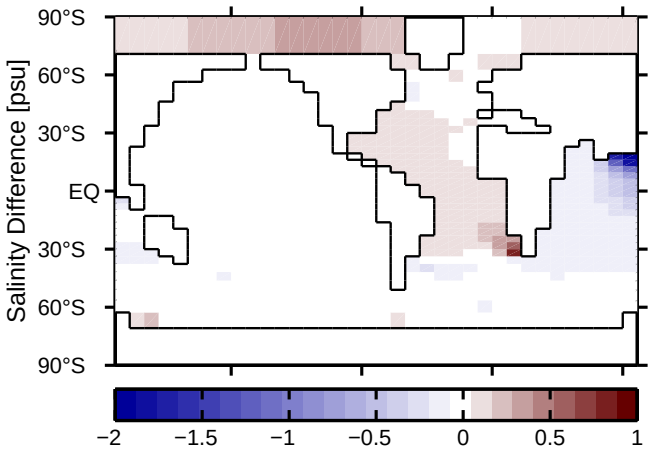

Figure 20: Sea Surface Salinity difference between the new equilibrium with a dipole-compensated Agulhas leakage flux corresponding to 2 Sv (weakest), and the standard modern Bern3D equilibrium. The salt inlet (L4) and compensating freswater inlet (L5) are recognized as the locations with maximum and minimum salinity difference, respectively. Compare Figure 12.

With the dipole locations L4 and L5 described above, quantitative experiments were made. According to Beal et al., 2011, Agulhas leakage amounts to a flow of 2 - 15 Sv into the Atlantic. This corresponds roughly to a pure freshwater loss of 0.058 - 0.430 Sv (converted using an average salinity of $S_0 = 34.78$ psu). Five experiments were conducted to simulate this range. The dipole freshwater flux was activated for a period of 10,000 years, in rectangular shape to obtain a constant flux over the whole duration. After an initial slight overshooting

in AMOC strength, new equilibria were established after roughly 1000 -3000 years (depending on perturbation strength), with a AMOC maximum of 14.9 -16.1 Sv (unperturbed: 14.5 Sv). This confirms that the AMOC can be strengthened by 3 % to 11 % by a simple Agulhas leakage parameterization in the Bern3D model.

This finding leads to the question if part of the Atlantic-to-Pacific freshwater flux (APF, compare Section 2.4) in the Bern3D model could be substituted by Agulhas leakage. It was found that the AMOC weakening due to a weaker APF can indeed be compensated by adding an Agulhas dipole, especially if only the southern part of the APF is weakened. This is shown in Figure 21 for two different strengths of the dipole. It can be seen that, e.g., with an Agulhas leakage of 5 Sv, the South APF can be weakened to 0.07 Sv to retain the current AMOC strength. Stronger leakages were not included because they cause a highly unrealistic SSS distribution (too fresh waters in a large zone around L5). However, if the South APF is removed completely, the AMOC is shut down even with a stronger dipole.

In conclusion, the Agulhas leakage can account for a major part of the South APF; but the dipole paramaterization used for the experiments described above is not suited to substitute part of the APF in the standard steady state of the model, because it freshens the Indian Ocean too much (even for small leakages, see Figure 20). Still, it represents the phenomenon much better than the standard all-box freshwater flux compensation.

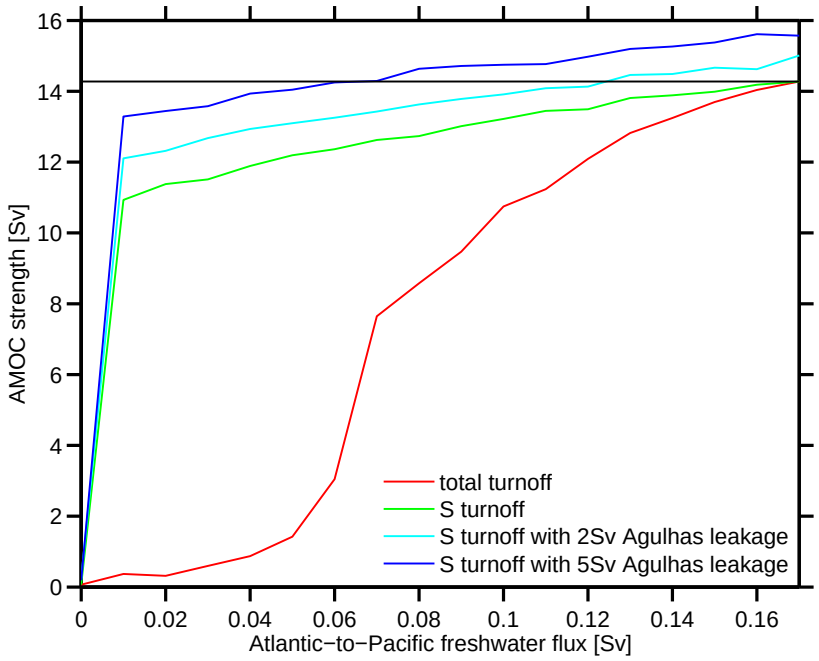

Figure 21: Equilibrium maximum AMOC strength as a function of Atlantic-to-Pacific freshwater flux (APF) strength, without Agulhas leakage (red and green lines) and with two different Agulhas leakage strengths (dipole compensated). The x-axis corresponds to the Northern and Southern part of the APF for the red line, and only to the Southern part for the other lines. The black line at 14.5 Sv corresponds to the AMOC maximum of the unperturbed model state with an APF of 0.7 Sv on both hemispheres.

3.1.5. AMOC Hysteresis

Climate models often show a non-linear, hysteresis-like response of the AMOC to freshwater perturbations (Stocker and Marchal, 2000; Rahmstorf et al., 2005; Hu et al., 2012). One of the main differences between the models is that their unperturbed state may be mono-stable (their initial equilibrium is reached after a freshwater perturbation vanishes) or bi-stable (a new equilibrium is reached). Under mixed boundary conditions (MBC), the Bern3D model was found to be in a bi-stable state (Ritz, 2007; Lehmann, 2011).
In most hysteresis experiments, the freshwater perturbations are introduced in the North Atlantic. For comparison purposes, such an experiment was performed using the coupled Bern3D model. Freshwater was let into the Atlantic uniformly between 50°N and 70°N. Following Rahmstorf et al., 2005, the rate of change of freshwater input was chosen to be 0.05 Sv per 1000 years, which is slow enough that the system can sufficiently equilibrate at all times. A 8000 year triangular shaped freshwater forcing of +0.2 Sv was directly followed by a negative forcing of the same dimensions. Perturbations with no compensation were tested as well as perturbations with compensation in all grid boxes. The resulting hysteresis curves are given in Figure 22. It can be seen that the coupled model is bi-stable in the uncompensated case, but mono-stable with the all-box compensation.[2]

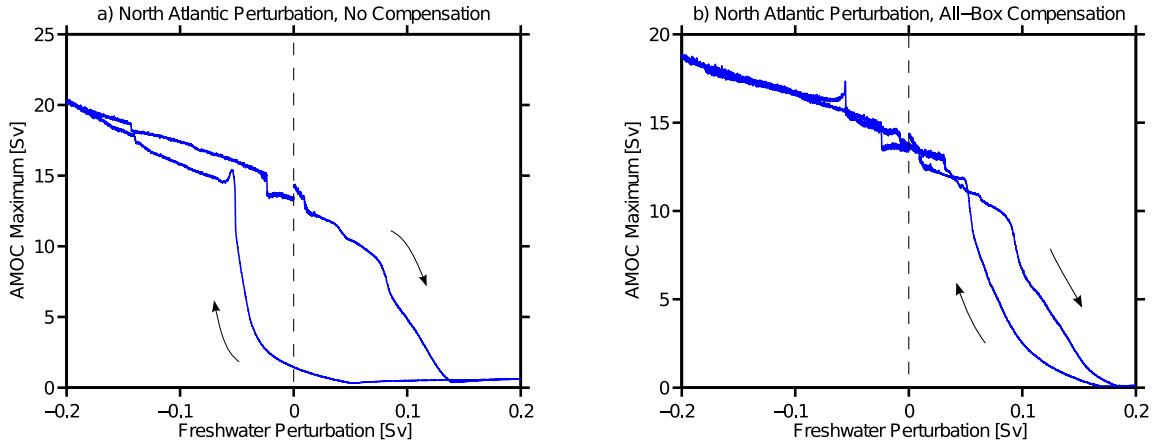

Figure 22: AMOC hysteresis due to a freshwater forcing of 0.2 to −0.2 Sv, applied in the North Atlantic between 50°N and 70°N. The forcing is a) uncompensated and b) compensated in all grid boxes.

Can freshwater perturbations in the Agulhas region also cause an AMOC hysteresis? This question was investigated using the coupled Bern3D model with three different freshwater compensation approaches: a) no compensation, b) compensation in all grid boxes and c) dipole compensation (compare section 3.1.4). While the temporal evolution of the freshwater fluxes was the same as in the North Atlantic experiments, the maximum amplitude was increased to 0.5 Sv, because Agulhas perturbations have a weaker (less direct) impact on the AMOC. The results are shown in Figure 23.

There are several differences between these Agulhas-forced AMOC modifications and the

[2] Here, 'mono-stable' and 'bi-stable' are used as defined in Rahmstorf et al., 2005: If two different states exist when the perturbation vanishes (i.e., at the 0 Sv line), the system is bi-stable; else it is mono-stable, even if a hysteresis-like behavior is observed for non-zero perturbations.

"classical" AMOC hysteresis behavior (e.g., in Figure 22). Firstly, it can be seen that the AMOC off-state is not fully reached in any of the three cases, in spite of the larger amplitude of the freshwater perturbation. Secondly, in all cases the negative freshwater perturbation causes the AMOC not to increase, but to decrease again. This was already noticed in earlier experiments with negative freshwater pulses, if the pulses were strong or long enough - the integrated amount of freshwater loss is the key parameter. The reason for the AMOC weakening is probably that the enhanced sinking of water masses does not occur in the NADW formation region, but further South, if enough salt is let in at Cape Agulhas. This could cause flows that counteract the AMOC. The effect is strongest in the uncompensated case, where the AMOC only partly recovers after the positive freshwater perturbation and reaches its minimum during the negative perturbation. This causes an obvious bi-stability. In the all-box compensation experiment, the AMOC shows only a very minimal hysteresis behavior because the compensation effect overrules the Agulhas leakage effect. Herein, the AMOC weakening during the negative perturbation is probably not due to Southern convection, but due to the compensation effect. Dipole compensation produces the most "classical" monostable hysteresis behavior, strengthening the assumption that this is the most suitable of the three approaches to simulate Agulhas in the Bern3d model. The sudden shifts in AMOC may be caused by non-equilibrium effects due to the higher rate of change of freshwater input.

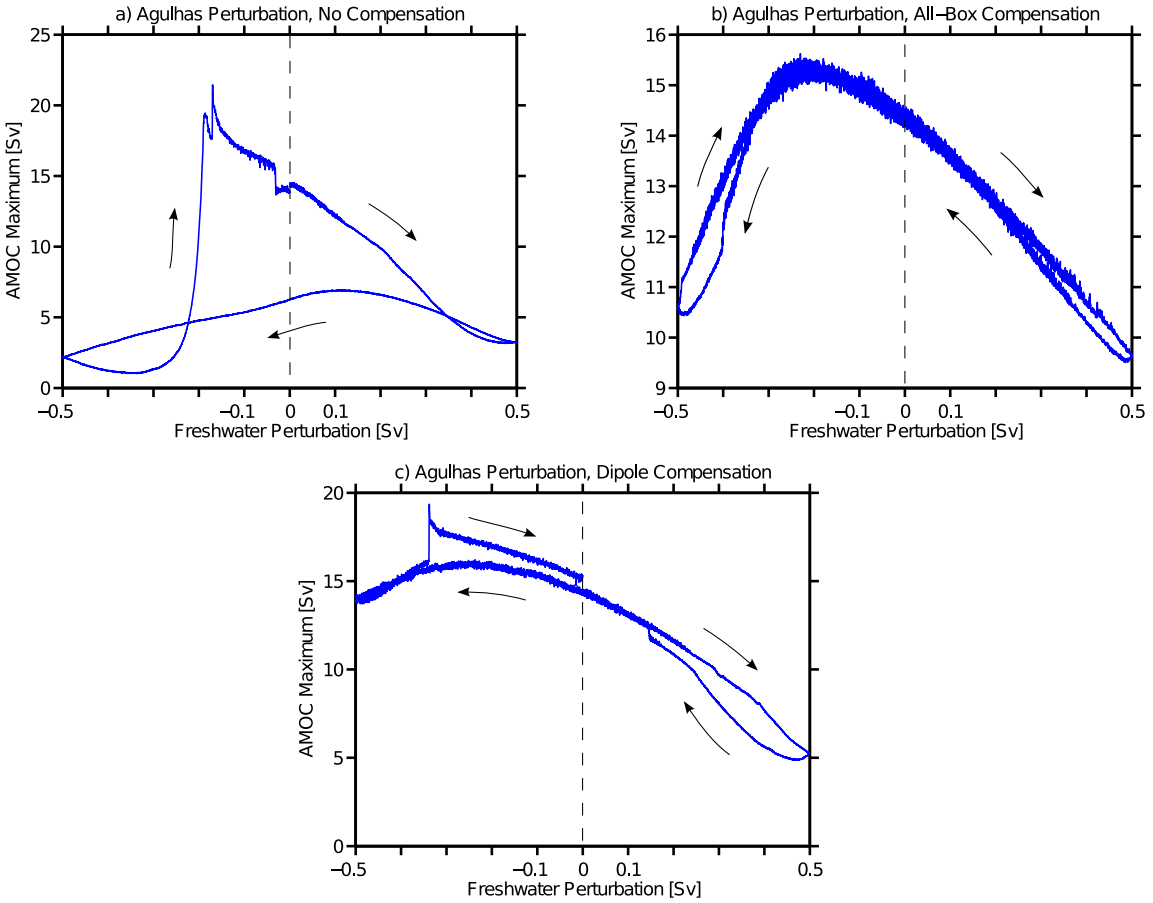

Figure 23: AMOC hysteresis due to a freshwater forcing of 0.5 to −0.5 Sv, applied at Cape Agulhas (at location L4, see Figure 12). The forcing is a) uncompensated, b) compensated in all grid boxes and c) dipole-compensated.

3.2. Modern world tectonic rearrangements

As detailed in the Methods Section 2.6, three mayor ocean gateways were modified in the modern-world map: Drake Passage, Panama strait, and strait of Suez. The results for Drake and Panama modifications are divided into two sections: Combinations of open and closed states of the two gateways are described in Section 3.2.1, and effects of gradual openings are discussed in Section 3.2.2. The minor effects of the strait of Suez opening are discussed separately in the last paragraph of this section. Abbreviations used for topographies are listed in Table 1.

3.2.1. Topographies with closed Drake Passage and open Panama Strait

Figures 24 to 26 show physical model properties, namely the depth-integrated and meridional ocean circulation, SST, SSS and atmospheric temperature, for four different topographies: standard modern (CTRL), closed Drake Passage (DRC5), open Panama strait (PAN2), and closed Drake Passage with open Panama Strait (PD5). These are also listed in Table 1. Separate model spinups were made for each topography, the figures show the situation after spinup 5 (compare Section 2.3). The most notable changes in ocean climate in response to these tectonic rearrangements are listed below.

Ocean circulation

Figure 24a is identical to Figure 2 that was described earlier. Figure 24b shows that closing Drake Passage strengthens ocean gyres in the southern hemisphere, namely the South Pacific Gyre and the Indian Ocean Gyre. The wind-driven current around Antarctica, which would form the ACC if Drake Passage was open, is reflected back into the Pacific by the closed passage. It feeds into the South Pacific Gyre, and thereafter partly into the Indian Ocean Gyre via a strengthened Indonesian throughflow, which couples the two gyres. Although the South Atlantic Gyre is also coupled to the Indian Ocean Gyre via Agulhas leakage, it is not notably strenghtened. The stronger Agulhas Current along Southeast Africa is also more strongly deflected, such that the flow increase is not transmitted into the Atlantic. Furthermore, clockwise subpolar gyres are formed east and west of Drake Passage, probably due to a combination of wind forcing and large-scale turbulence caused by the reflection of the above mentioned gyre currents on the closed passage.

Figures 24c and 24d show the effects of an open Panama Strait on the barotropic circulation. Panama throughflow increases from 7 Sv to 22 Sv when Drake Passage is closed, because of the deflected Antarctic current described in the above paragraph. Therefore, the other circulation changes due to an open Panama Strait are also stronger with a closed Drake Passage. The easternmost part of the South Pacific Gyre is redirected northward, forming the Panama throughflow. Therefore, the zonal extent of the gyre is decreased. It is also weakened, as is the Indian Ocean Current which is coupled to it. However, the large-scale northward flow in the South Pacific is not significantly affected: Although the values of the Barotropic stream

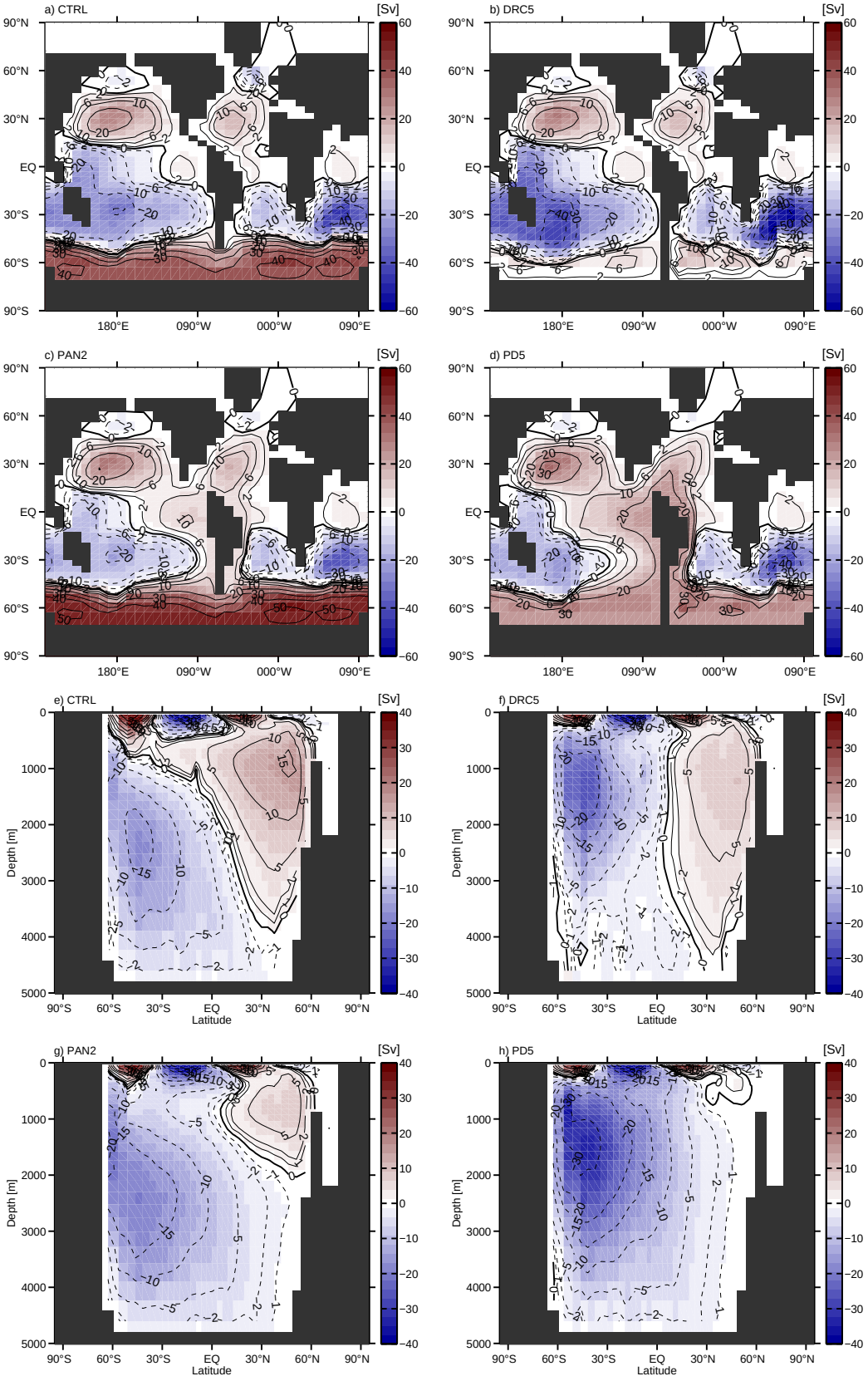

Figure 24: Barotropic stream function (a-d) and Global MOC (e-h) in CTRL (control run), DRC5 (closed Drake Passage) PAN2 (open Panama strait) and PD5 (combination of DRC5 and PAN2). Compare Table 1.

function are shifted, its gradient shape and remain roughly the same in this region. Similarly, although the stream function value around Antarctica is around 10 Sv higher in Figure 24c than in Figure 24a, the Drake throughflow has only increased by less than 1 Sv. This has to be kept in mind when comparing circulation plots: not the *magnitude* of the stream function, but its *gradient* dictates how strong the circulation is.

The Panama throughflow also weakens the North Atlantic Subpolar Gyre and incorporates the Subtropical Gyre into a southward flowing western boundary current (WBC). With a closed Drake Passage, these two effects are so strong that both gyres almost entirely vanish. The South Atlantic Gyre remains stable even in presence of the strong WBC caused by the Panama throughflow. The small gyres around the closed passage are present also when the Panama Strait is open, they are just less well visible in Figure 24d due to the choice of stream line intervals.

Figures 24e-h show the global MOC in the four different bathymetries. Most important for our studies is the AMOC, but with an open Panama Strait plotting the AMOC separately is not very informative because there is a discontinuity due to the Panama throughflow. However, the AMOC is very well visible in the northern part of the global MOC because the North Pacific MOC is very weak (compare, e.g., Ritz et al., 2011). The control run (Figure 24e) features a stable AMOC of about 16 Sv and a Southern Ocean overturning cell which is about equally strong.

With a closed Drake Passage (Figure 24f), the AMOC gets weaker (max. 9 Sv), but deeper: NADW propagates all the way down to the seafloor. More importantly however, the NADW is not transported to Antarctica as in the control state, but upwelled in the Northern hemisphere. The Northern Hemispheric AMOC cell is disconnected from the global circulation. This weakening and disconnection can be qualitatively explained with the simplified picture of the ocean conveyor belt. The ACC is a major driver of the global thermohaline circulation, directly feeding into the AMOC after flowing through Drake Passage. In its absence, the AMOC is therefore slowed down. Also in more comprehensive considerations, it was shown that the ACC and AMOC are dynamically linked. Toggweiler and Samuels (1995) found a direct relation between wind stress forcing in the Drake Passage region and AMOC strength in their model simulations. Stronger wind stress forcing causes stronger Ekman divergence in the Southern Ocean, resulting in stronger upwelling of NADW. While the wind stress was not modified in our simulations, the closed Drake Passage inhibits not only the ACC but also surface flows parallel to Antarctica in this region, such that Ekman divergence can only occur farther east. As seen in the simulation, there is no NADW upwelling in the Southern Ocean under these unfavorable circumstances. There may also be other factors contributing to the significant change in the AMOC's behavior, as the ocean circulation is a very complex system. As an example, the stronger Southern Ocean meridional overturning circulation (SOMOC) may also counteract the southward propagation of NADW, especially because the maximum of the cell is also shifted to shallower depths.

Figures 24g and 24h show that opening Panama Strait weakens the AMOC even more significantly. The main reason for this is probably the Panama throughflow. It causes a dynamical perturbation of the NADW formation region and transports fresher waters from the Pacific into the North Atlantic (see also Figures 25g and 25h). With an open Drake Passage, a shallow and weak AMOC cell remains; with a closed passage, the AMOC is completely shut down, which corroborates with the above hypothesis because the Panama throughflow is much stronger in this topography.

In summary, by opening Panama Strait and closing Drake Passage, we find a completely different flow regime compared to the standard modern setting. This underlines the importance of these two gateways for the global ocean climate state. The changes they cause in SST, SSS and atmospheric temperature are briefly discussed below.

Sea surface temperature, salinity and atmospheric temperature

Figures 25 and 26 show the SST, SSS and atmospheric temperature distributions in the control run and differences in the simulation with modified gateways. The control simulation distributions are in reasonable agreement with observations, as described in Ritz et al. (2011). In the modified topographies, the most obvious difference is a North-South dipole in the Atlantic SST distribution. This cooling in the North Atlantic and warming in the South is mainly caused by the collapsing AMOC (compare Figures 24f-h), and has also been found in previous studies (Stocker, 2002). However, in the case of a closed Drake Passage the southern warming is enhanced by a secondary effect: an east-west temperature dipole around Drake Passage. The cooling in the west may be caused by cold waters originating in the western part of the Pacific sector of the Southern Ocean, which stagnate before the closed passage or are distributed in this region by the Pacific Southern Ocean subpolar gyre mentioned earlier in this section. The additional warming east of Drake Passage can be similarly explained by the barotropic circulation (Figures 24b and 24d): Because the Indian Ocean gyre goes down to higher latitudes when Drake Passage is closed, warm waters from the Indian Ocean reach the Atlantic sector of the Southern Ocean, where they are further distributed by the subpolar gyres east of the passage.
The atmospheric temperature differences shown in Figure 26 are in line with the above described SST differences, due to air-sea heat exchange.

The most prominent SSS difference arising from a closing of Drake Passage is a widespread freshening in the Pacific, which is stronger in the South. The fact that the South Atlantic gets saltier at the same time raises the hypothesis that this change is caused by a larger impact of the APF in the southern region, because the compensating effect of the ACC is missing. On the other hand, a Panama Strait opening mainly causes a freshening of the North Atlantic and Arctic Ocean. The reason for this is the inflow of fresher water masses through the strait. The SSS is slighty increased in the South, which is probably because the WBC originating from Panama throughflow transports salty North Atlantic waters southwards.
The Arctic Ocean gets saltier when the Drake Passage is closed, and fresher when the Panama

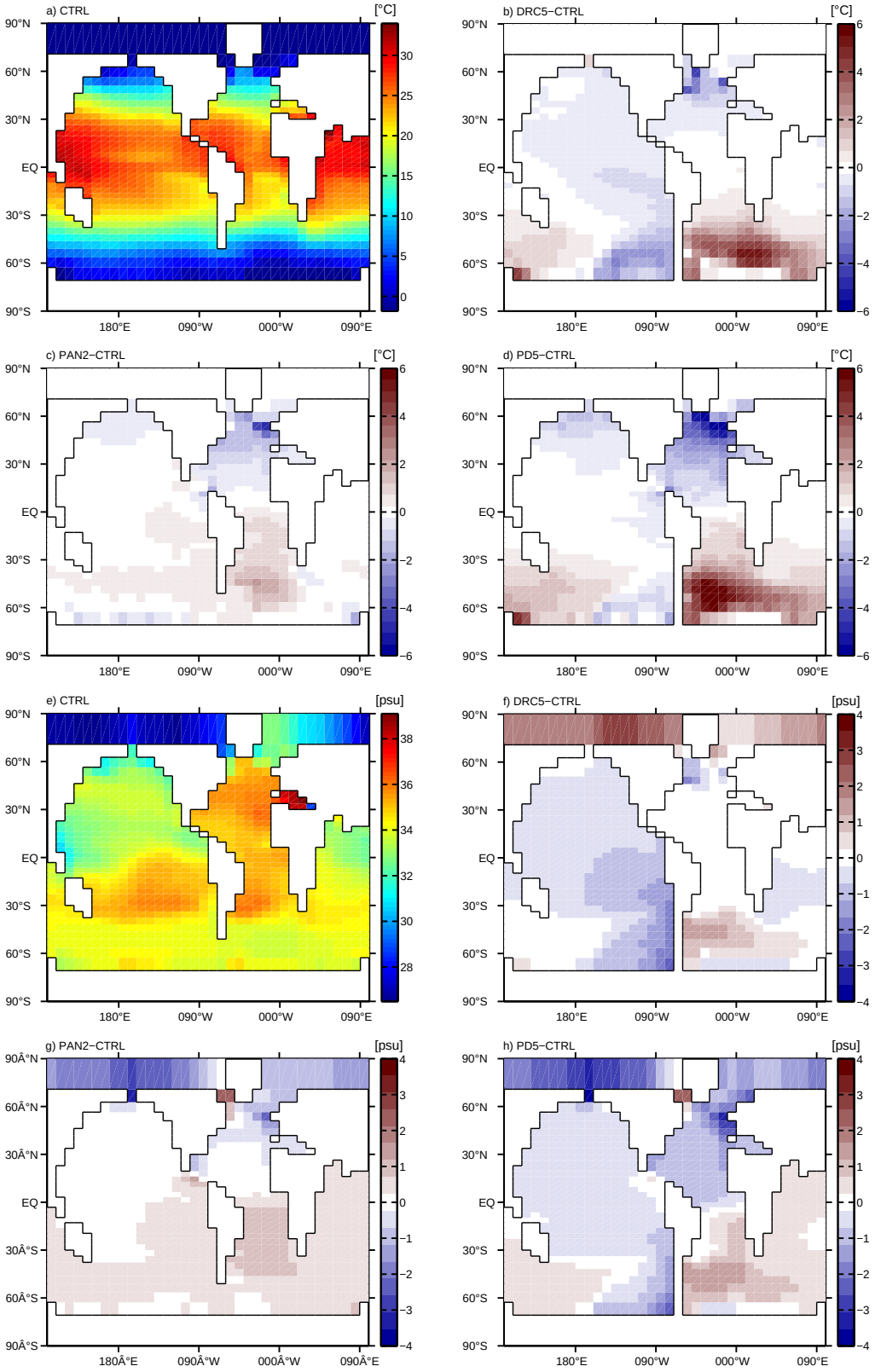

Figure 25: SST (a-d) and SSS (e-h) distributions in CTRL (control run), and differences DRC5-CTRL (closed Drake Passage), PAN2-CTRL (open Panama strait) and PD5-CTRL (combination of DRC5 and PAN2). Compare Table 1.

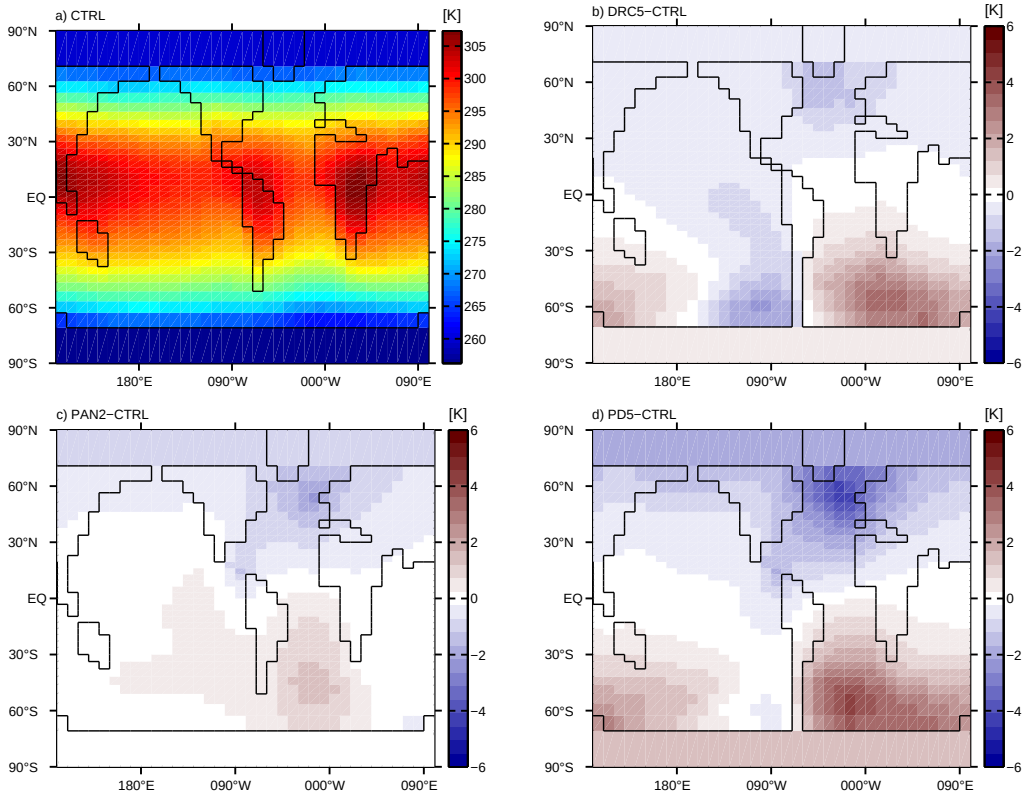

Figure 26: Atmospheric temperature distribution in CTRL (control run, a), and atmospheric temperature differences DRC5-CTRL (closed Drake Passage, b) PAN2-CTRL (open Panama strait, c) and PD5-CTRL (combination of DRC5 and PAN2, d). Compare Table 1.

Strait is opened. In the combined case, the latter effect prevails. This is directly related to Bering Strait throughflow, which is strengthened by a closed Drake Passage and shut down if the Panama Strait is open. More details are given near the end of the next paragraph.

Neodymium isotopes

Let us now look at Neodymium isotopes in these four topographies. For the comparison with marine sediment cores, the seafloor values are most interesting. Figure 27 shows ϵ_{Nd} and $[\mathrm{Nd}]_d$ distributions at the seafloor in the control run, and differences in the three modified topographies. The Nd distributions in the control run are also in reasonable agreement with observations, as discussed in Rempfer et al. (2011). Closing Drake Passage has no obvious effect on the ϵ_{Nd} seafloor distribution, except a widespread shift towards slightly more positive values. Especially in the region of our foremost interest, the Atlantic Southern Ocean where the ODP sites 689 and 1090 are located (compare Figure 10), the signal is quite complex and ambiguous. A clearer signature emerges from the Panama Strait opening: The seafloor ϵ_{Nd} values are also slightly increased in many regions, but especially in the North Atlantic due to inflow of Pacific waters (with higher ϵ_{Nd} values) through the Panama Strait. The positive signal is weaker, but still unambiguous in the Atlantic Southern Ocean, to where it is most probably transported by the WBC originating from Panama throughflow. Interestingly, this effect increases with a closed Drake Passage in the North Atlantic (due to stronger Panama

throughflow), but not in the Atlantic Southern Ocean (although the WBC is also stronger); compare Figures 27c-d and 24c-d, correspondingly. The Arctic Ocean ϵ_{Nd} is reduced in both topographies with an open Panama Strait, which is probably related to the freshening in this region, as ϵ_{Nd} covaries with salinity.

Figures 27f-h show the differences in seafloor $[Nd]_d$ caused by the tectonic rearrangements. As described in Rempfer et al. (2011), seafloor $[Nd]_d$ increases with increasing age of the water mass. Closing Drake Passage causes a concentration increase in the Atlantic Southern Ocean and North Atlantic. The Atlantic Southern Ocean increase is probably caused by a stagnation of wind-driven water masses before the passage. The reason for the North Atlantic increase is the weakened AMOC: slower overturning increases the North Atlantic turnover time, which in turn increases the water mass age. Similarly, seafloor $[Nd]_d$ is probably decreased due to faster ventilation by the stronger Indian Ocean gyre.

Opening Panama Strait has an additional dipole-type effect on the concentration. The Panama throughflow transports Nd from the Pacific into the North Atlantic and Arctic Ocean, increasing $[Nd]_d$ in the latter regions and decreasing it in the Pacific. This effect is much stronger if Drake Passage is closed, and the North Atlantic increase is further enhanced by the weakened AMOC as described earlier. With an open Drake Passage, an additional decrease in the Southern Ocean is visible. This can be explained by the stronger SOMOC which decreases the age of the water masses in the Southern Ocean.

Another interesting effect is recorded in the Arctic Ocean, where seafloor $[Nd]_d$ is decreased in DRC5 (except in a region west of Greenland which is connected to the North Atlantic via Polar Gyre), and increased in PAN2 and PD5. This may be explained by the changes in Bering Strait throughflow. In CTRL, 0.36 Sv are transported into the Arctic Ocean from the North Pacific through Bering Strait. It is noteworthy that the exact same amount is transported from the Arctic Ocean into the North Atlantic through Davis strait in the standard setting of the Bern3D model. The reason for this symmetry is that Greenland is not defined as a separate island with respect to ocean circulation (i.e., in the .psiles and .paths files, compare Appendix A). Therefore, it technically belongs to the mainland Eurasia, such that there is no net flow between Greenland and Europe, and the flow between Greenland and North America (Davis Strait) is identical to the flow between Asia and North America (Bering Strait). Now, the Drake Passage opening increases Bering Strait throughflow to 0.92 Sv, decreasing the Arctic water mass age and thus $[Nd]_d$. On the other hand, the throughflow becomes negligibly small (<0.05 Sv) when the Panama Strait is opened (even with an open Drake Passage), increasing Arctic $[Nd]_d$ in most regions.

Strait of Suez opening

Only one of the six tested Suez configurations listed in Table 1 leads to a significant flow through the Strait of Suez, namely SUE6. This bathymetry features the widest and deepest Strait of Suez opening towards the Indian Ocean, but no additional opening on the Atlantic

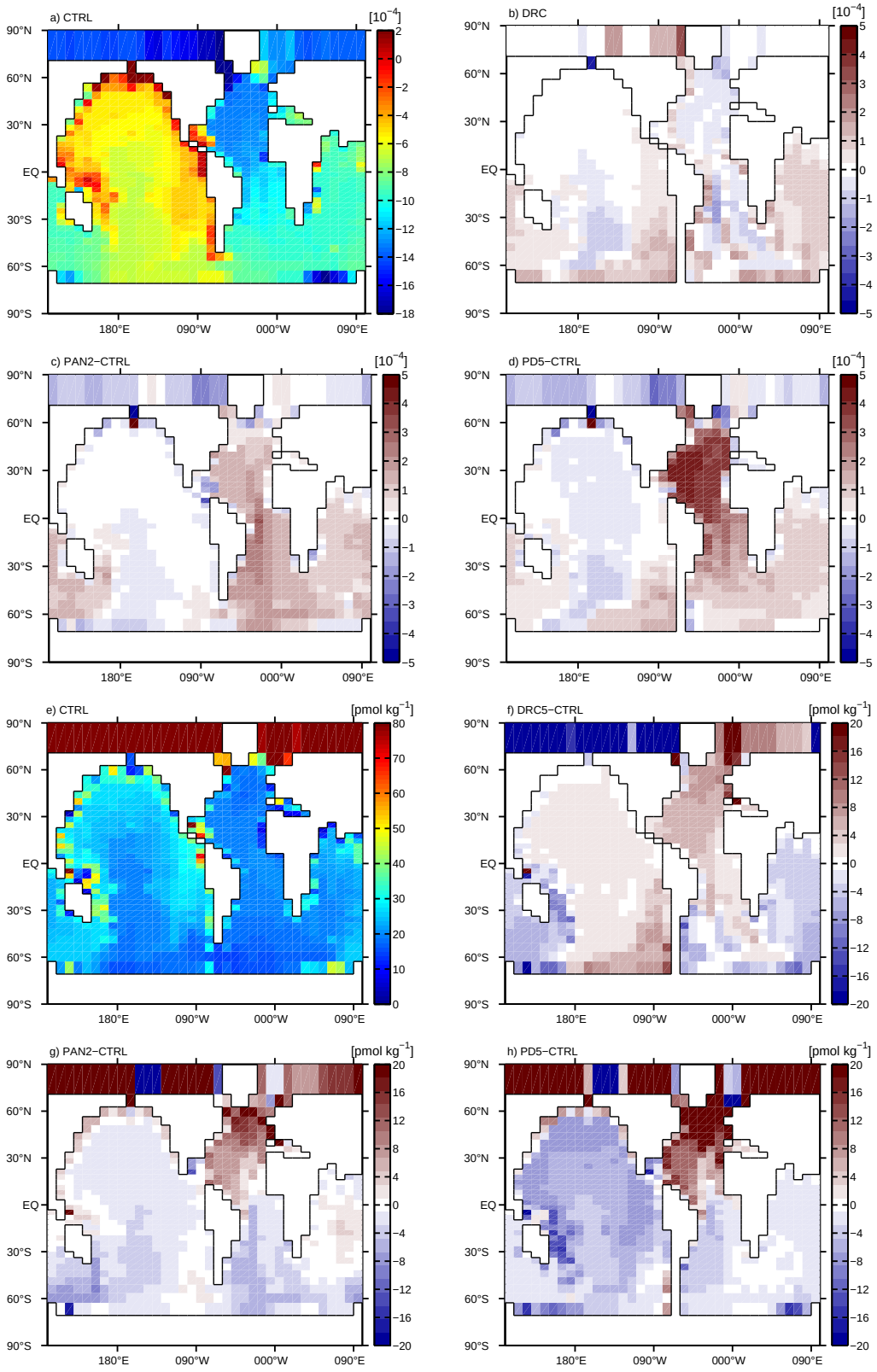

Figure 27: Seafloor ϵ_{Nd} (a-d) and $[Nd]_d$ (e-h) distributions in CTRL (control run), and differences DRC5-CTRL (closed Drake Passage), PAN2-CTRL (open Panama strait) and PD5-CTRL (combination of DRC5 and PAN2). Compare Table 1.

side. Interestingly, if the Atlantic side is widened as well (SUE5), there is no throughflow anymore. Possibly, the weak east-to-west flow seen in SUE6 is suppressed by a west-to-east flow which could arise due to the widening. Experiments with an open Panama Strait and a shallow or closed Drake Passage were repeated with an open Strait of Suez as in SUE6. However, because the Suez throughflow is so weak (1.7 Sv), the global circulation is barely modified. Figure 28 shows the circulation in the SPD1 bathymetry, with a shallow Drake Passage as in DRA4.

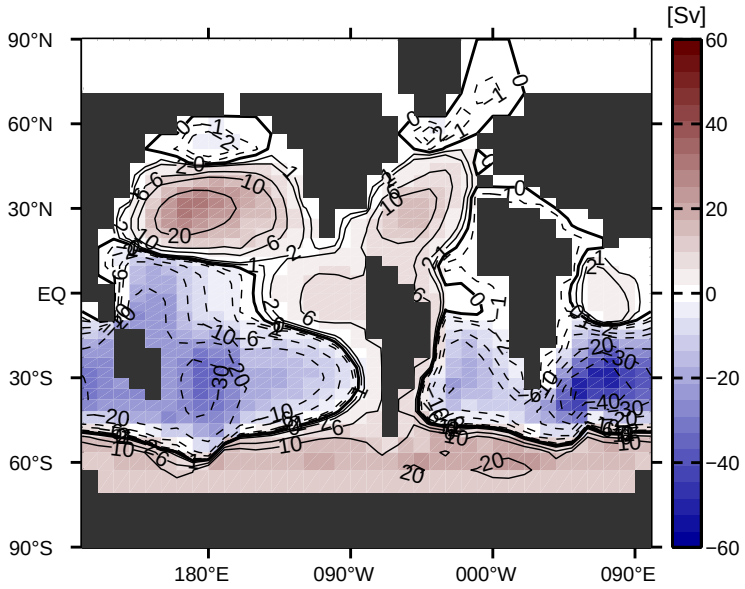

Figure 28: Depth-integrated ocean circulation in SPD1, a bathymetry with an open Panama Strait, open Strait of Suez and shallow Drake Passage (compare Table 1). Colors and contours show the Barotropic stream function in Sverdrup (Sv).

A stronger throughflow in the Suez region is only found if the Strait of Suez (or Tethys Seaway, correspondingly) is opened wider and to greater depths, as seen in, e.g., EO72 (Figure 35e). However, it is not sensible to do so in the modern map, because it would require to either shrink Africa to an unrealistic size, or modify its position, which would be quite time-consuming. Also, no Nd experiments were made with an open Strait of Suez, because the boundary source is not defined in this region.

3.2.2. Effects of opening Drake Passage and Panama Strait

In this section, the effects of opening Drake Passage and Panama Strait on throughflows and Neodymium isotopes are studied. As described in detail in Section 2.6, the two Panama Strait grid cells were opened uniformly, and the three Drake Passage cells were opened both uniformly and proportional to the modern-world bathymetry (with a deeper middle cell). Panama Strait opening started from CTRL, Drake Passage opening from both DRC5 (closed Panama Strait) and PD5 (open Panama Strait). Hence, four different Drake Passage opening scenarios are investigated in total. For two of them (the proportional openings from DRC5 and PD5), and for the Panama Strait opening, a pseudo-tranient method (compare also

section 2.6) was tested. The differences in results from this method versus separate spinups for each topography are discussed in the last paragraph of this section.

Uniform Panama Strait opening

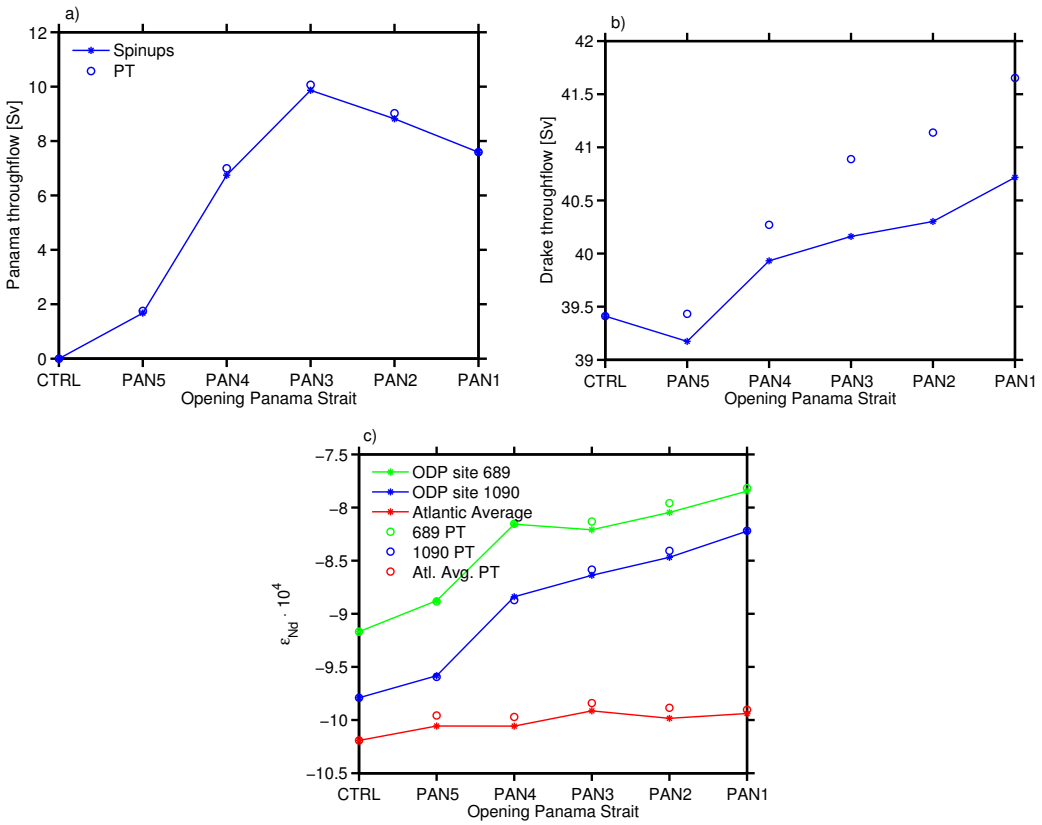

Figure 29: Panama- (a) and Drake throughflow (b) caused by an opening of Panama Strait from its modern closed state. The response of Neodymium isotopes at ODP sites 689 and 1090 and in the Atlantic average is shown in c). Labels on the x-axis correspond to the bathymetries listed in Table 1. Connected asterisks show results from separate spinups, circles show results from pseudo-transient (PT) simulations.

Figure 29 shows the Drake throughflow, Panama throughflow and ϵ_{Nd} evolution in response to a Panama Strait opening in five steps (PAN5 to PAN1 in Table 1). Connected asterisks show the values from separate spinups, circles show the values from pseudo-transient simulations for the same bathymetries. Interestingly, the Panama throughflow increases only in the first three steps (up to PAN3, with a Panama Strait depth of 729 m), and slightly decreases in the last two steps (which increase the depth to 2100 m). The maximum Panama throughflow of roughly 10 Sv in the modern-world bathymetry is hence reached with a relatively shallow strait. This is especially surprising because the friction around the Panama Strait is lower in the last two runs, because the strait is deeper than k_λ (compare Section 2.2.1). One might hypothesize that the lower drag is actually the cause of the weaker flow, e.g., because of a dynamical reaction on the modified drag distribution. This was tested in an additional simulation with the lowest Panama Strait seafloor elevation which still increases the drag (17 layers). The Panama throughflow in this simulation amounts to 9.29 Sv, which lies between the throughflow strenghts in PAN3 (9.86 Sv) and PAN2 (8.82 Sv). This implies that the slight weakening is not caused by drag modifications, but actually by the altered bathymetry.

For topographies with an open Panama Strait and modified or closed Drake Passage, the depth of PAN2 was chosen for the Panama Strait (1287 m). One of the larger depths was chosen for its reduced drag and because the Eocene Panama Strait was also deep (compare, e.g., Figure 5); and PAN2 was chosen because it showed and average Panama throughflow between PAN1 and PAN3, as described above.

The Drake throughflow varies only little in response to Panama Strait modifications: it decreases very slightly after Panama Strait opening, and increases by around 2 Sv when the strait is deepened. This corresponds to only about 5 % of the throughflow's magnitude and is negligible compared to the throughflow changes caused by Drake Passage modifications, as described in the following paragraphs. On the other hand, the influence of Panama Strait opening on ϵ_{Nd} distribution is quite significant. The Atlantic average increases very slightly, but the seafloor values around ODP sites 689 and 1090 increase by about $1.5 \cdot 10^{-4}$. This is probably due to the Panama WBC described in Section 3.2.1, which transports more radiogenic Nd from the eastern Pacific boundary to these locations. However, the Atlantic Southern Ocean ϵ_{Nd} signature is not directly correlated to the Panama throughflow: Although the greatest increase in both quantities is found in the second opening step, ϵ_{Nd} increases further in the last two steps where the Panama throughflow slightly decreases.

Drake Passage opening approaching the modern bathymetry

The first bathymetric evolution of Drake Passage goes from a fully closed state DRC5 (or PD5, for the case with open PS) to the standard modern CTRL (PAN2), as seamlessly as possible within the limitations of the coarse resolution. This evolution was first simulated in five steps DRC1-5 (PD1-5), as listed in Table 1, and the steps CTRL-DRC2 (PAN2-PD2) were then refined into 11 substeps. Figures 30a-c show the Drake throughflow, Panama throughflow and AMOC maximum values for the large steps, Figures 30d-e for the substeps. Obviously, the Panama throughflow is only shown for simulations with an open Panama Strait, and the AMOC maximum only for simulations with a closed strait.

In the coarse evolution shown in Figure 30a, the increase in Drake throughflow with increasing Drake Passage depth looks quite linear. An open Panama Strait causes a slightly larger deviation from linearity, otherwise the evolution is very similar. In contrast, the "gradual" opening looks far from linear. The Drake throughflow is surprisingly strong when all three Drake Passage cells are opened just one layer deep: 13 Sv, corresponding to water mass velocities of up to $14\,\mathrm{cm\,s^{-1}}$. Such velocities are otherwise only found in the strongest surface currents of wind-driven gyres, located in the open ocean where the drag is much lower. Thereafter, it can be seen that the throughflow stays constant or actuall decreases as only the middle box is further deepened. Only in the two steps in which the two outer boxes are deepened, the throughflow increases again. We will not hypothesize why this is the case, because that would lead to argumentations on a one-gridbox level, which should be avoided. We just observe that a uniform Drake Passage depth is apparently favorable for a strong Drake throughflow, which is backed up by the experiments on uniform Drake Passage opening (later in this Section).

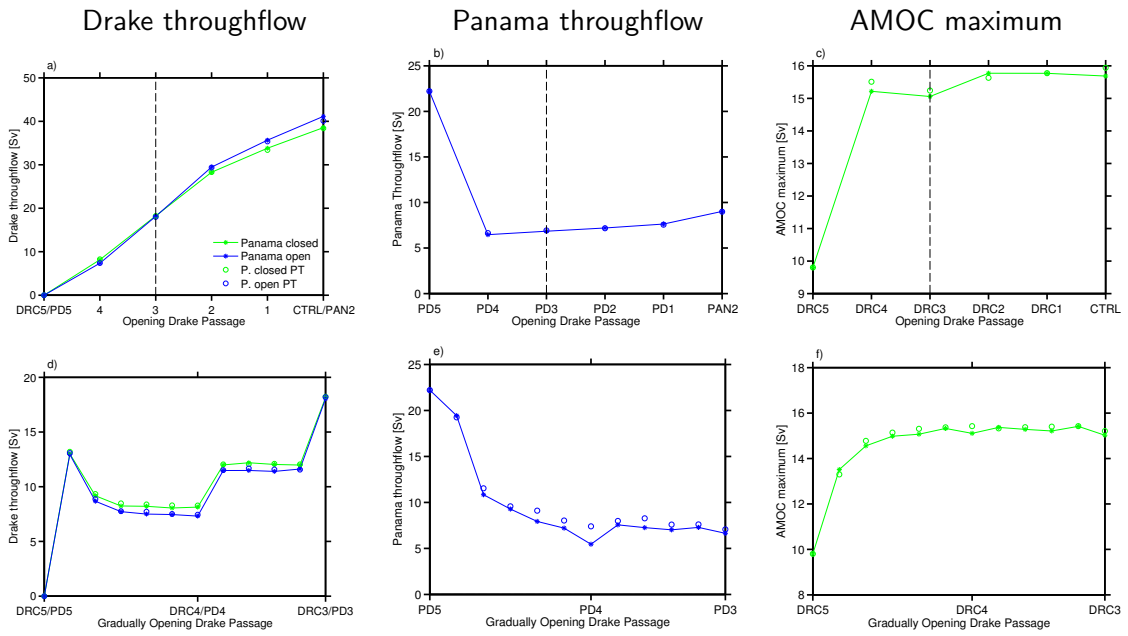

Figure 30: Opening Drake Passage from a closed state to its modern open state in equal steps (a-c), and substeps up to depth B (d-f). Panama throughflow (a/d), Drake throughflow (b/e) and AMOC maximum (c/f) are shown. Labels on the x-axis correspond to the bathymetries listed in Table 1; numbers 1-4 denote bathymetries DRC1-4/PD1-4. Panama Strait is closed in DRC1-5 and CTRL and open in PD1-5 and PAN2. Connected asterisks show results from separate spinups, circles show results from pseudo-transient (PT) simulations.

As can be seen in both Figure 30b and e, the Panama throughflow decreases quickly in response to Drake Passage opening, reaching its minimum of around 6 Sv in the PD4 bathymetry. This minimum Panama throughflow, along the associated shallow Drake Passage bathymetry, is similar to the Panama throughflow simulated by Heinemann (2009) in their Eocene bathymetry (compare Section 3.4). The AMOC maximum (Figures 30c and f) is only shown for simulations with a closed Panama Strait. When Drake Passage is opened, the AMOC recovers quickly from its weakened state. This suggests firstly that already a weak ACC is sufficient to maintain a strong interhemispheric AMOC, and secondly that the modern AMOC is in a stable equilibrium state which can only be disorganized by very strong perturbations (e.g., a fully closed Drake Passage).

Figure 31 shows the response of ϵ_{Nd} to the Drake Passage opening proportional to the modern-world bathymetry. The only clear signal is a slight drift towards more negative values in the Atlantic average when the passage is opened with an open Panama Strait, which is directly related to the weakening of the Panama throughflow. Other than that, the signals are quite diffuse and no clear trends are visible.

Uniform Drake Passage opening

The second bathymetric evolution of Drake Passage is very simple: Starting from the closed state DRC5 (or PD5, for the case with open Panama Strait), all three Drake Passage grid cells are deepend simultaneously in steps of one layer. By committing to this simplification, a Drake Passage bathymetry similar to the modern world is never reached, but we also don't

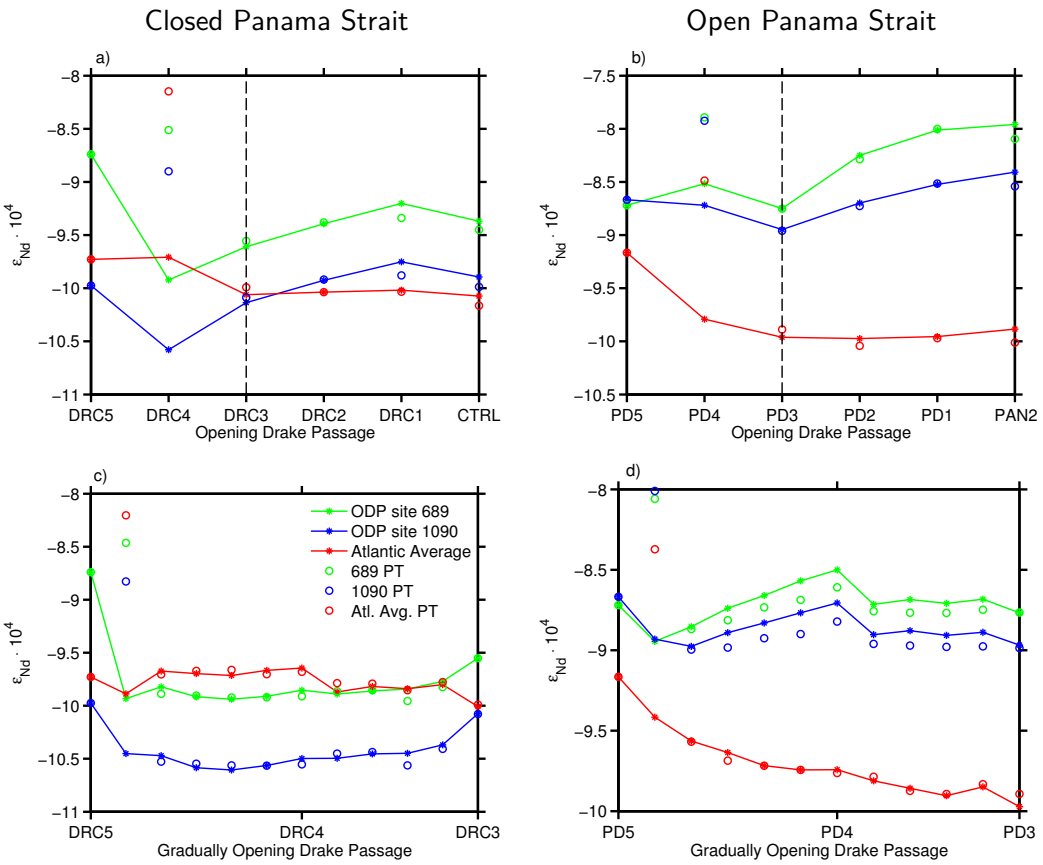

Figure 31: Opening Drake Passage from a closed state to its modern open state in equal steps (a-b), and substeps up to depth B (c-d). Experiments with closed (a/c) and open (b/d) Panama Strait were made. Response of Neodymium isotopes at ODP sites 689 and 1090 and in the Atlantic average are shown. Labels on the x-axis correspond to the bathymetries listed in Table 1. Connected asterisks show results from separate spinups, circles show results from pseudo-transient (PT) simulations.

make possibly false assumptions about the bathymetric shape of the newly opened passage.

Figure 32 shows the Drake throughflow, Panama throughflow and AMOC maximum evolution in response to the uniform Drake Passage opening. The evolution is much smoother than in the modern-world-approaching case (Figures 30d-f). Only when the depth is increased from 15 to 16 layers (corresponding to seafloor elevations of 17 to 16 layers), a slight jump is visible. The stronger increase in Drake throughflow in this step is caused by the lowering of the drag because the passage is deepened to below k_λ (compare Section 2.2.1). After that, the throughflow stays more or less constant. Because the slope of the throughflow evolution was strongly decreasing before the lowering of the drag, it may be inferred that such a Drake throughflow stagnation would also occur if the drag was not lowered. Apparently, a Drake throughflow maximum is reached at around 54 Sv to 57 Sv, which is not exceeded even if the passage is further deepened. The magnitude of this maximum is probably constrained by horizontal bathymetry, grid resolution, wind stress and drag.

In case of an open Panama Strait, the Panama throughflow is strongly negatively correlated with the Drake throughflow ($R^2 = 0.996$). This means that most of the Panama throughflow variability is caused by the changing Drake throughflow, i.e. the water masses that flow

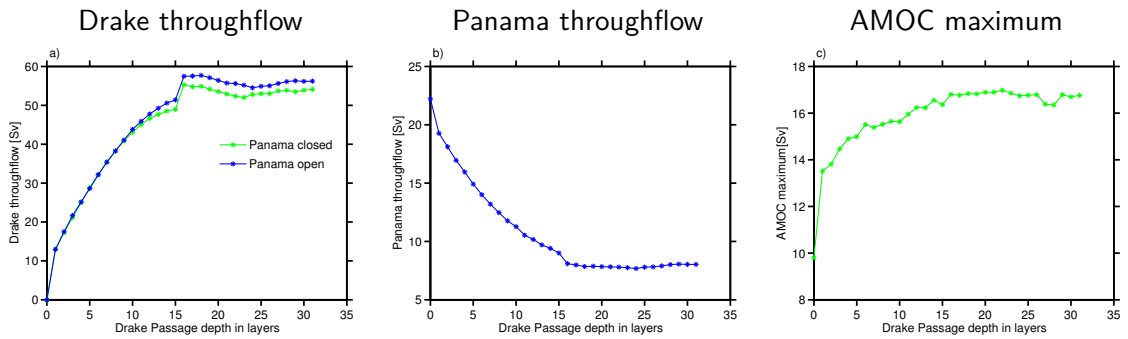

Figure 32: Uniformly opening Drake Passage from a closed state. The legend in a) is valid for all figures. Drake throughflow (a), Panama throughflow (b) and AMOC maximum (c) are shown.

through Drake Passage cannot feed into the current forming the Panama throughflow anymore. With a closed Panama Strait, the AMOC maximum is positively correlated with the Drake throughflow ($R^2 = 0.892$), implying that AMOC increase is primarily driven by the Drake throughflow (or ACC) increase.

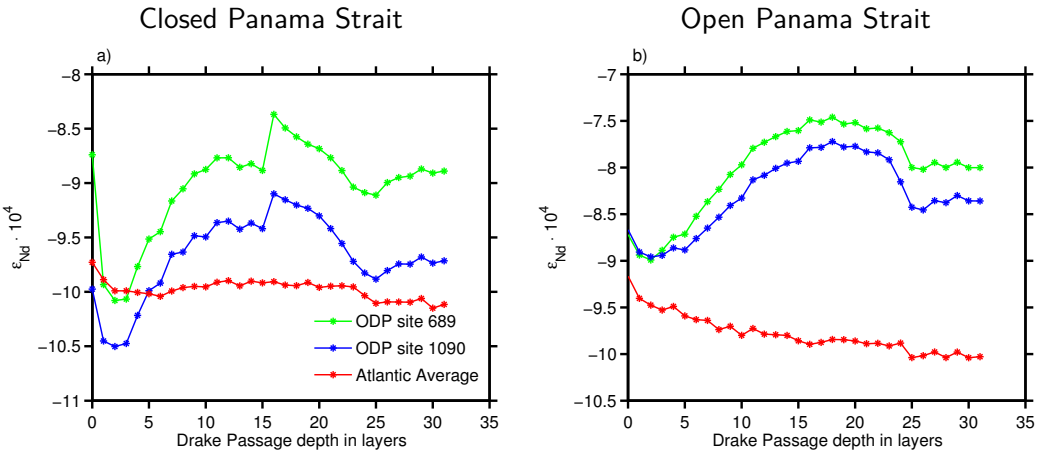

Figure 33: Uniformly opening Drake Passage, with a closed (a) and open (b) Panama Strait. Response of Neodymium isotopes at ODP sites 689 and 1090 and in the Atlantic average are shown. The legend in a) is valid for both figures.

Figure 33 shows the ϵ_{Nd} evolution in response to the uniform Drake Passage opening. Compared to the non-uniform opening experiments, a much clearer pattern is visible in the seafloor ϵ_{Nd} signature around the ODP sites, which is qualitatively very similar for both sites. The immediate effect of the opening is a significant decrease in the signature, which amounts to roughly 0.5×10^{-4} around ODP site 1090 and 1.3×10^{-4} around ODP site 689 if the Panama Strait is closed, and to only around 0.3×10^{-4} at both sites if the strait is open. A possible explanation for this decrease is the increasing strength of Southern Ocean subpolar gyres following the opening. These gyres are positioned such that they transport water masses from the strongly negative Antarctic boundary source at around 60°E to the ODP sites (especially site 689). Even though this negative boundary source is very local, its signature is so strong ($\epsilon_{Nd} = -40 \times 10^{-4}$, compare Figure 1c in Rempfer et al. (2011)) that it may cause this effect.

The initial decrease is followed by an increase which lasts up to intermediate Drake Passage depths around 1200 m. With a closed Drake Passage, the increase amounts to 1.4×10^{-4} (ODP site 1090) and 1.7×10^{-4} (ODP site 689). It would probably already cease at a shallower depth if the drag was not lowered at a depth of 16 layers, which creates a discernible spike in the ϵ_{Nd} evolution. With an open Panama Strait, this spike is not visible, but the increase is similarly strong (1.3×10^{-4} and 1.5×10^{-4}) and flattens out smoothly at a depth of 15 to 17 layers. Both the weaker initial decrease and the missing peak in the open Panama Strait case may be explained by the moderating effect of the Panama throughflow, which also transports radiogenic Pacific water masses to the ODP sites. This makes the ϵ_{Nd} response in these regions less sensitive to the Drake throughflow and also explains the slightly weaker increase, because the Panama throughflow is decreasing when Drake Passage is opened. However, based on the previous Nd experiments, we would expect that this weakening effect would have a larger impact on the increase. The weakening is probably so slight because the the increase is more strongly enhanced by MOC changes if the Panama Strait is closed than if it is open. Both the more complete shutdown of the AMOC and the stronger SOMOC increase ϵ_{Nd} in the Atlantic Southern Ocean (Rempfer et al., 2012).

Pseudo-transient simulations

Regarding throughflow strengths, the agreement between spinups and pseudo-transient simulations is overall very good. The most notable deviations are found in Drake throughflow during the Panama Strait opening, and in Panama throughflow during Drake Passage opening. But even those are slight enough to be reasonably explained by the interpolations that were made in the pseudo-transient simulations. Also the ϵ_{Nd} signatures of the pseudo-transient simulations are generally in good agreement with the spinups, except for a very large deviation in the first opening step. In this pseudo-transient step, there is an ϵ_{Nd} increase of about 1.5×10^{-4} in the whole Atlantic, accompannied by a similarly strong decrease in the Pacific and most surprisingly, a vast global increase in seafloor $[Nd]_d$ (not shown). The reason for these changes is largely unknown, but it is hardly credible that the opening should have such a huge global impact, especially since this is not seen in the spinup opening. Also the fact that this effect occurs independently of how deep Drake Passage is opened is suspicious, as it creates two much different ϵ_{Nd} signatures for, e.g., DRC4 (compare Figure 31a to 31c or 31b to 31d). However, no error was found, as the Nd isotopes are treated identically to the other tracers including T and S, which do not show such an anomaly. This may lead to the hypothesis that the boundary source could be cause of the problem, but again the impact should not be so large. Also, ϵ_{Nd} in the second step of the pseudo-transient opening is virtually identical to the spinup method, meaning the pseudo-transient simulation series recovers from the large deviation very quickly. We hence note that the pseudo-transient method is overall suitable for Nd simulations, but shows a weakness in the first Drake Passage opening step. Therefore, and for time-saving reasons, it was decided to model the uniform Drake Passage opening only with separate spinups.

3.2.3. Influence of Drake Passage on Neodymium isotopes: model-data comparison

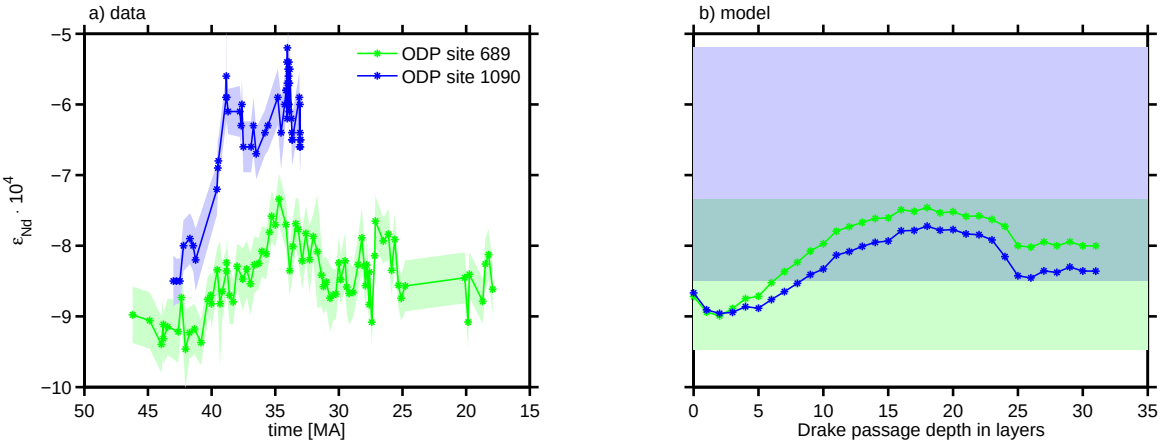

Figure 34: ϵ_{Nd} data from marine sediment cores from ODP sites 689 and 1090 (a), and simulated seafloor ϵ_{Nd} evolution in response to DP opening with an open Panama Strait (b). Data in a) were taken from Scher and Martin (2004, 2006), shaded areas show the 2σ-uncertainty intervals as estimated therein. In b), shaded areas show the range of measurements from a), colors corresponding to the two different sites, uncertainties not included.

Figure 34 shows a comparison between the modeled seafloor ϵ_{Nd} evolution and data from marine sediment cores from ODP sites 689 and 1090. The data are taken from Scher and Martin (2004, 2006), including the uncertainty estimates made by them. The model evolutions are taken from Drake Passage opening simulations with an open Panama Strait, which were already described in Section 3.2.2 (Figure 33b). The open Panama Strait case was chosen for the comparison because the strait was open in the Eocene. A direct quantitative comparison is not made, because this would require assigning a date to the modeled opening steps, which is impossible because the opening is simplified and does not correspond to real Drake Passage bathymetries. But the qualitative agreement between modeled and measured seafloor ϵ_{Nd} for ODP site 689 is striking. Both series show an increase followed by a slighter decrease and stabilization around a new equilibrium value. Even the range of values is similar, although the simulated range is slightly narrower because the increase starts at a higher ϵ_{Nd}. This may be explained by the Panama throughflow which is stronger than in Eocene GCM simulations (compare Section 3.4), increasing ϵ_{Nd} in the Atlantic Southern Ocean as described in Section 3.2.1.

For ODP site 1090 on the other hand, the model-data agreement is worse. The only common feature which is also found there is an overall ϵ_{Nd} increase. But the magnitude of the increase is much different. The simulated increase is very similar to, and slightly weaker than, the simulated increase around site 689. The measured increase already starts from a higher value and is much more pronounced. Two main reasons are suggested for this difference: Firstly, the model seafloor values are averaged over a very large region around both sites (roughly 30° (lon.) 15° (lat.)), with a latitudinal band of only 5° between both regions. This equalizes the two ϵ_{Nd} evolutions. Secondly, Scher and Martin (2006) elaborate that one of the main reasons for the difference in the two records is the elevation difference between the two sites.

They state the Eocene paleodepths to be 3700 m (site 1090, Agulhas ridge) and 1600 m (site 689, Maud rise). In the bern3d standard bathymetry, both sites and their surroundings are deep ocean due to the coarse resolution (Maud rise is not resolved), such that the averaging only includes ϵ_{Nd} values of depths between 3000 m and 5000 m.

From these results, we conclude that the measured increase in seafloor ϵ_{Nd} east of Drake Passage could indeed correspond to a Drake Passage opening. One might further infer that the opening took place earlier than the onset of the increase, because modeled ϵ_{Nd} shows a slight decrease as a first reaction to the opening. Such a decrease also seems to be visible in the data from ODP site 689, but it might well turn out to be a statistically insignificant deviation from a pre-opening equilibrium value if the record was prolonged. We will however not make this inference, as the cause of this small decrease in the model is not yet understood.

3.3. From standard to double resolution: modern and Eocene maps

The goal of this section is to explore the effects of doubling the model resolution on the physical model state. For this purpose, the model was run with the bathymetries MOD2X and EO2X, which are exact duplicates of the CTRL bathymetry and the preliminary EO36 bathymetry, but with doubled model resolution in longitude and latitude. The transition from EO2X to EO72, the final Eocene bathymetry which has an actual resolution (not just model resolution) of 72×72 grid cells, is also described in this section. Compare Section 2.5 for more details on the bathymetries.

Figures 35 to 40 compare MOD2X to CTRL, EO2X to EO36, and EO72 to EO2X. Ocean circulation, SST, atmospheric temperature, albedo, and SSS are shown, differences are taken where applicable. Since the doubling of the resolution is not the main topic of this thesis, only the most prominent features are shortly described in the following. The model's behavior in EO36 (resp. EO2X) is not separately discussed or compared to the modern bathymetry, because EO72 is the Eocene map of main interest. The circulation in EO72 is further investigated and compared to a comprehensive GCM in Section 3.4.

Most differences in barotropic ocean circulation can be explained by the fact that the regions of increased drag (compare Section 2.2.1) are smaller when the resolution is doubled. This enables the stronger ACC in MOD2X and EO2X versus CTRL and EO36. The gyres in the northern hemispere are also strengthened. However, as the wind stress forcing is not enhanced, the kinetic energy input into the double resolution simulations is the same as into the standard resolution simulations; and although a smaller fraction is lost due to frictional dissipation, the gyres in the southern hemisphere are not strenghened, because a larger fraction of this energy feeds into the ACC. In MOD2X, they are even slightly weakened, because the Drake throughflow gets so strong (68 Sv) and the ACC extends to lower latitudes below the Indian Ocean. In the Eocene simulations, the effects of reduced drag and increased Drake throughflow compensate, such that the strengths of the single gyres in the southern hemisphere are roughly equal in EO2X, EO36 and EO72. The figures are misleading in this respect because the stream function values are shifted, as was also observed in Section 3.2.1. A better measure for the gyre strength is the difference between the gyre maximum and the outermost closed stream line. For the South Pacific gyre for example, one could take the difference between its maximum and the stream funcion value east of South America, which is about 30 Sv in EO2X, EO36 and EO72. However, the matter is complicated by the fact that the gyre is connected to a global anticlockwise supergyre in EO72 and EO36, which is split into two gyres in EO2X. This splitting is related to the direction of the Panama throughflow and the clockwise gyre forming west of the Panama Strait, which also arises in some modified EO72 bathymetries and is further discussed in Section 3.4. The supergyre is stronger in EO72 than in EO36, because it is linked by the throughflows through Tethys seaway and Panama Strait, which are enhanced in EO72 due to the reduced drag.

The global overturning is very similar for all three Eocene configurations. However, the

AMOC is weakened and separated from the stronger SOMOC in EO2X compared to EO36. This is directly related to the change in polar temperatures and Southern Ocean sea ice formation described below. It is probably also related to the freshwater flux correction that was applied to the Ross and Weddell Seas in CTRL, but not in MOD2X.

The most notable feature in the SST and atmospheric temperature distributions is a strong cooling over the southern ocean in MOD2X compared to CTRL. What triggers the cooling in the first place would require further investigation, but certainly it is strongly enhanced by the ice-albedo feedback. Stefan Ritz also found that the sea ice in the model is very sensitive to resolution changes, because the sea ice albedo is set to 0.8 in the standard setting, which creates a strong feedback once a cooling is triggered (pers. comm.). Therefore, he set the ice albedo to a lower limit of 0.65 in the variable-grid version of the model.

Figure 39 shows the surface albedo of the different simulations. The land albedo is prescribed by the exact same mask in the two modern simulations, and set to a constant value in the Eocene simulations as described in Section 2.9.1. Sea ice formation is well visible as regions of maximum albedo over the ocean. Large potions of the Southern Ocean are covered with sea ice in MOD2X, much more than in CTRL; this enhances the cooling described above. Similarly, as the Eocene Arctic Ocean is only resolved in EO72 and sea ice is formed there, the region is strongly cooled compared to EO2X due to the ice-albedo-feedback.

In the salinity plots of EO2X and EO72 in Figure 40, the colorbars have been shifted by 2.2 and 2.0 psu, respectively. This has been done to correct for a recorded offset in the global salinity inventory in these Eocene runs. The offset is not related to the EBM, but stems from the restoring boundary conditions. Because interpolated modern salinity fields were used for the restoring spinup of the Eocene maps, a large potion of the Tethys Seaway was restored to very high salinities, originating from the small Mediterranean which was spread out to a large region by the interpolation. The resulting offset is therefore not physical or related to the Eocene map, which is why it was corrected for in the figures. Apart from this offset, the only prominent differences are found in the Arctic regions. Arctic water masses are more saline in MOD2X and EO2X than in CTRL and EO36. Their salinity is so low in CTRL and EO36 because freshwater is brought there by precipitation (and runoff, but in EO36 the runoff was modified such that none flows into the small Arctic basin), and cannot be mixed with saltier water masses quickly because the connections to the other basins are so shallow and narrow. With double resolution, the Bering Strait and the connection to the Tethys Seaway are both two boxes wide, instead of one. While there can still be no Sverdrup transport through the latter, diffusion is enhanced, enabling a better water exchange with the small Arctic basin. Bering Strait throughflow in MOD2X is increased to 1.32 Sv from 0.36 Sv, causing the Arctic salinity to approach the values found in the North Atlantic and North Pacific.

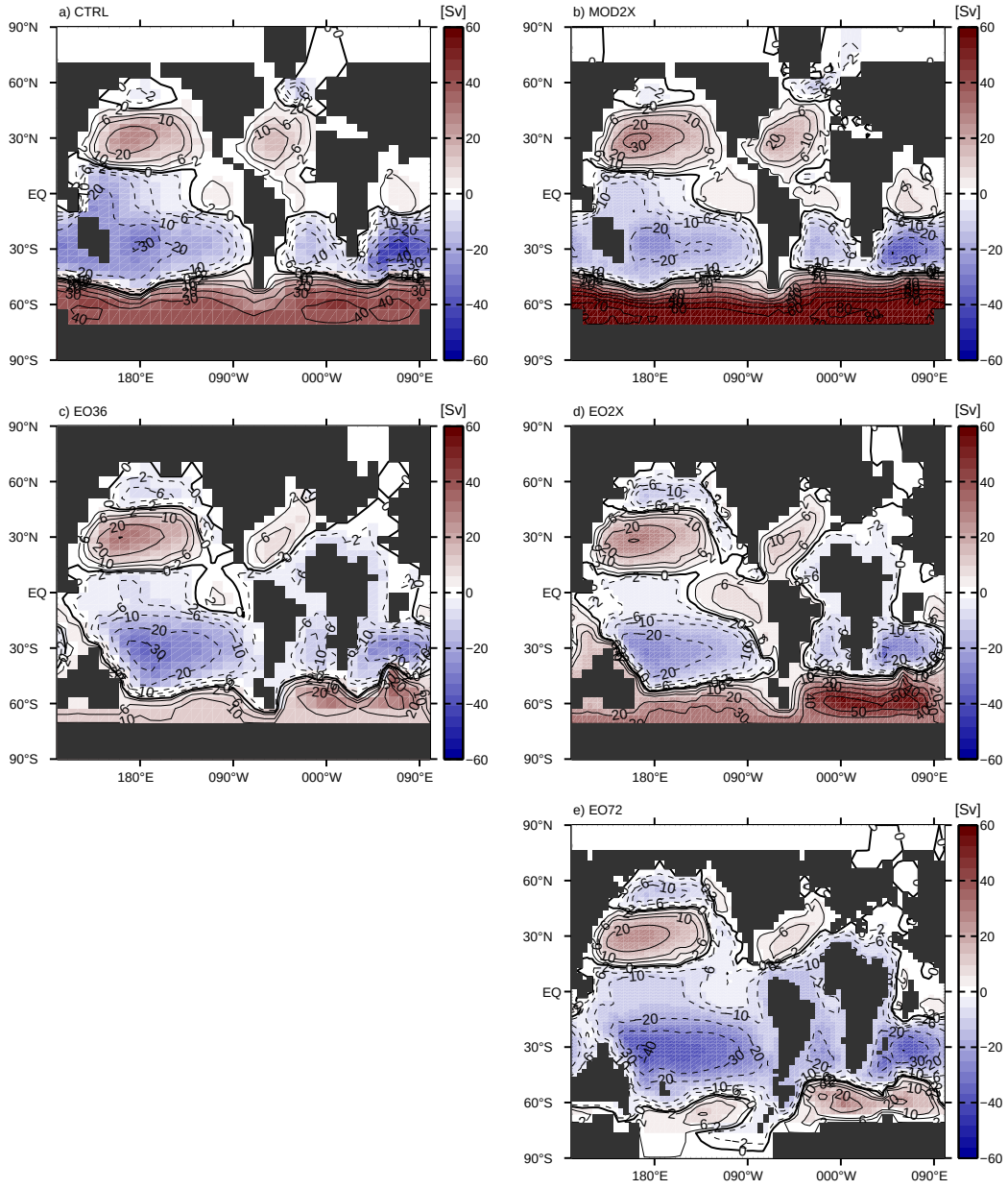

Figure 35: Impact of a doubling of the model resolution (a-d) and bathymetry resolution (e) on depth-integrated ocean circulation. Colors and contours show the barotropic stream function in Sverdrup (Sv).

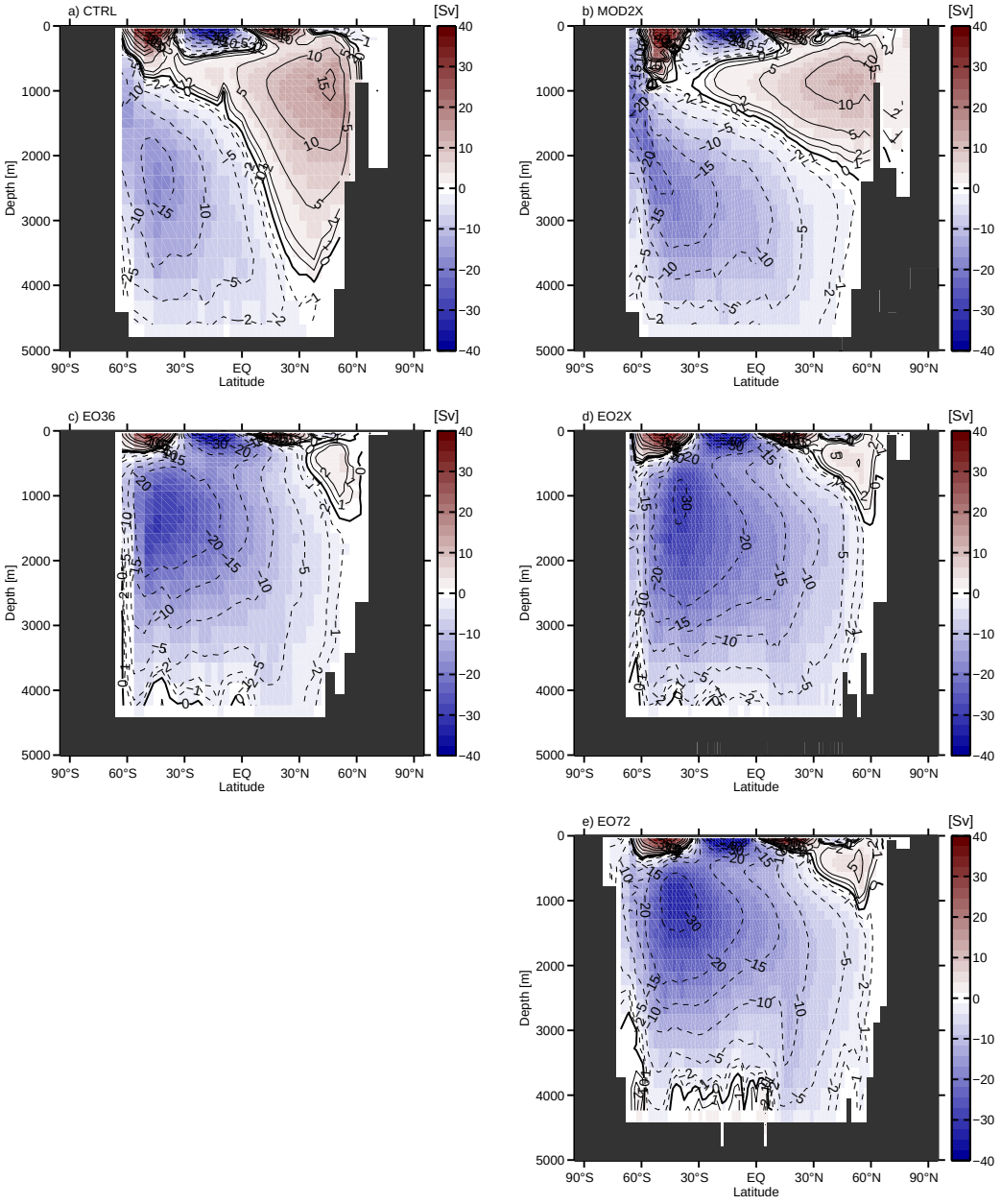

Figure 36: Impact of a doubling of the model resolution (a-d) and bathymetry resolution (e) on GMOC. Colors and contours show the stream function in Sverdrup (Sv).

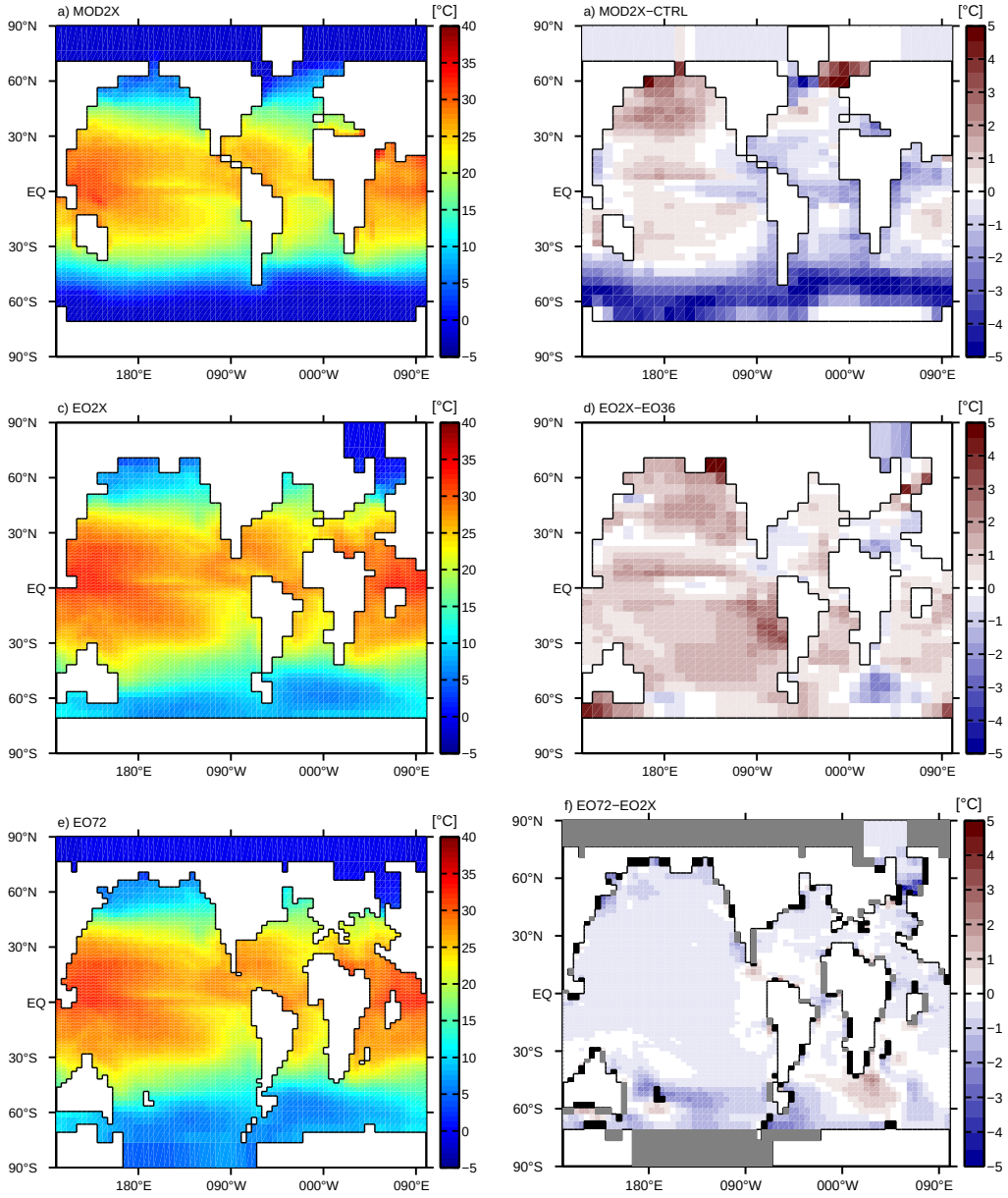

Figure 37: Impact of a doubling of the model resolution (a-d) and bathymetry resolution (e-f) on SST. a), c) and e) show the SST distributions in the simulations with double resolution, b), d) and f) their differences to the corresponding simulations with standard resolution. In f), regions that are only land in EO2X but not in EO72 are shaded in gray, and regions where the opposite is the case are shaded black.

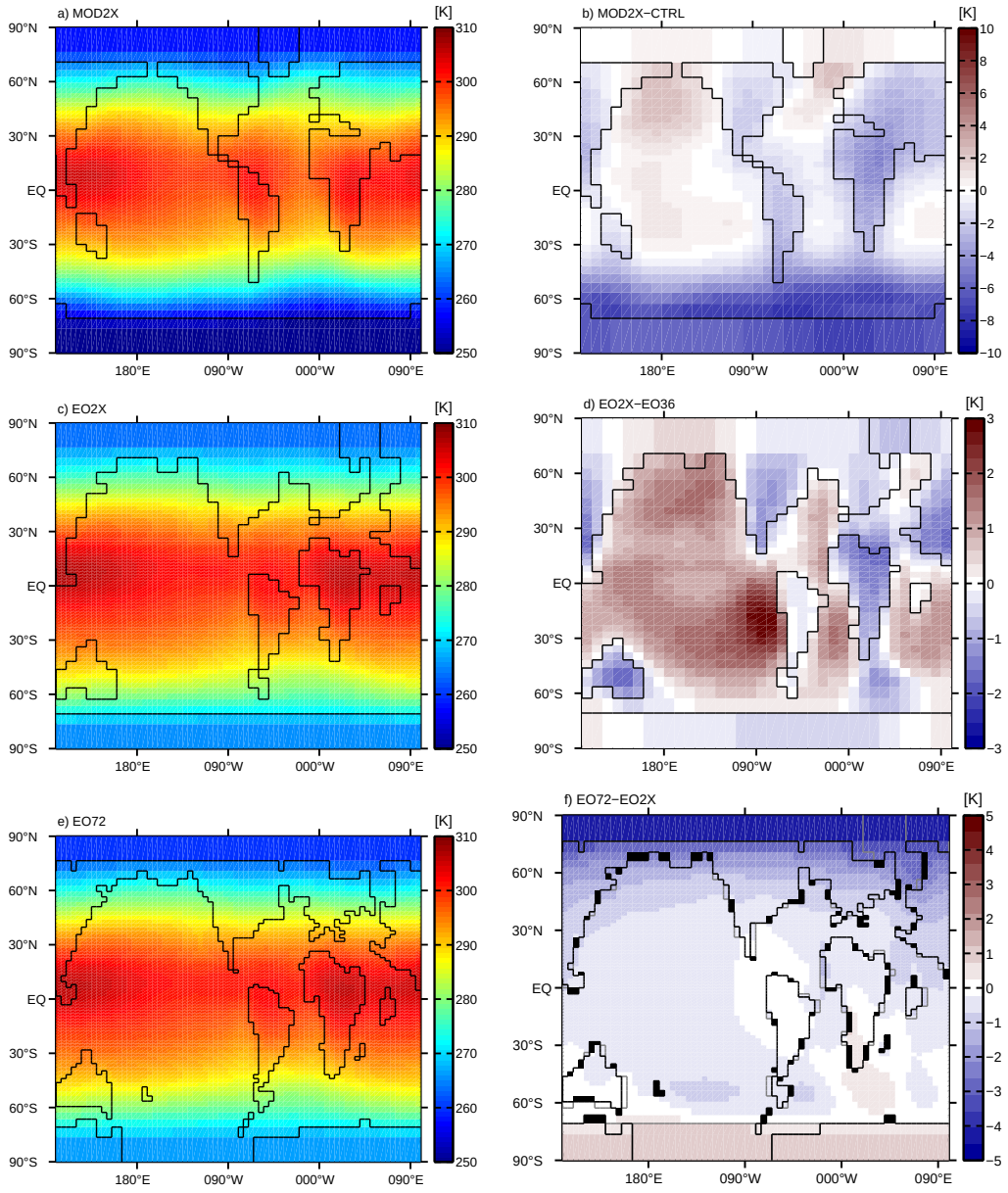

Figure 38: Impact of a doubling of the model resolution (a-d) and bathymetry resolution (e-f) on atmospheric temperature. a), c) and e) show the atmospheric temperature distributions in the simulations with double resolution, b), d) and f) their differences to the corresponding simulations with standard resolution. In f), regions that are only land in EO2X but not in EO72 are enclosed in gray lines, and regions where the opposite is the case are shaded black.

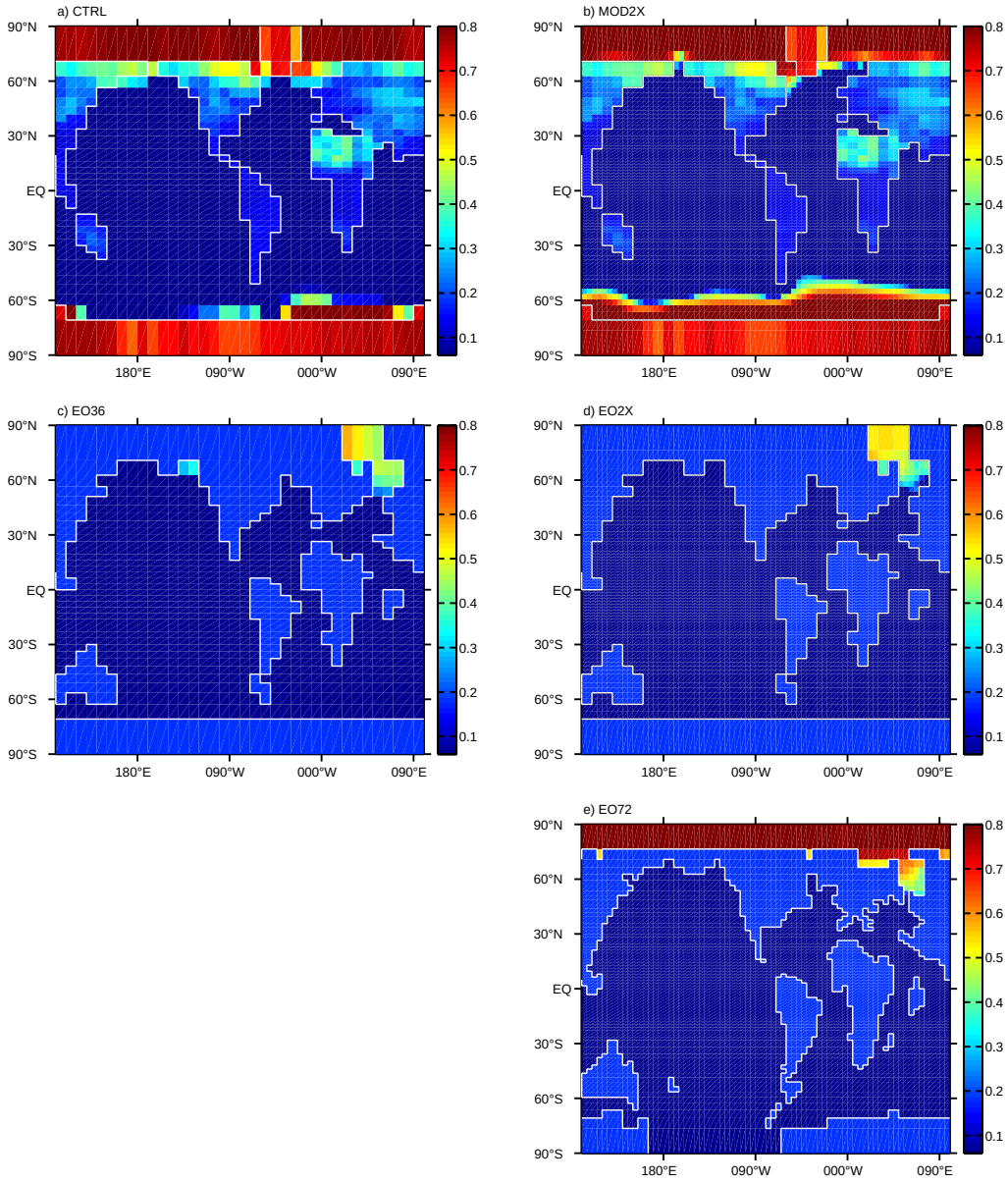

Figure 39: Impact of a doubling of the model resolution (a-d) and bathymetry resolution (e) on surface albedo (including sea ice). The land surface albedo is prescribed by a climatology in the modern case (a,b) and set to a constant in the Eocene case (c-e). The sea ice leading to high albedos in some ocean regions is simulated.

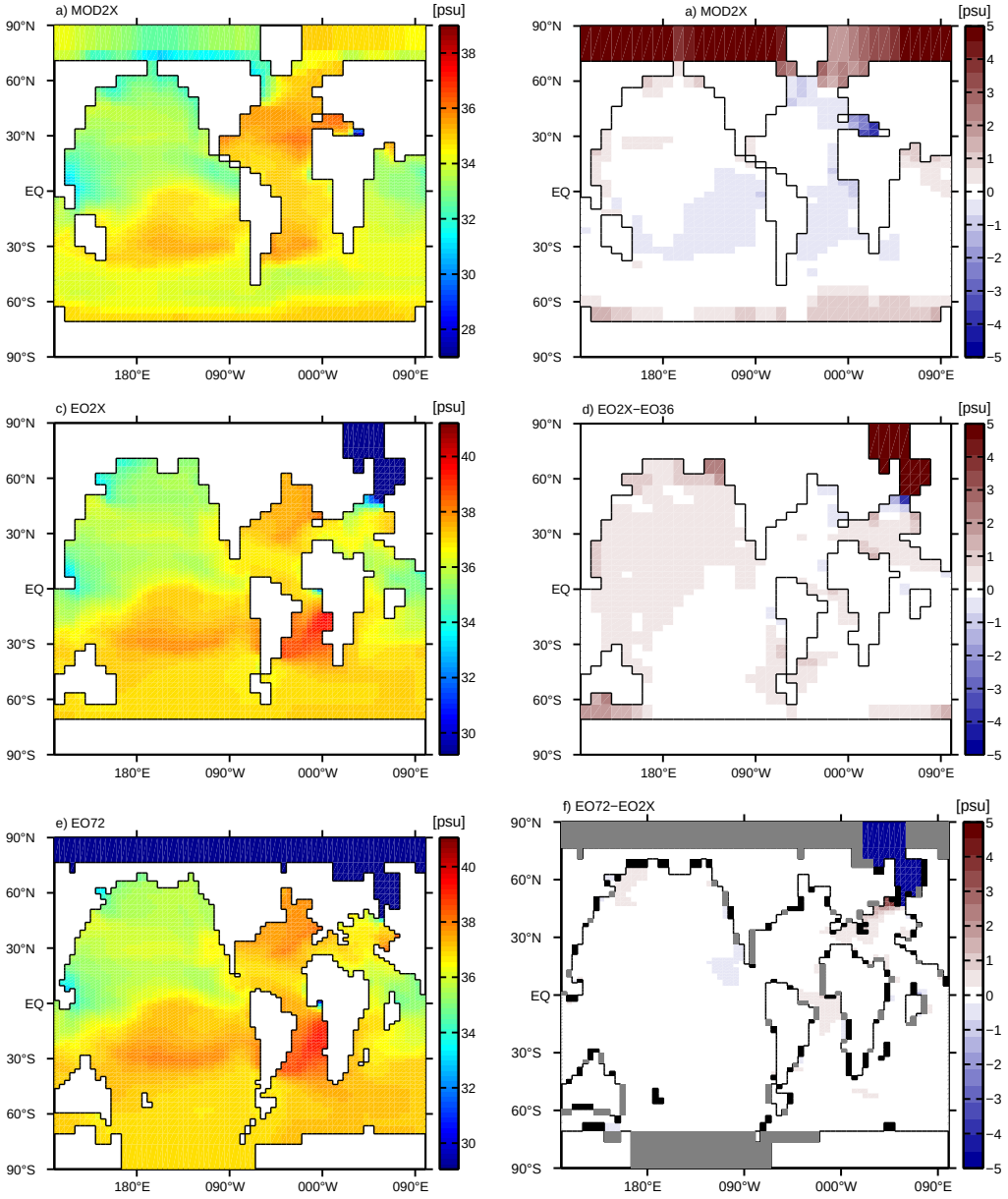

Figure 40: Impact of a doubling of the model resolution (a-d) and bathymetry resolution (e-f) on SSS. a), c) and e) show the SSS distributions in the simulations with double resolution, b), d) and f) their differences to the corresponding simulations with standard resolution. In f), regions that are only land in EO2X but not in EO72 are shaded in gray, and regions where the opposite is the case are shaded black.

3.4. Eocene ocean circulation: comparison with a comprehensive GCM

In this section, the ocean circulation in various representations of the Eocene bathymetry in the Bern3d model is compared to the circulation simulated by the MPI ocean model (MPI-OM) in an Eocene setting. This model was chosen for comparison because its Eocene setting is well documented by Heinemann (2009), and its bathymetry in the region of interest is similar to the bathymetry we used.

No other climate information than ocean circulation is compared, because the only boundary conditions that were modified from CTRL in the Eocene simulations (apart from the few necessary adaptations listed in Section 2.9.1) were the bathymetry and the albedo. To simulate Eocene climate, various climate forcings should be modified additionally. Most importantly, the atmospheric CO_2 partial pressure (pCO_2; or corresponding radiative forcing) should be increased; Eocene model studies are usually made with a pCO_2 between 2× preindustrial (560 ppm) and 16× preindustrial (4480 ppm) (Heinemann, 2009; Lunt et al., 2012). Bern3d Eocene simulations with such an increase in CO_2 radiative forcing were carried out for testing purposes. However, they did not cause drastic circulation changes as in the MPI-OM (see Figure 42; the barotropic circulation of the Eocene simulations with increased pCO_2 is not shown, because it is very similar to the barotropic circulation in EO72).

Figure 41a shows the Eocene landmask in the MPI-OM and the corresponding ciruclation in the simulation with a pCO_2 of 560 ppm, hereafter referred to as PE. The landmask in the northern hemisphere looks different from the landmask we used, in that a greater fraction of the Tethys region is ocean and more islands are resolved. However, the additional ocean regions are very shallow and do not feature strong currents, such that their influence on the global circulation is relatively small. As in EO72 (Figure 41b), both the Tasmanian Gateway and the Drake Passage are open, but very shallow. The most notable difference is that the Antarctic peninsula is not detached from the continent as in EO72. Therefore, a bern3d bathymetry in which the peninsula was reconnected (BOT2, compare Table 2) is also shown in the comparison, Figure 41c.

A different color scale was chosen for the Bern3D circulation to better visualize the gyres, which are generally weaker than in MPI-OM. This was expected as the standard modern CTRL state shown in Section 2.2 also produces weaker gyres than GCMs. The qualitative agreement between gyre shapes is good, except for the narrow gyres around the equator which are missing in EO72, as they are also missing in CTRL. The various minor throughflows listed in the northern hemisphere of PE are zero by definition in the Bern3D Eocene simulations, because the northern continental area (Eurasia and North America) is one single land mass.

The flows through the Tethys Seaway and the Tasmanian Gateway in EO72 and BOT2 are in good agreement with PE. The Drake throughflow is stronger, even in BOT2 where the Drake Passage opening is actually smaller. The largest difference is found in the Panama

throughflow: EO72 and BOT2 show a strong throughflow in the opposite direction of the net Panama throughflow in PE. However, the Panama throughflow in the Bern3D Eocene setting is highly sensitive to bathymetric modifications in the Drake Passage and Tasmanian Gateway region. Although the flow is directed from east to west in most cases (compare Section 3.5), Figures 41d and 41e show two bathymetry examples (WIDE1 and OTOP2) with a Panama throughflow from west to east. However, this flow is still different from the one in PE, because it feeds into the North Atlantic gyre before becoming a WBC along South America. Also, it can be seen that the Drake Passage bathymetries creating this Panama throughflow are more different from PE than EO72 and EO2X.

Finally, two modified modern bathymetries are shown in Figures 41f and 41g (TRIO31 and PD4 compare table 1). These are included in the comparison because they were each used in one of the Neodymium experiments: TRIO31 in the uniform opening, PD4 in the proportional opening (compare Section 3.2.2). Evidently, in these two cases only the Panama throughflow and Drake throughflow can be compared to PE. Although we think that the uniform opening produces more robust Nd results than the proportional opening, we see that PD4 is in better agreement with PE than TRIO31 with respect to throughflows. But also in TRIO31, the Panama throughflow goes in the same direction as in PE. However, it also feeds into the North Atlantic like in WIDE2 and OTOP2.

Figures 42a shows the GMOC in a second MPI-OM simulation named PE1, Figure 42b shows the GMOC in PE. The only difference between the two runs is the atmospheric pCO_2, which is 280 ppm in PE1 and 560 ppm in PE. This difference creates two completely different GMOC patterns: increasing the pCO_2 from PE1 to PE nearly shuts down the SOMOC. The AMOC is also stronger and especially deeper in PE1 than in PE, but this is not so well visible in the GMOC because the strong Southern MOC cell extends up to the North Pacific.

Figures 42c and d show the GMOC in EO72 and EO2C, a Bern3D simulation with the same bathymetry as EO72 but a pCO_2 of 560 ppm. They both show a similar GMOC, with a stable SOMOC and a nearly shut down AMOC. The GMOC of the other Eocene representations included in Figure 41 is not shown, because it is very similar in all representations. In the modified modern cases, the latter is mostly due to the Panama throughflow, as explained earlier in Section 3.2.1. In in the bathymetries that were modified from EO72, the formation of NADW is additionally hindered by the land mass extending to lower latitudes, and the AMOC is probably further suppressed by the narrow Atlantic basin. The Southern hemispheric GMOC in EO72 is in reasonable agreement with the southern hemispheric GMOC in PE1, which was forced by the same atmospheric pCO_2. But the shift to a different overturning regime due to a doubling of pCO_2 is not seen in the Bern3D model, the circulation is just slightly enhanced in EO2C.

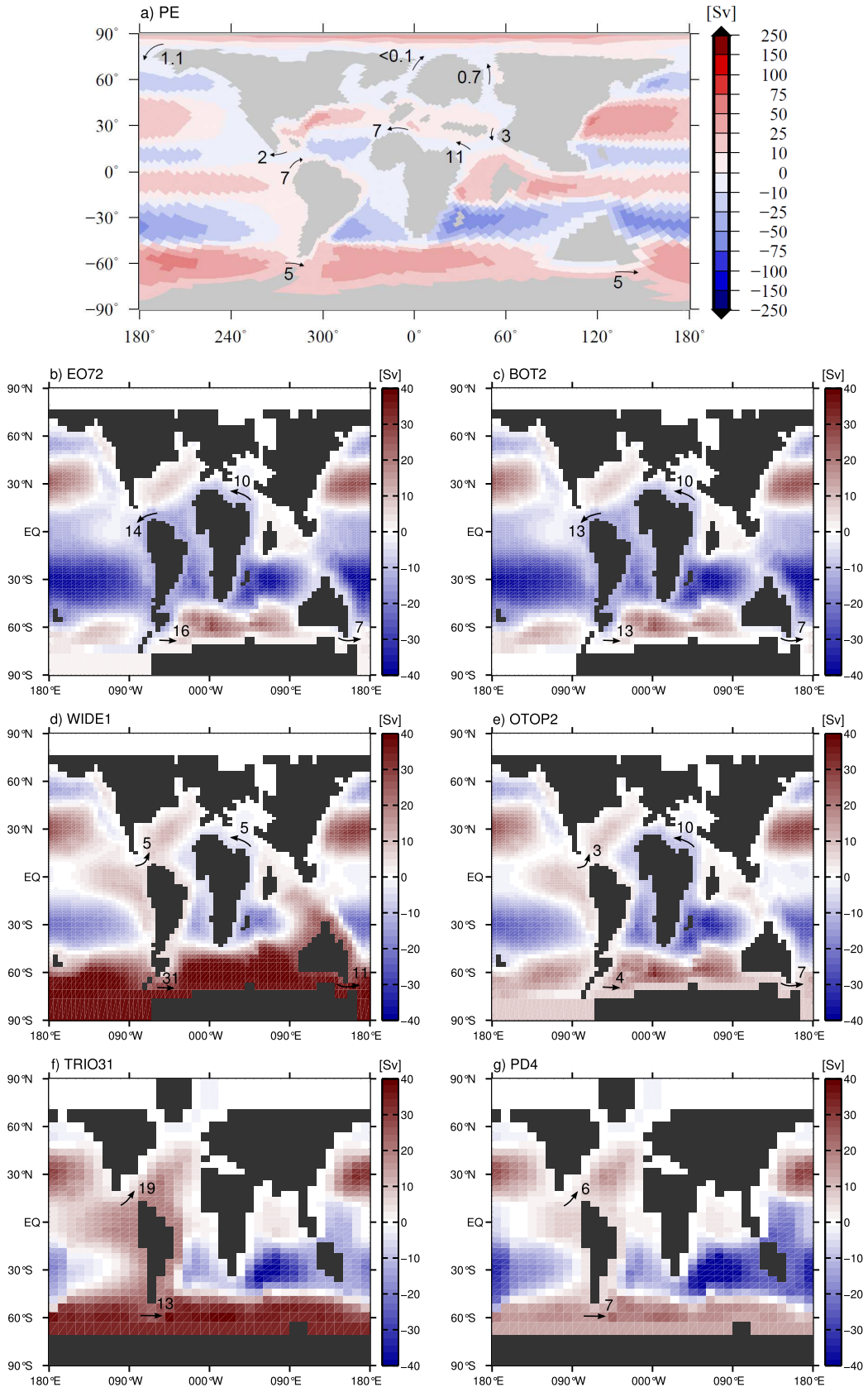

Figure 41: Depth-integrated ocean circulation and throughflows in MPI-OM and Bern3D simulations. Colors show the barotropic stream function, arrows and numbers the throughflows, both given in Sverdrup (Sv). Figure a) is taken from Heinemann (2009) and shows the MPI-OM Eocene simulation PE (pCO_2 = 560 ppm). Figures b)-g) show Bern3D simulations with different bathymetries, labels according to Tables 2 (b-e) and 1 (f-g).

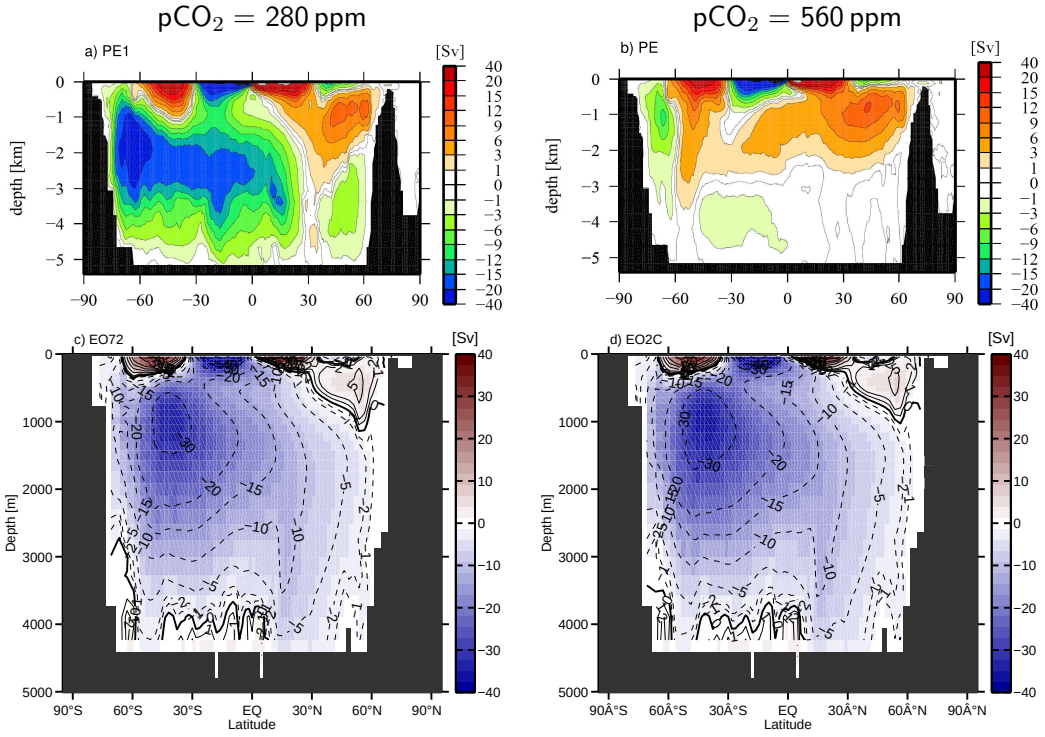

Figure 42: GMOC in MPI-OM and Bern3D simulations with different CO_2 radiative forcings. Colors and contours show the stream function in Sverdrup (Sv). Figures a) and b) are taken from Heinemann (2009) and show the MPI-OM Eocene simulations PE1 ($pCO_2 = 280$ ppm) and PE ($pCO_2 = 560$ ppm). Figures c) and d) show the Bern3D simulations EO72 (with $pCO_2 = 280$ ppm) and EO2C (same bathymetry, but $pCO_2 = 560$ ppm).

3.5. Tectonic rearrangements in the Eocene bathymetry

In this section, the influence of the two Southern Ocean gateways in the Eocene map on ocean circulation is investigated, with a focus on Drake throughflow, Panama throughflow and flow through the Tethys Seaway. This should also help decide whether the EO72 bathymetry, combined with the tested opening methods, is suitable for future experiments with Neodymium in an Eocene setting. Drake Passage was closed from EO72 in two series of five steps, as described in Section 2.9.2. In the first series shown in Figures 43a,c and e, the precursor of the Antarctic peninsula was closed from the North, i.e., first connected to the tip of South America, and only thereafter to Antarctica. In the second series shown in Figures 43b, d and f, the order was reversed. Both series were carried out with four different configurations of the Tasmanian Gateway: normal (as in EO72), shallower, closed, and deeper (compare Table 2). Abbreviations used for bathymetries are listed in Table 2.

Figures 43a and b show the Drake throughflow in these experiments. Two main inferences can be made from those figures: Firstly, the Drake throughflow is not strongly influenced by the Tasmanian Gateway, as the normal, shallow and closed Tasmanian Gateway states all produce a similar throughflow at all stages of the Drake Passage closing. If the Tasmanian Gateway throughflow is weakened or ceases, the flow around Australia is enhanced, feeding into the WBC along Australia and thereafter into the Drake throughflow. Only when Tasmanian Gateway is deepened, the Drake throughflow is also significantly increased, because the

ACC is enhanced; Tasmanian Gateway throughflow is increased from 7 Sv to 12 Sv, which is an even higher relative increase than in the Drake throughflow. The Drake throughflow increase is strongest when water masses are allowed to flow through the unaltered northern Drake Passage opening, i.e., in the first step in Figure 43a and the first three steps of Figure 43b. This leads to the second inference that the northern opening is more important for Drake throughflow than the southern opening. This effect is largest when Tasmanian Gateway is deepened, but it is also visible in the other cases. With an unmodified Tasmanian Gateway for example, the Drake throughflow is still about 13 Sv when the southern opening is closed, and only about 7 Sv when the northern opening is closed. This is probably because the flow through the northern opening is much more direct, as seen in Figure 35e. Although the southern opening consists of more ocean cells, it lies south of the maximum wind forcing region, such that water masses only pass it after having been deflected from the island blocking Drake Passage.

The Panama throughflow, as seen in Figures 43c and d, is more sensitive to modifications of the Tasmanian Gateway. Interestingly, both a closed and a deeper Tasmanian Gateway weaken the throughflow, though the effect is stronger in the latter case. With a deeper Tasmanian Gateway, the throughflow gets so weak that it may even be reversed when the Drake Passage bathymetry is modified. Figure 44 shows the ocean circulation in TAS2 (a) and TAS3 (b), Eocene bathymetries with an unmodified Drake Passage and a closed or deepened Tasmanian Gateway, respectively. It reveals that a clockwise gyre emerges west of the Panama Strait, which is only slightly visible in TAS2 and fully formed in TAS3. Because the Panama throughflow is an east-to-west flow in EO72, it is counteracted and weakened by this gyre. If the gyre is further strengthened, it reverses the Panama throughflow, as seen in Figures 41d and e. In these simulations (TDO4 and WIDE2), the gyre is as strong as 10 Sv and also much larger. One might speculate that the gyre's strength is related to the kinetic energy from the Southern Ocean water masses that are deflected before Drake Passage, i.e., that it is anticorrelated to Drake throughflow. But Figures 41d and e falsify this speculation, showing that a strong gyre can emerge in a setting with both a very weak and a strong Drake throughflow. The real cause of the gyre is thus not understood, and should be investigated if it is decided to use these bathymetries in future experiments. Similarly complicated is the effect of Drake Passage closing on the Panama throughflow. The overall picture shows a slight weakening, but this is not consistent in all closing steps, suggesting a more complex relationship that is not further explored here.

Figures 43e and f show the response of the Tethys Seaway throughflow to a closing of Drake Passage and modifications of the Tasmanian Gateway. Again, the closed Tasmanian Gateway creates more similar values to the deepened Tasmanian Gateway than the normal and shallow states. An overall increase in Tethys Seaway throughflow strength is observed, except for the very first closing step from the South, which causes a slight decrease. The evolution of the Tethys Seaway throughflow is closely linked to the strength of the Indian Ocean gyre that drives it. This gyre's strength increases with decreasing Drake throughflow strength, probably because this also weakens the subpolar gyres south of the Indian Ocean and allows

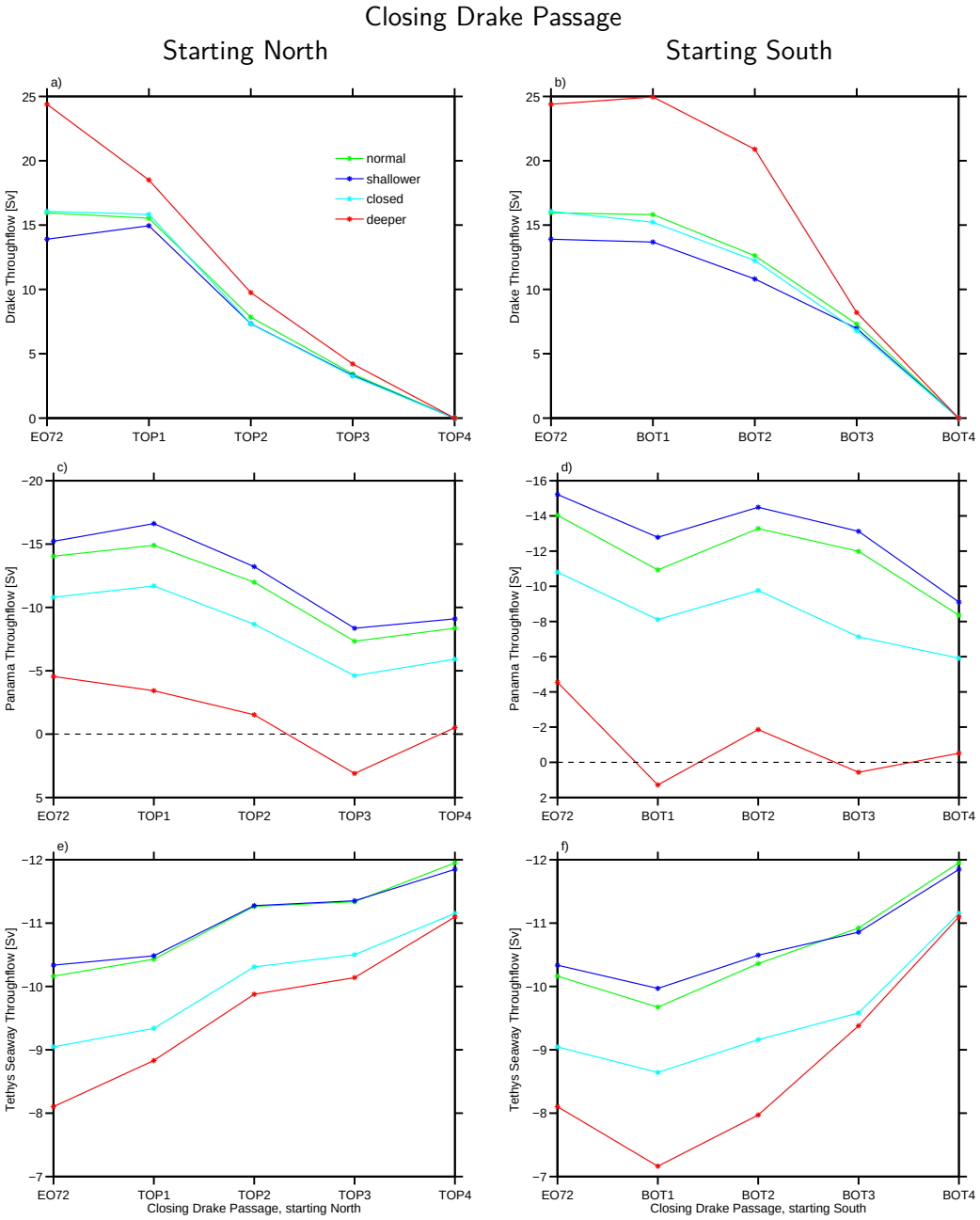

Figure 43: Evolutions of Drake throughflow (a,b), Panama throughflow (c,d), and STF (e,f) in response to a Drake Passage closing from EO72, compare Table 2. The left column shows a closing starting from the South, the right column from the North. Differently colored lines show different depths of the Tasmanian Gateway, as indicated by the legend. Positive values indicate flow from west to east, negative values correspond to flow from east to west. Labels on the x-axis are bathymetry names as listed in Table 1, and correspond to the case with a normal Tasmanian Gateway. For the cases with a shallower/closed/deeper gateway, EO72 is replaced by TAS1/TAS2/TAS3, and a prefix (S/C/O) is added to the other labels.

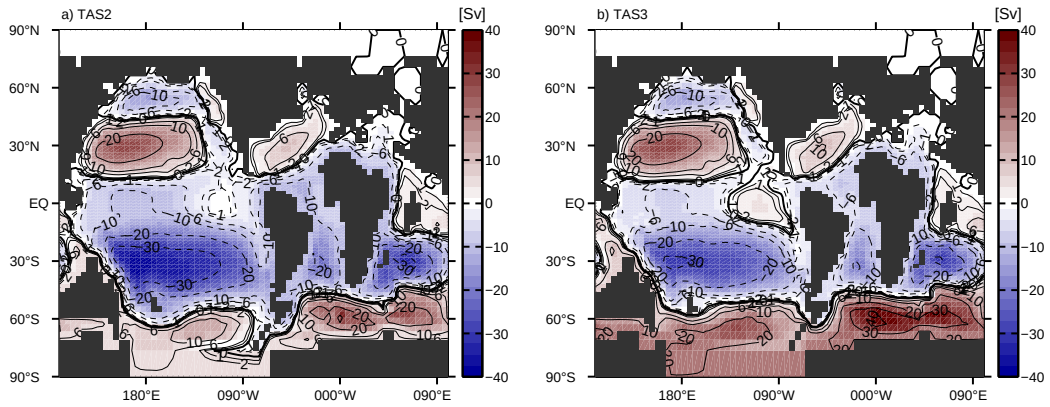

Figure 44: Depth-integrated ocean circulation in an Eocene simulation with closed Tasmanian Gateway (a) and one with deepened Tasmanian Gateway (b). Colors and countours show the barotropic stream function in Sverdrup (Sv).

the Indian Ocean gyre to expand latitudinally. Therefore, the (absolute value of the) Tethys Seaway throughflow is negatively correlated to Drake throughflow, with an average coefficient of determination of $R^2 = 0.950$, where $R^2 > 0.900$ in all 8 cases.

As a final experiment, the precursor of the Antarctic peninsula was shrunk stepwise and finally removed, to see what the Drake throughflow would be like in the Eocene setting without this obstacle. As detailed in Table 2, the Tasmanian Gateway was deepened at the same time to achieve maximal stimulation of the ACC. In the first opening step, the island is shrunk from three to two land cells, which was done both from the southern and from the northern end. Thereafter, it is completely flooded and deepened.

The results of this opening and widening experiment are shown in Figure 45. Again, Panama throughflow, Drake throughflow and Tethys Seaway throughflow are shown. An overall increase in Drake throughflow up to 38 Sv is observed, which is still less than in the modern simulations because the ACC is hindered by Australia in the Eocene configuration. An overall decrease is found in the Tethys Seaway throughflow, which is in agreement with the negative Drake throughflow-Tethys Seaway throughflow correlation we have found earlier. The stepwise evolutions of the throughflows will not be described here in detail, but their complex behavior reminds us to be careful with interpretations of bathymetric modifications in the Southern Ocean gateways. The Tasmanian Gateway consists of one single ocean grid cell, as well as the northern opening of Drake Passage. The precursor of the Antarctic peninsula, which has such a major influence on global circulation, consists of just three land cells. The most rapid circulation change in the widening experiments is found when the southernmost land cell of this island is converted to an ocean cell (green asterisk in Figure 45). While this change can be explained because this conversion allows a direct Drake throughflow in this region, it is far from robust: Global circulation is extremely sensitive on the path chosen around this little island (compare Section 2.5.2). This is not shown here, but described in the following.

Two correct paths were defined around the island, and were compared in two separate simu-

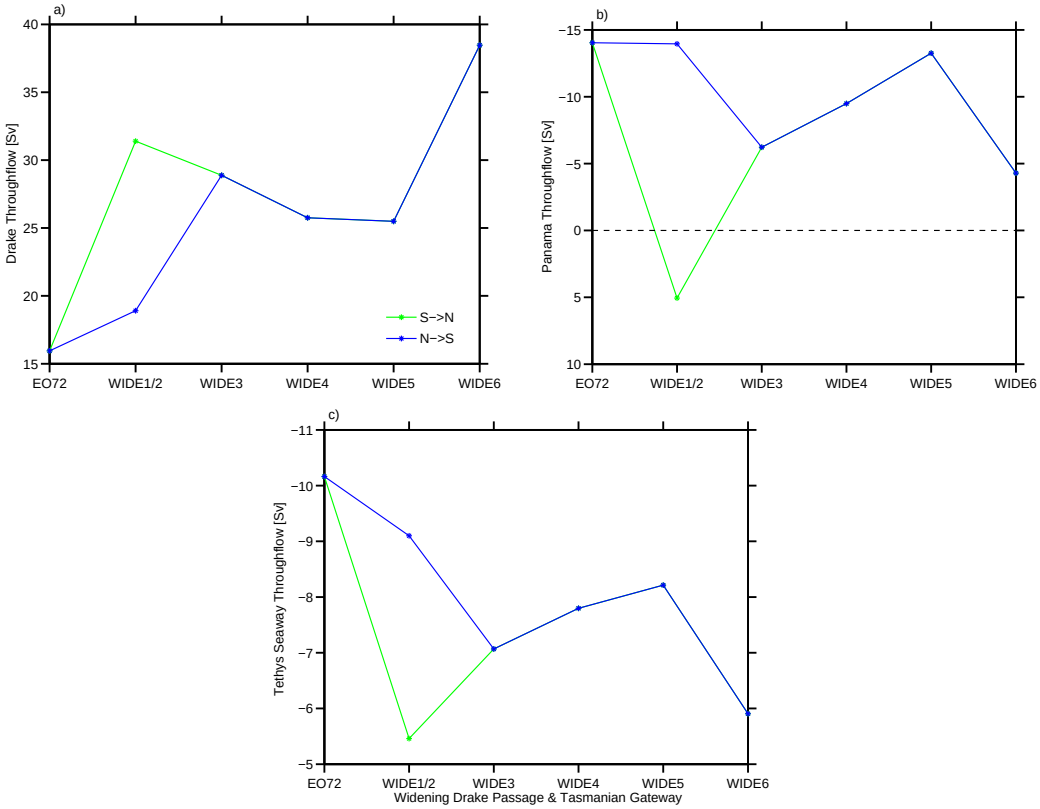

Figure 45: Evolutions of Drake throughflow (a), Panama throughflow (b), and STF (c) in response to a Drake Passage and Tasmanian Gateway widening from EO72, compare Table 2. The green line shows a Drake Passage opening starting from the South, and the blue line from the North. They coincide as the precursor of the Antarctic peninsula vanishes. Positive values indicate flow from west to east, negative values correspond to flow from east to west. Labels on the x-axis correspond to

lations, with all other paths unmodified. One of them, which led to the more credible result, is WIDE1 shown in Figure 41d and represented by the green asterisk in Figure 45. WIDE1 has a path directly along the coast of the island. In the other simulation, the path was chosen to be identical to the EO72 path, i.e., it encircles a southern ocean grid cell in addition to the two land cells in WIDE1. With this path a circulation was simulated that is much different from WIDE1 and the other Eocene bathymetries, with a much stronger east-to-west Panama throughflow of 47 Sv and an extremely fast circulation around the island (around 30 Sv in a small region, leading). While such an extreme effect of a path modification has not been recorded before, Marsh et al. (2011) found that moving the path around Antarctica latitudinally modifies the Drake Passage throughflow by up to 25 Sv, depending on model resolution. They used the C-GOLDSTEIN model, which has the same physical core as the Bern3D. Stefan Ritz also found similar paths effects during the development of the variable-grid version of the Bern3D model with different resolutions (pers. comm.). In other cases, a path modification may also have little to no effect, as was found in a follow-up experiment: Five vastly different paths around South America were tested in EO72, all producing a very similar ocean circulation.

We conclude that the EO72 bathymetry is not ideal to simulate the response of Nd isotopes to a Drake Passage opening in an Eocene setting, at least not with one of the two opening

methods tested here. The throughflow response on the opening is too complex, and the ocean system is too sensitive to changes in single grid boxes. Islands as small as the precursor of the Antarctic peninsula should not be included in a Bern3D bathymetry, a possible solution would be to reconnect the island to Antarctica as a standard. Furthermore, the Panama throughflow direction is not in agreement with the MPI-OM Eocene simulations (compare Section 3.4). If the EO72 bathymetry is to be used in future experiments, the climate setting should be tuned so it better represents Eocene conditions, and a more robust Drake Passage opening method should be used. A uniform opening as described in Section 3.2.2 is suggested, even if this leads to a larger deviation from the realistic Eocene Drake Passage bathymetry.

4. Summary and Outlook

After showing and discussing the results of our experiments, we can now summarize by answering the research questions that were raised in the introduction. We also give an outlook to how the experiments could be expanded and improved.

We have shown that a simple parametrization of Agulhas leakage can be realized in the Bern3D model and leads to the expected result of a strengthening of the AMOC. The parametrization has been realized as a freshwater dipole, with a freshwater flux out of a surface grid cell at cape Agulhas and into a surface cell in the Indian Ocean, simulating a salt flux in the opposite direction. The AMOC strengthening by the leakage parametrization is capable of compensating a weakening of the southern Atlantic-to-Pacific freshwater flux. However, the AMOC still shuts down if this flux is turned off. The Agulhas leakage parametrization has only a slight influence on the AMOC seasonality: the AMOC strenghtening by the leakage is strongest in the spring minimum. This is found for all tested shapes of the leakage freshwater forcing, which include triangular and rectangular steady forcings as well as 1 to 4 periodic freshwater pulses per year. We infer that the seasonality of the leakage is not transferred to the AMOC. Finally, strong freshwater pulses in the Agulhas region can also shut down the AMOC and produce different kinds of hysteresis behavior, depending on the freshwater compensation method used.

Very recently, a variable-grid version of the Bern3D model has been developed by Stefan Ritz (pers. comm.). It allows for a better resolution at high latitudes at the cost of a longer computation time. The resolution can be selected both in latitude and longitude, instead of the previous fixed constant longitude and sine latitude resolution. This way, the resolution may be varied regionally in longitudinal and latitudinal bands, such that, e.g., the resolution in the Atlantic can be better than in the Pacific. A suitable grid for the modern world bathymetry has been introduced in this model version, which features among other advantages a stronger ACC and a stronger AMOC, even without prescribing an Atlantic-to-Pacific freshwater flux. Therefore, an Agulhas leakage parametrization is not needed in this version to achieve a more realistic AMOC. But it would still be interesting to test the impact of Agulhas leakage in this model version. If further experiments are conducted, it is recommended to extend the freshwater dipole to a larger number of grid boxes; for example, the freshwater outflux of the ocean could be distributed over numerous cells along the leakage pathway, and the influx could be distributed over a larger region of the Indian Ocean. Drastic local changes in the SSS, as resulting from the one-gridbox dipole, could so be avoided. To make the parametrization more realistic, heat fluxes could be prescribed in addition to the freshwater fluxes, as done in similar experiments by Weijer et al. (2002).

In the experiments on modern-world tectonic rearrangements, the Bern3D model reached an equilibrium state in all modified bathymetries that were tested. Opening Panama Strait results in an east-to-west Panama throughflow, which is strengthened if Drake Passage is closed

additionally, and shuts down the AMOC. Closing the Drake Passage separately also weakens the AMOC and separates it from the Southern overturning cell, and increases the strength of southern hemispheric gyres. The modification of these two gateways caused various local changes in seafloor ϵ_{Nd} and $[Nd]_d$, as described in Section 3.2.1. Most notably, the opening of Panama Strait resulted in a widespread ϵ_{Nd} increase across the Atlantic, including the Atlantic sector of the Southern Ocean; whereas the closing of Drake Passage produced no clear signal in the latter region. The Strait of Suez openings that were tested had only a very slight influence on the global ocean circulation.

The opening of Drake Passage was simulated with both an open and a closed Panama Strait, and two different bathymetric evolutions of Drake Passage, a uniform opening and an opening proportional to the modern bathymetry. These two evolutions produced distinctly different results, in throughflows but even more pronounced in the seafloor ϵ_{Nd} measured around ODP sites 689 and 1090. This shows that the Nd response is highly sensitive to the choice of the bathymetric shape of Drake Passage during the opening process. Because we make fewer assumptions on this shape in the uniform opening case, the results of this opening are probably more robust. Therefore, they are compared to the Nd data from marine sediment cores described in Scher and Martin (2006) in Section 3.2.3.

An increase in seafloor ϵ_{Nd} around ODP sites 689 and 1090 is indeed found in the model simulations with a uniform opening. Around site 689, the increase is quantitatively similar to the sediment core data, around site 1090 the increase in the data is more pronounced. We conclue that the ϵ_{Nd} increase that Scher and Martin (2006) found at around 41 Ma could indeed correspond to the opening of Drake Passage. However, due to the sensitivity of the Nd response to bathymetric shape, further experiments need to be conducted to better assess the ϵ_{Nd} response to an opening of Drake Passage. These experiments should be carried out with better resolution in the low latitudes, i.e. with the new variable-grid version of the Bern3D model described above. The boundary source for Nd or its scaling factor, could be modified to assess its influence on the ϵ_{Nd} evolution. If it is possible to adapt the boundary source to the Eocene bathymetry, the Drake Passage opening (and influence of the Tasmanian Gateway) should also be simulated in this setting. The boundary source could be tuned such that steady state ϵ_{Nd} values around the ODP sites match the Eocene data shown in Figure 1 in Scher and Martin (2006) (before Drake Passage opening). It is suggested that the main focus of the continuation of this thesis should lie on the experiments proposed in this paragraph.

In the preparation of an Eocene bathymetry with better resolution for possible use in future experiments, the effects of a doubling of the horizontal model resolution were investigated. The doubling caused various changes in ocean circulation, as described in Section 2.7. Some circulation features were strengthened due to the reduced boundary drag, namely the ACC and some gyres, most notably small gyres like the Arctic polar gyre. The overall circulation patterns were not changed by the resolution increase in the modern world, but in the Eocene bathymetries the sensitive Panama throughflow (see below) was reversed.

The Eocene ocean circulation in the bathymetry with doubled resolution was then compared to the Eocene circulation in the comprehensive MPI ocean model. Qualitative agreement was found in the barotropic circulation, apart from the narrow tropical gyres which are missing in the Bern3D model, and a reversed Panama throughflow. However, modified Eocene bathymetries showed a Panama throughflow in the same direction as the MPI-OM, indicating that this throughflow is very sensitive to bathymetry changes in this Eocene setting. The meridional circulation is vastly different in the two models. In the Bern3D model, the SOMOC is strong and the AMOC shut down independently of atmospheric CO_2 concentration. In the MPI-OM, both a vigorous SOMOC and AMOC are found with $pCO_2 = 280\,ppm$, but the SOMOC is shut down and the AMOC weakened when pCO_2 is increased to 560 ppm (Heinemann, 2009). It has to be noted that apart from the land albedo, no climate forcings were changed in the Bern3D simulations with the Eocene bathymetry. For future Eocene experiments, the pCO_2 should be increased; this was done here only in some test simulations, and only in the radiative forcing of the EBM. If the BGC module is included for Nd experiments, the atmospheric CO_2 concentration should also be increased in the carbon cycle. The orbital forcing and other tunable parameters (e.g., atmospheric heat diffusion, longwave emissivity, feedback parameter) could be modified as well to obtain an Eocene steady state that compares well with more comprehensive models.

Finally, the influence of tectonic rearrangements on throughflows was tested in the Eocene bathymetry. Drake Passage was closed and widened from the standard Eocene bathymetry by modifying the northern and southern connections of the precursor of the Antarctic peninsula, which hinders the Drake throughflow in the Eocene bathymetry. The results from the stepwise closing are adoptable to a stepwise opening, because a separate spinup was performed for each step. They show rather complex throughflow changes and indicate that a more robust opening method should be used, if Nd experiments were to be conducted in this bathymetry. In addition to the Drake Passage, the Tasmanian Gateway was also modified. While a shallower Tasmanian Gateway had little effect on the throughflows, a closed or deeper gateway caused significant changes. We infer that these cases should also be considered in future Nd experiments in an Eocene setting.

Appendix A. The seven input maps

***.k1** This most important map contains two types of information: bathymetry and runoff map. All grid cells with numbers between 1 and 32 denote ocean grid cells, and the numbers specify their seafloor elevation level k. The relation between k and the cell depth z_k^w in metres is given by equation 1. Land cells contain numbers between 91 and 94, which determine the runoff direction: 91 =eastward from this cell; 92 =southward; 93 =westward and 94 =northward.

***.bmask** This mask is relevant only for ocean cells. It splits the ocean into regions (e.g. North Atlantic, Central Atlantic, South Atlantic, etc.), which can be used for plotting and for freshwater experiments. It can be customized to include smaller regions down to one single grid cell.

***.lmask** Similar to `*.bmask`, but for land cells.

***.dyemask** This mask is only needed if dye tracers are used. The inlet locations for any number of different dye tracers are specified in this mask.

***.alti** This mask contains an altitude value for each land cell, and is only used for the diagnostic computation of land temperature assuming a constant lapse rate.

***.psiles** While all masks described so far contain values for the centers of the grid cells, the `.psiles` mask contains a value for the edges. Compare Ritz (2012) for details on the center and edge grids. Apart from assigning each edge to land or ocean, the `*.psiles` mask also numbers the edges according to the island they belong to. This is used in the calculation of the ocean circulation.

***.paths** This is not an actual world mask, but a list of paths. There is a path for each island except the mainland (Eurasia in MOD36), which is used to calculate the path integral around the island. Above the list of paths, a list of numbers is given which indicates the lengths of the paths in steps.

Appendix B. Description of the regridding process

The first regridding step was performed using using the "Ferret" program, which has a built-in regridding function. Two of the several available interpolation methods were tested: averaging and linear. The linear interpolation was chosen because the resulting coarse bathymetry was visually more similar to the original bathymetry. The missing values corresponding to the land cells in the original bathymetry were replaced by zeros before the bathymetry was interpolated to the Bern3D grid. If the interpolation had been applied to the original bathymetry with missing values, the resulting land masses on the Bern3D grid would have been much too large, because the value of a new cell which overlaps any old missing value cell is automatically missing. The regridded bathymetry ferret output is a two-dimensional map of ocean depths in meters, not elevation levels. The land/sea mask was also regridded in Ferret, without prior modifications.

The combination of the bathymetry and the land/sea mask was then done in MATLAB, as well as the conversion of depths to depth levels. In a first step, all cells for which the land fraction in the land/sea mask was larger than 0.6 were converted to land boxes in the bathymetry mask (by filling them with missing values). It may appear more intuitive to convert all cells with a land fraction larger than 0.5, but this number was tuned to 0.6 in favor of more ocean boxes. Apart from creating a map that was visually more similar to the original bathymetry, this was done mainly for practical reasons, as explained in the next paragraph. Each cell was then assigned a seafloor elevation level based on its depth, as described in the following. A cell was assigned the seafloor elevation k if its depth in the original map lay between z^c_{k-1} and z^c_k. Here, z^c_k, $k \in \{1, 2, ..., kmax\}$ are the centers of the Bern3D depth layers, as calculated in equation 2. This assignment also means that all cells with a depth smaller than $z^c_{kmax} = 19\,\mathrm{m}$ have to be converted to land cells, if they have not been converted before.

From the regridding process, map inconsistencies arose, such as unrealistic land fragments or enclosed ocean boxes. To remove these, some corrections were finally made by hand. Most notably, some isolated ocean boxes in the northernmost cell row were closed, as well as a number of shallow ocean boxes in the southernmost row. The latter was done to remove the irregular pattern of land and ocean boxes in the Pacific part of the southernmost row. An alternative would have been to open the land boxes in this region. It was not chosen because this would also have resulted in a broader Drake Passage, which was too open already without this modification, because the island obstructing the throughflow (compare Figure 5) was not resolved. This last step also explains why critical cells should rather be regridded to ocean cells than to land cells, as described in the previous paragraph: if a correction has to be made by hand, it is much easier to convert an ocean cell into a land cell than vice versa, because no assumptions have to be made on the depth of the cell.

References

Beal, L. M., De Ruijter, W. P. M., Biastoch, A., Zahn, R., and 136, SCOR WCRP IAPSO Working Grp (2011). "On the role of the Agulhas system in ocean circulation and climate". *Nature*, *472*, 429–436. DOI: 10.1038/nature09983.

Biastoch, A., Boening, C. W., Schwarzkopf, F. U., and Lutjeharms, J. R. E. (2009). "Increase in Agulhas leakage due to poleward shift of Southern Hemisphere westerlies". *Nature*, *462*, 495–U188. DOI: 10.1038/nature08519.

Cohen, K.M., Finney, S., and Gibbard, P. L. (2012). *International Chronostratigraphic Chart*. URL: www.stratigraphy.org/ICSchart/ChronostratChart2012.pdf.

Collins, M., Tett, S. F. B., and Cooper, C. (2001). "The internal climate variability of HadCM3, a version of the Hadley Centre coupled model without flux adjustments". *Clim. Dyn.*, *17*, 61–81. DOI: 10.1007/s003820000094.

Ganachaud, A. and Wunsch, C. (2000). "Improved estimates of global ocean circulation, heat transport and mixing from hydrographic data". *Nature*, *408*, 453–457. DOI: 10.1038/35044048.

Gerber, M. and Joos, F. (2013). "An Ensemble Kalman Filter multi-tracer assimilation: Determining uncertain ocean model parameters for improved climate-carbon cycle projections". *Ocean Modelling*, *64*, 29 –45. DOI: 10.1016/j.ocemod.2012.12.012.

Godfrey, J. S. (1989). "A Sverdrup Model of the Depth-Integrated Flow for the World Ocean allowing for Island Circulation". *Geophys. Astro. Fluid Dyn.*, *45*, 89–112. DOI: 10.1080/03091928908208894.

Gregory, J. M., Dixon, K. W., Stouffer, R. J., Weaver, A. J., Driesschaert, E., Eby, M., Fichefet, T., Hasumi, H., Hu, A., Jungclaus, J. H., Kamenkovich, I. V., Levermann, A., Montoya, M., Murakami, S., Nawrath, S., Oka, A., Sokolov, A. P., and Thorpe, R. B. (2005). "A model intercomparison of changes in the Atlantic thermohaline circulation in response to increasing atmospheric CO_2 concentration". *Geophys. Res. Lett.*, *32*. DOI: 10.1029/2005GL023209.

Heinemann, M. (2009). "Warm and sensitive Paleocene-Eocene Climate". PhD thesis. Department Geowissenschaften der Universitaet Hamburg.

Hu, A., Meehl, G. A., Han, W., Timmermann, A., Otto-Bliesner, B., Liu, Z., Washington, W. M., Large, W., Abe-Ouchi, A., Kimoto, M., Lambeck, K., and Wu, B. (2012). "Role of the Bering Strait on the hysteresis of the ocean conveyor belt circulation and glacial climate stability". *Proc. Natl. Acad. Sci. U. S. A.*, *109*, 6417–6422. DOI: 10.1073/pnas.1116014109.

Johns, T. C., Carnell, R. E., Crossley, J. F., Gregory, J. M., Mitchell, J. F. B., Senior, C. A., Tett, S. F. B., and Wood, R. A. (1997). "The second Hadley Centre coupled ocean-atmosphere GCM: Model description, spinup and validation". *Clim. Dyn.*, *13*, 103–134. DOI: 10.1007/s003820050155.

Kanzow, T., Cunningham, S. A., Johns, W. E., Hirschi, J. J. M., Marotzke, J., Baringer, M. O., Meinen, C. S., Chidichimo, M. P., Atkinson, C., Beal, L. M., Bryden, H. L., and Collins, J. (2010). "Seasonal Variability of the Atlantic Meridional Overturning Circulation at 26.5 degrees N". *J. Clim.*, *23*, 5678–5698. DOI: 10.1175/2010JCLI3389.1.

Kosch, M. (2011). "The Snowball Earth Hypothesis: Experiments with the Bern3D Model". MA thesis. University of Bern.

Lawver, L. M. and Gahagan, L. M. (1998). "Tectonic Boundary Conditions for Climate Reconstructions". Ed. by T. J. Crowley and K. G. Burke. Vol. 39. Oxford Univ. Press, New York. Chap. Opening of Drake Passage and Its Impact on Cenozonic Ocean Circulation, pp. 212–226.

Lehmann, E. (2011). "Centennial-scale Oscillations of the Atlantic Meridional Overturning Circulation in Freshwater Experiments with the Bern3D Model". MA thesis. University of Bern.

Levitus, S. and Boyer, T. (1994). *Temperature*. World Ocean Atlas 4.

Levitus, S, Burgett, R., and Boyer, T. (1994). *Salinity*. World Ocean Atlas 3.

Lunt, D. J., Valdes, P. J., Dunkley Jones, T., Ridgwell, A., Haywood, A. M., Schmidt, D. N., Marsh, R., and Maslin, M. (2010). "CO_2-driven ocean circulation changes as an amplifier of Paleocene-Eocene thermal maximum hydrate destabilization". *Geology*, *38*, 875–878. DOI: 10.1130/G31184.1.

Lunt, D. J., Dunkley Jones, T., Heinemann, M., Huber, M., LeGrande, A., Winguth, A., Loptson, C., Marotzke, J., Roberts, C. D., Tindall, J., Valdes, P. J., and Winguth, C. (2012). "A model-data comparison for a multi-model ensemble of early Eocene atmosphere-ocean simulations: EoMIP". *Climate of the Past*, *8*, 1717–1736. DOI: 10.5194/cp-8-1717-2012.

Marsh, R., Mueller, S. A., Yool, A., and Edwards, N. R. (2011). "Incorporation of the C-GOLDSTEIN efficient climate model into the GENIE framework: "eb_go_gs" configurations of GENIE". *Geosci. Model Dev.*, *4*, 957–992. DOI: 10.5194/gmd-4-957-2011.

Meinshausen, M., Smith, S. J., Calvin, K., Daniel, J. S., Kainuma, M. L. T., Lamarque, J-F., Matsumoto, K., Montzka, S. A., Raper, S. C. B., Riahi, K., Thomson, A., Velders, G. J. M., and Vuuren, D. P. P. (2011). "The RCP greenhouse gas concentrations and their extensions from 1765 to 2300". *Clim. Chang.*, *109*, 213–241. DOI: 10.1007/s10584-011-0156-z.

Menviel, L., Joos, F., and Ritz, S. P. (2012). "Simulating atmospheric CO_2, C-13 and the marine carbon cycle during the Last Glacial-Interglacial cycle: possible role for a deepening of the mean remineralization depth and an increase in the oceanic nutrient inventory". *Quat. Sci. Rev.*, *56*, 46–68. DOI: 10.1016/j.quascirev.2012.09.012.

Mueller, S. A., Joos, F., Edwards, N. R., and Stocker, T. F. (2006). "Water mass distribution and ventilation time scales in a cost-efficient, three-dimensional ocean model". *J. Clim.*, *19*, 5479–5499. DOI: 10.1175/JCLI3911.1.

Parekh, P., Joos, F., and Mueller, S. A. (2008). "A modeling assessment of the interplay between aeolian iron fluxes and iron-binding ligands in controlling carbon dioxide fluctuations during Antarctic warm events". *Paleoceanography*, *23*. DOI: 10.1029/2007PA001531.

Pearson, P. N. and Palmer, M. R. (2000). "Atmospheric carbon dioxide concentrations over the past 60 million years". *Nature*, *406*, 695–699. DOI: 10.1038/35021000.

Peeters, F. J. C., Acheson, R., Brummer, G. J. A., Ruijter, W. P. M. de, Schneider, R. R., Ganssen, G. M., Ufkes, E., and Kroon, D. (2004). "Vigorous exchange between the Indian and Atlantic oceans at the end of the past five glacial periods". *Nature*, *430*, 661–665. DOI: 10.1038/nature02785.

Rahmstorf, S., Crucifix, M., Ganopolski, A., Goosse, H., Kamenkovich, I., Knutti, R., Lohmann, G., Marsh, R., Mysak, L. A., Wang, Z. M., and Weaver, A. J. (2005). "Thermohaline circulation hysteresis: A model intercomparison". *Geophys. Res. Lett.*, *32*. DOI: 10.1029/2005GL023655.

Rempfer, J., Stocker, T. F., Joos, F., Dutay, J., and Siddall, M. (2011). "Modelling Nd-isotopes with a coarse resolution ocean circulation model: Sensitivities to model parameters and source/sink distributions". *Geochim. Cosmochim. Acta*, *75*, 5927–5950. DOI: 10.1016/j.gca.2011.07.044.

Rempfer, J., Stocker, T. F., Joos, F., and Dutay, J. (2012). "On the relationship between Nd isotopic composition and ocean overturning circulation in idealized freshwater discharge events". *Paleoceanography*, *27*. DOI: 10.1029/2012PA002312.

Ritz, S. P. (2007). "Global Distribution of Radiocarbon during Changes of the Atlantic Meridional Overturning Circulation". MA thesis. University of Bern.

Ritz, S. P. (2012). *Documentation of the Physical Core of the Bern3D Ocean Component*.

Ritz, S. P., Stocker, T. F., and Joos, F. (2011). "A Coupled Dynamical Ocean-Energy Balance Atmosphere Model for Paleoclimate Studies". *J. Clim.*, *24*, 349–375. DOI: 10.1175/2010JCLI3351.1.

Roth, R. and Joos, F. (2013). "A reconstruction of radiocarbon production and total solar irradiance from the Holocene ^{14}C and CO_2 records: implications of data and model uncertainties". *Climate of the Past Discussions*, *9*, 1165–1235. DOI: 10.5194/cpd-9-1165-2013.

Scher, H. D. and Martin, E. E. (2004). "Circulation in the Southern Ocean during the Paleogene inferred from neodymium isotopes". *Earth Planet. Sci. Lett.*, *228*, 391–405. DOI: 10.1016/j.epsl.2004.10.016.

Scher, H. D. and Martin, E. E. (2006). "Timing and climatic consequences of the opening of Drake Passage". *Science*, *312*, 428–430. DOI: 10.1126/science.1120044.

Schettino, Antonio and Turco, Eugenio (2009). "Breakup of Pangaea and plate kinematics of the central Atlantic and Atlas regions". *Geophys. J. International*, *178*, 1078–1097. DOI: 10.1111/j.1365-246X.2009.04186.x.

Sebille, E. van and Leeuwen, P. J. van (2007). "Fast northward energy transfer in the Atlantic due to Agulhas rings". *J. Phys. Oceanogr.*, *37*, 2305–2315. DOI: 10.1175/JPO3108.1.

Sebille, E. van, Johns, W. E., and Beal, L. M. (2012). "Does the vorticity flux from Agulhas rings control the zonal pathway of NADW across the South Atlantic?" *J. Geophys. Res.-Oceans*, *117*. DOI: 10.1029/2011JC007684.

Sluijs, A., Bijl, P. K., Schouten, S., Roehl, U., Reichart, G. J., and Brinkhuis, H. (2011). "Southern ocean warming, sea level and hydrological change during the Paleocene-Eocene thermal maximum". *Clim. Past*, *7*, 47–61. DOI: 10.5194/cp-7-47-2011.

Smith, R. S., Dubois, C., and Marotzke, J. (2006). "Global climate and ocean circulation on an aquaplanet ocean-atmosphere general circulation model". *J. Clim.*, *19*, 4719–4737. DOI: 10.1175/JCLI3874.1.

Stocker, T. F. (2002). "North-south connections". *Science*, *297*, 1814–1815. DOI: 10.1126/science.1075870.

Stocker, T. F. and Marchal, O. (2000). "Abrupt climate change in the computer: Is it real?" *Proc. Natl. Acad. Sci. U. S. A.*, *97*, 1362–1365. DOI: 10.1073/pnas.97.4.1362.

Stocker, T.F. (2011). *Introduction to Climate Modelling (Advances in Geophysical and Environmental Mechanics and Mathematics)*. Springer-Verlag Berlin Heidelberg.

Tindall, J., Flecker, R., Valdes, P. J., Schmidt, D. N., Markwick, P. J., and Harris, J. (2010). "Modelling the oxygen isotope distribution of ancient seawater using a coupled ocean-atmosphere GCM: Implications for reconstructing early Eocene climate". *Earth Planet. Sci. Lett.*, *292*, 265 –273. DOI: 10.1016/j.epsl.2009.12.049.

Toggweiler, J. R. and Samuels, B. (1995). "Effect of Drake Passage on the global thermohaline circulation". *Deep-Sea Res. Pt.I*, *42*, 477–500. DOI: 10.1016/0967-0637(95)00012-U.

Tschumi, T., Joos, F., and Parekh, P. (2008). "How important are Southern Hemisphere wind changes for low glacial carbon dioxide? A model study". *Paleoceanography*, *23*. DOI: 10.1029/2008PA001592.

UCAR (2013a). *CESM 1.1 Experiments, Data and Diagnostics*. URL: http://www.cesm.ucar.edu/experiments/cesm1.1.

UCAR (2013b). *CESM 1.1 Experiments, Data and Diagnostics: Barotropic Stream Function*. URL: http://www.cesm.ucar.edu/experiments/cesm1.1/diagnostics/b.e11.B1850C5CN.f09_g16.001/ocn_1-50-obs/BSF.gif.

Veevers, J. J., Clare, A., and Wopfner, H. (1994). "Neocratonic magmatic-sedimentary basins of post-Variscan Europe and post-Kanimblan eastern Australia generated by right-lateral transtension of Permo-Carboniferous Pangaea". *Basin Research*, *6*, 141–157. DOI: 10.1111/j.1365-2117.1994.tb00081.x.

Wei, X., Hahmann, A. N., Dickinson, R. E., Yang, Z. L., Zeng, X. B., Schaudt, K. J., Schaaf, C. B., and Strugnell, N. (2001). "Comparison of albedos computed by land surface models and evaluation against remotely sensed data". *J. Geophys. Res.-Atmos.*, *106*, 20687–20702. DOI: 10.1029/2001JD900218.

Weijer, W., De Ruijter, W. P. M., Sterl, A., and Drujfhout, S. S. (2002). "Response of the Atlantic overturning circulation to South Atlantic sources of buoyancy". *Global Planet. Change*, *34*. Symposium on From Process Studies to Reconstruction of the Palaeoenvironment, NICE, FRANCE, APR 25-29, 2000, 293–311. DOI: 10.1016/S0921-8181(02)00121-2.

Zachos, J., Pagani, M., Sloan, L., Thomas, E., and Billups, K. (2001). "Trends, rhythms, and aberrations in global climate 65 Ma to present". *Science*, *292*, 686–693. DOI: 10.1126/science.1059412.

Zaucker, F., Stocker, T.F., and Broecker, W.S. (1994). "Atmospheric Fresh-water Fluxes and their Effect on the Global Thermohaline Circulation". *J. Geophys. Res.-Oceans*, *99*, 12443–12457. DOI: 10.1029/94JC00526.

Acknowledgements

I would like to thank ...

... Thomas Stocker for giving me the opportunity to write this thesis, and for taking the time to provide me with most helpful input and feedback in a time of much greater responsibilities.

... Stefan Ritz for introducing me to the Bern3D model and his matlab tools, and for providing assistance whenever it was needed.

... Raphael Roth for being the "Bern3D Doc", for proof-reading and for showing me some nerdy tricks.

... Everybody at KUP with whom I have had the pleasure to hold scientific and non-scientific discussions.

... my family for their invaluable support.